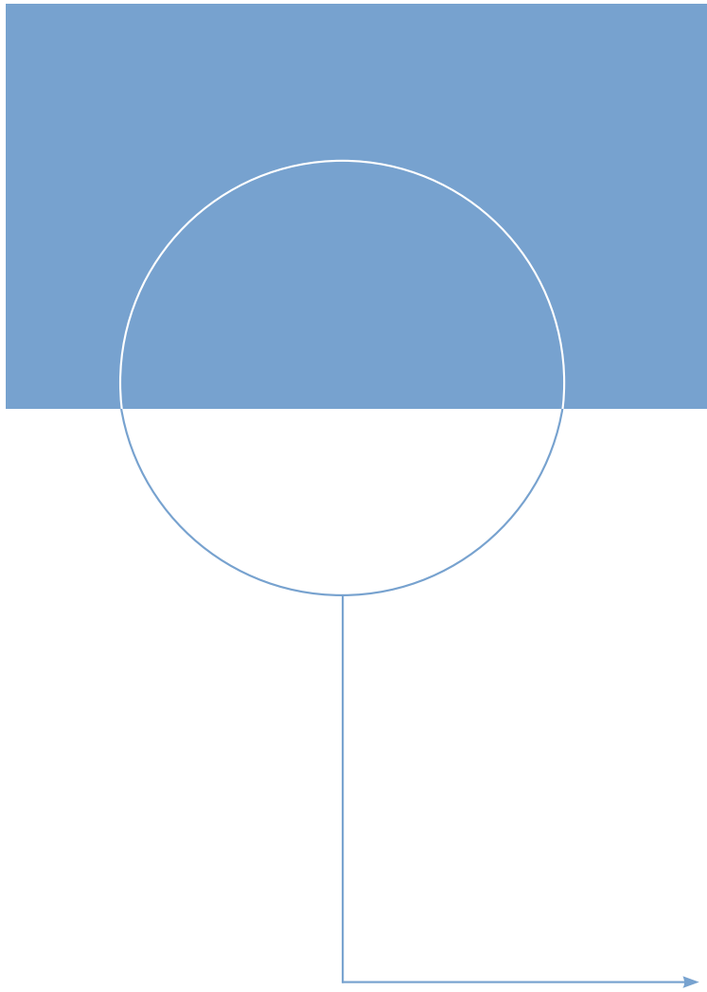

Master's thesis

2020

Frida Mattson

NTNU
Norwegian University of
Science and Technology
Faculty of Engineering
Department of Marine Technology

Frida Mattson

Numerical Study of Nonlinear Effects for the Wave-Induced Drift Loads on an FPSO

July 2020

NTNU
Norwegian University of
Science and Technology

NTNU
Norwegian University of
Science and Technology

NTNU
Norwegian University of
Science and Technology

Numerical Study of Nonlinear Effects for the Wave-Induced Drift Loads on an FPSO

Frida Mattson

Master's Thesis in Marine Technology
Submission date: July 2020
Supervisor: Marilena Greco
Co-supervisor: Arne Nestegård

Norwegian University of Science and Technology
Department of Marine Technology

NTNU Trondheim
Norwegian University of Science and Technology
Faculty of Engineering Science and Technology
Department of MarineTechnology

MASTER THESIS IN MARINE TECHNOLOGY

Spring 2020

FOR

Frida Mattson

Numerical Study of Nonlinear Effects for the Wave-Induced Drift Loads on an FPSO

(Numerisk studie av ikke-lineære effekter for bølgeinduserte driftkrefter på en FPSO)

A turret moored FPSO weathervanes around the mooring system, enabling the FPSO to position the vessel favorably against the wind with its bow against the waves. In extreme sea states, bow impact and green sea contribute significantly to the loads and motion response of the vessel. Large steep waves will enhance the pitch motions and the low-frequency surge drift force. These highly non-linear effects should be accounted for in the design of the mooring system.
In the Project thesis, the candidate performed a literature study on the state-of-the-art and carried out a preliminary investigation using the linear potential-flow frequency-domain DNV GL software SESAM: Hydro-D (Wadam). She performed a numerical-convergence analysis and then examined the influence of the FPSO bow geometry (using a basic geometry and two bow modifications) on the linear body motions and on the mean-drift force in surge induced by regular head-sea waves. The student also selected the CFD solver ComFLOW as a research tool for the Master-thesis studies.

Objective
The present Master thesis aims to investigate the importance of nonlinear wave-body interaction effects (e.g. large motions, wave-bow impacts events, etc.) on the FPSO drift loads in waves.

The work should be carried out in steps as follows:

1. Summarize major findings/outcomes from the Project thesis, reporting on the background and motivation, literature study, and analysis so far carried out. Possibly complement a) the literature survey in order to characterize the state-of-the-art of the problem and b) the Wadam analysis, e.g. attempt improving the numerical modelling of the wall sided geometry for an enhanced Wadam solution and estimate the mean-drift loads for the diffraction problem.
2. Describe the selected CFD method, ComFLOW, and its basic assumptions considered in the present study. Perform a numerical convergence study, both in terms of discretization size and fluid-domain extension, for the basic FPSO fixed in regular head-sea waves.
3. Select at least three incident-wave frequencies (from the Project work) and steepnesses (so to go from linear to steep incident-wave conditions) and examine the basic FPSO as fixed in head-sea regular waves. Compare the integrated loads against the diffraction-problem results from Wadam and discuss them.
4. Select at least three incident-wave frequencies (from the Project work) with at least three steepnesses (so to go from linear to steep incident-wave conditions) and examine the basic FPSO as freely floating in head-sea regular waves. For simplicity, neglect the mooring-line system and assume fixed all degrees of freedom but for heave and pitch motion of the

FPSO. Compare the results against wave-induced motions and mean-drift force in surge from Wadam and discuss them. If time allows, model the mooring-line system as linear springs so to reproduce realistic natural period in surge and study the effect on the mean-drift force in surge for one selected case.

5. Examine the three bow geometries, identified during the Project work, both as fixed and as freely floating (in heave and pitch) for at least one incident-wave frequency and one wave steepness. Compare the integrated loads against Wadam results and discuss them.
6. Draw the conclusions from the studies carried out and their results and discuss possible further research steps.

The work may show to be more extensive than anticipated. Some topics may therefore be left out after discussion with the supervisor without any negative influence on the grading.

The candidate should in her report give a personal contribution to the solution of the problem formulated in this text. All assumptions and conclusions must be supported by mathematical models and/or references to physical effects in a logical manner.

The candidate should apply all available sources to find relevant literature and information on the actual problem.

The thesis should be organised in a rational manner to give a clear presentation of the work in terms of exposition of results, assessments, and conclusions. It is important that the text is well written, and that tables and figures are used to support the verbal presentation. The thesis should be complete, but still as short as possible. In particular, the text should be brief and to the point, with a clear language. Telegraphic language should be avoided.

The thesis must contain the following elements: the text defining the scope (i.e. this text), preface (outlining project-work steps and acknowledgements), abstract (providing the summary), table of contents, main body of thesis, conclusions with recommendations for further work, list of symbols and acronyms, references and (optional) appendices. All figures, tables and equations shall be numerated.

The supervisor may require that the candidate, in an early stage of the work, present a written plan for the completion of the work. The plan should include budget for the use of computer and laboratory resources that will be charged to the department. Overruns shall be reported to the supervisor.

From the thesis it should be possible to identify the work carried out by the candidate and what has been found in the available literature. It is important to give references to the original source for theories and experimental results.

Supervisor : Marilena Greco
Co-supervisor : Arne Nestegård

Submitted : January 15th 2020
Deadline : July 1th 2020

Marilena Greco
Supervisor

Preface

This thesis is written by Frida Mattson as a part of the Master of Science degree in Marine Technology within Marine Hydrodynamics at the Norwegian University of Science and Technology in Trondheim. The work was carried out during the spring semester of 2020, and have an equivalence of 30 ECTS. The master thesis is a continuation of the preliminary work, project thesis, performed during the fall semester of 2019. The work was accomplished in cooperation with DNV GL, which suggested the topic, provided the software, extra computational power, and contributed with a co-supervisor.

The master thesis discloses a numerical study of drift loads on an FPSO, using the potential theory code Wadam, and the CFD code ComFLOW. A considerable amount of time was used to set up and getting familiar with the software. Especially defining the grid in ComFLOW turned out very challenging.

The dissertation was written during the outbreak of Covid-19. The consequence for this thesis was counseling sessions online, and the plan of writing from DNV GL's offices at Høvik was cancelled. The increase of students and employees at NTNU working from home, caused the queue to escalate on the cluster Idun and the supercomputer Saga. The latter was partly reserved for scientific research on the virus for the Norwegian Health Department, which further increased the waiting time.

It was a great challenge using the extra computational power. Limitations related to the allocated memory on the user at Idun only made it possible to use it for primarily testing of ComFLOW. Saga and DNV GL's cluster Tyr were used for the analysis. As the different high performance computers had slightly different setups an appreciable extent of time was used to master the systems.

Over all, I have found the process of writing this thesis to be very educational and interesting. It has been a challenging and complex task, but all the more rewarding.

Frida Mattson
Oslo, July 1th 2020

Acknowledgements

I would first like to thank my supervisor, Marilena Greco, for her academic encouragement and insight. Marilena has during our weekly meetings guided and challenged me with her knowledge and questions and introduced me to new aspects of solving problems and presenting results. I have very much appreciated her positive spirit and support in a challenging and, in many ways, different semester.

I wish to express my gratitude to my co-supervisor Arne Nestegård, for suggesting an interesting and relevant topic and helping me shape the target of the master thesis. The feedback, comments, and remarks on my work have been invaluable. I would like to thank Arne for his engagement in my learning process, both through discussions and by providing relevant literature.

I would like to acknowledge Øystein Lande for giving me the introduction to ComFLOW, and answering my many questions along the way. I wish to express my very profound gratitude to DNV GL, and especially the unit of *Hydrodynamics, MetOcean and SRA*, for their support, and for providing extra computational resources.

In addition, I must recognize Bjørn Lindi for his technical support with Saga and Idun, for introducing me to the terminal, his endless patience and for always being available. I would also like to thank Kjell Larsen and Equinor for providing a model of an FPSO with corresponding results.

Finally, the support from my classmates and my family has been inestimable. I am tremendously grateful for the companionship from my fellow students in academia, but also for the friendships, making these five years memorable.

Abstract

The main objective of the thesis was to investigate the importance of nonlinear wave-body interaction effects on the FPSO drift loads in waves in three dimensions, focusing on the mean drift loads. This thesis presents a systematic study of the forces and motions of an FPSO performed with the CFD solver ComFLOW and compared with results from the linear potential solver Wadam.

A brief technical introduction of an FPSO is given before some basic theory behind the software is presented followed by a selection of relevant literature describing the state-of-the-art methods and common industry practice for drift loads.

A geometry with bulb, one without bulb, and one wall sided geometry were modeled in GeniE and analysed in Wadam. The RAO's revealed that the geometry with and without bulb had similar behaviors, while the wall sided geometry had larger surge motions but smaller heave and pitch response. The wall sided geometry did also have the largest mean drift force in surge. Comparing the floating and fixed FPSO, the high mean drift force for the wall sided geometry was mainly due to the diffracted waves.

The direct pressure integration method and the conservation of fluid momentum method were used to calculate the forces, and the results were compared. The direct pressure integration method proved to be more sensitive to uneven geometries, leading the conservation of fluid momentum to be the most robust theory.

To study the problem as fully nonlinear, a CFD analysis was completed. First, a convergence study of the domain size, the meshing of the geometry, and the refinement of the grid of the domain was done. The test was conducted for a wave period of 10 s and a wave amplitude of 1 m, which was assumed to satisfy the linear conditions and, hence, be comparable to Wadam. According to the convergence ratio and the order of accuracy, only some of the tests clearly demonstrated convergence. Based on the reduction in the deviation from Wadam and the CPU time, a domain size of 1472 m x 623 m x 220 m, a geometry mesh of 7.07 m, and a domain grid refinement of 0.94 m x 1.03 m x 0.67 m

were chosen.

The analysis were done for a fixed and a floating geometry with bulb for the wave periods of 4 s, 8 s and 11 s, which according to the Wadam results were in the range of periods experiencing significant drift forces. Three amplitudes corresponding to 10%, 50% and 70% of the maximum steepness were studied for a fixed FPSO, while a fourth steepness of 90% of the maximum steepness was added for the floating vessel. In addition, the three different bow geometries were examined for a wave period of 11 s with an amplitude corresponding to a steepness of 10% of the maximum steepness for both a fixed and a floating FPSO.

The results from ComFLOW were expected to be close to the results from Wadam for the waves with the steepness of 10% of the maximum steepness. As the steepness of the waves increases, more nonlinearities are introduced which cause higher drift forces. Based on this the results from ComFLOW were anticipated to predict higher drift forces than Wadam for the higher steepnesses. However, the fixed and floating cases analyzed for the geometry with bulb detected lower mean drift forces for all but one steepness. The analysis for the three bow geometries resulted in higher mean drift forces in surge for all the cases studied. ComFLOW turned out to be sensitive regarding the grid size of the domain, which could be a contribution to the unexpected results.

To further develop the model, the set up of parameters and grid should be improved. ComFLOW should be validated against other CFD programs to investigate if ComFLOW needs to be further developed to accurately calculate the mean drift forces. Additional features as irregular sea, mooring lines and current should be implemented to enable the study of more realistic cases.

Sammendrag

Hovedmålet med denne oppgaven var å undersøke viktigheten av ikke-lineære interaksjonseffekter mellom bølger og skip for driftskreftene på en FPSO i bølger i tre dimensjoner, med fokus på de midlere driftkreftene. Denne avhandlingen presenterer en systematisk studie av kreftene og bevegelsene til en FPSO utført med CFD-løseren ComFLOW og sammenlignet med resultatene fra den lineære potensielle løseren Wadam.

En kort teknisk introduksjon av en FPSO blir gitt før grunnleggende teori bak programvarene presenteres etterfulgt av et utvalg av relevant litteratur som beskriver moderene metoder og vanlig bransjepraksis for beregning av driftkrefter.

En geometri med bulb, en uten bulb, og en rettsidet geometri ble modellert i GeniE og analysert i Wadam. RAO'ene avslørte at geometriene med og uten bulb oppførte seg likt, mens den rettsidede geometrien hadde større jag-bevegelser, men mindre bevegelser i hiv og stamp. Den rettsidede geometrien hadde også den største midlere driftkraften i jag. Ved å sammenligne den flytende og den fasteholdte FPSOen ble det klart at den høye midlere driftkraften for den resttsidede geometrien i jag hovedsakelig kom fra de diffrakterte bølgene.

Metoden for direkte trykkintegrasjon og metoden for bevaring av beveglesesmengden til fluidet ble brukt til å beregne kreftene, og resultatene ble sammenlignet. Metoden for direkte trykkintegrering viste seg å være mer følsom for ujevneheter i geometrien, noe som førte til at metoden for bevaring av beveglesesmengden til fluidet var den mest robuste teorien.

For å studere problemet som fullstendig ulineært, ble en CFD-analyse utført. Først ble det gjort en konvergenstest av domenestørrelsen, meshing av geometri og størrelsen på rutenett i domenet. Testen ble utført med en bølgeperiode på 10 s og en bølgeamplitude på 1 m, noe som ble antatt å tilfredsstille de lineære forholdene og dermed være sammenlignbart med Wadam. I henhold til konvergensraten og orden av nøyaktighet, var det bare noen av testene som tydelig viste konvergens. Basert på reduksjonen i avvik fra

Wadam og CPU-tiden, ble en domenestørrelse på 1472 m x 623 m x 220 m, en geometri med mesh på 7.07 m og et rutenett for domenet med størrelsene 0.94 m x 1.03 m x 0.67 m, valgt.

Analysen ble gjort for en fastholdt og en flytende geometri med bulb for bølgeperiodene 4 s, 8 s og 11 s, som ifølge Wadam-resultatene var i området for periodene med betydelige driftkrefter. Tre amplituder tilsvarende 10%, 50% og 70% av maksimal bølgesteilhet ble studert for en fast FPSO, mens en fjerde steilhet på 90% av den maksimale bølgesteilhet ble lagt til for det flytende fartøyet. I tillegg ble de tre forskjellige bauggeometriene undersøkt for en bølgeperiode på 11 s med en amplitude som korresponderte til en steilhet på 10% av maksimal bølgesteilhet for både en fastholdt og en flytende FPSO.

Resultatene fra ComFLOW var forventet å være nær resultatene fra Wadam for bølger med steilhet på 10% av maksimal bølgesteilhet. Når bølgenes steilhet øker, innføres flere ikke-lineariteter som forårsaker høyere driftkrefter. Basert på dette ble resultatene fra ComFLOW forventet å predikere høyere driftkrefter enn Wadam for de høyere steilhetene. Imidlertid viste analysene for de fasteholdte og flytende tilfellene for geometrien med bulb at det var lavere gjennomsnittlige driftkrefter for alle bortsett fra én steilhet. Analyse for de tre bauggeometriene resulterte i høyere gjennomsnittlige driftkrefter for alle tilfellene som ble undersøkt. ComFLOW viste seg å være følsom når det gjelder nettstørrelsen til domenet, noe som kan ha vært et bidrag til de uventede resultatene.

For å videreutvikle modellen bør oppsettet av parametere og rutenettet forbedres. ComFLOW bør valideres mot andre CFD-programmer for å umdersøke om ComFLOW burde videreutvikles før det brukes til beregninger av midlere dirftkrefter. Ytterligere funksjoner som irreregulære bølger , fortøyningsliner og strøm bør implementeres for å muliggjøre studier av mer realistiske tilfeller.

Abbreviations

2D	Two dimensional
3D	Three dimensional
BiCGSTAB	Biconjugate Gradient Stabilized
CFD	Computational Fluid Dynamic
CFL	Courant-Friedrichs-Lewy number
CPU	Central Processing Unit
COG	Center of Gravity
EOM	Euler-Overlay Method
FFT	Fast Fourier Transformation
FPSO	Floating Production, Storage and Offloading
FVM	Finite Volume Method
GABC	Generating and Absorbing Boundary Condition
GB	Gigabyte
GPGPU	General Purpose Graphic Processing Unit
HPC	High Performance Computing
ILU	Incomplete Lower Upper
JIP	Joint Industry Project
JONSWAP	Joint North Sea Wave Observation Project
KVLCC	Korean Institute of Ship and Ocean Engineering Very Large Crude Carrier
LHF	Local Height Function
Lpp	Length between perpendiculars
MACHO	Multi-dimensional Advective Conservative Hybrid Operator
MARINE	Maritime Research Institute Netherlands
MODU	Mobile Offshore Drilling Unit
NTNU	Norwegian University of Science and Technology
NVMe	Non-Volatile Memory express
OA	Order of Accuracy
PB	Petabyte
PLIC	Piecewise Linear Interface Calculation

QTF	Quadratic Transfer Function
RAO	Response Amplitude Operator
SOR	Successive Over Relaxation
Std	Standard deviation
SV	Slowly Varying
TB	Terabyte
TFLOPS	Tera Floating point Operations Per Seconds
URANS	Unsteady Reynolds Averaging Navier-Stokes
Var	Variance
VOF	Volume of Fluid
VPN	Virtual Private Network
VTK	Visualization Toolkit

Nomenclature

A	Added mass, Amplitude
$A^{x,y,z}$	Edge apertures
B	Damping, Beam
C	Stiffness
D	Draught
F	Force
F^b	Volume aperture
F^s	Volume fraction
H	Curvature
H_s	Significant wave height
L	Length
M	Mass
$\boldsymbol{M}(t)$	Fluid momentum
N	Newton, Number of wave components
R	False reflection amplitude
R_H	Reflection coefficient
$R(\alpha, \beta, \gamma)$	General rotation matrix
S	Closed surface
S_B	Body surface
$\mathrm{S}(\omega)$	Wave energy spectrum
T_p	Peak period
T_{jj}^{ic}	Transfer function
$\boldsymbol{V}$	Fluid velocity vector
c	Phase velocity
$\boldsymbol{g}$	Gravity acceleration vector
h	Water depth
h(z,t)	Local height function
k	Wave number
m	Meter

$\boldsymbol{n}$	Normal vector
p	Pressure
$r_{i,j,k}$	Refinement ratio
s	Seconds
s(x,z,t)	Level set function
$\boldsymbol{u}$	Velocity vector
ζ_a	Wave amplitude
α	Angle of incident, Roll angle
β	Wave propagation angle, Pitch angle
γ	Yaw angle
ω	Angular wave frequency
ϕ	Velocity potential
η	Wave elevation
λ	Wave length
Ω	Fluid volume
τ	Brard number
ρ	Water density
μ	Dynamic viscosity
ν	Kinematic viscosity
ϵ	Phase, Order of accuracy
θ	Real angle of incident waves
Θ	Angle between x-axis and tangential vector
Δ	Mass displacement
∇	Gradient operator

Contents

List of Figures

List of Tables

Chapter 1

Introduction

1.1 Motivation

Floating production and mobile offshore drilling units (MODU) are often exposed to harsh sea states, including wind, waves, and current. Mooring line failures for floating production and MODU's occurs almost every year, see Figure 1.1a, and overload has been identified as one of the reasons for line failure during heavy weather. This has brought to light the need for improved procedures, methods, and standard industry practice. A joint industry project (JIP), EXWAVE, was started in 2015 to review and improve industry practice. Since the problem was detected, the number of line failures has been significantly reduced, see Figure 1.1.

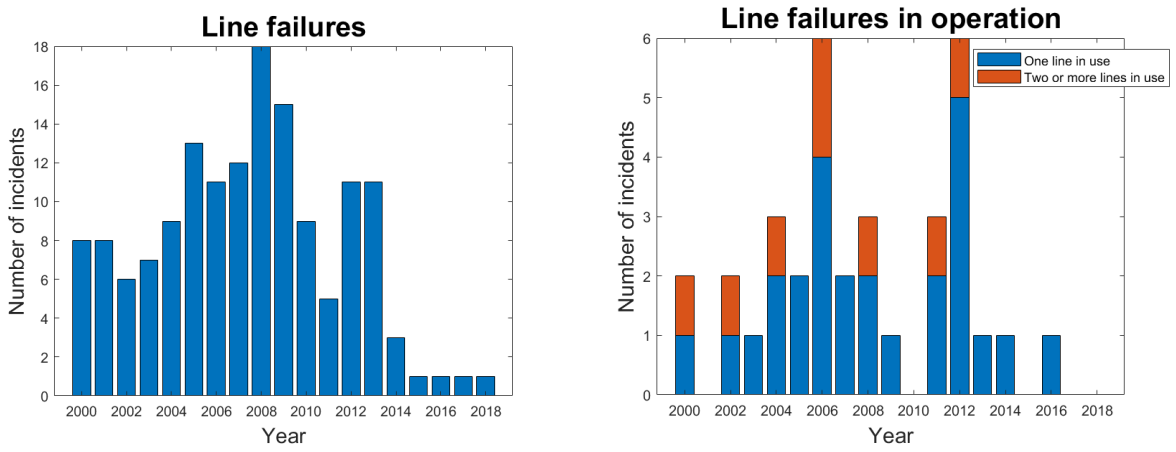

(a) Line failures.

(b) Line failures in operation.

Figure 1.1: Line failures in the Norwegian sector between year 2000 and 2018 (The Petroleum Safety Authority Norway - PSA, 2019).

When designing a station-keeping system for a ship-shaped structure, the slowly varying wave drift forces are important to consider. If the oscillation frequency coincides with any of the natural frequencies of the structure, large motions can be induced, causing severe mooring-line forces. For turret moored vessels, slowly varying forces in surge can become particularly large. This is because the ship is normally positioned with the bow against the waves to minimize the wave impact, causing the surge component to be the most significant contributor to the response of the mooring line. Another reason why the drift force in surge is intensified is because wind and waves are often found to be collinear for the most severe weather conditions (Hanssen, Bruschi, & Pettersen, 2013).

Drift forces and higher order forces are difficult to predict. Experience and experiments show that the forces, in general, are underpredicted. Normal practice is to assume the drift forces as weakly non-linear and estimate the forces using potential flow theory, including the terms up to the second order. This theory assumes small wave heights and small motions of the structure (Pinkster, 1980). This will not necessarily be valid assumptions for more severe sea states. Hence, the underprediction is most significant for higher and steeper waves.

The geometry, body motion, waves, wind, and current all affect the mean drift forces. Figure 1.2 shows the mean drift force for an FPSO in head sea waves with a current of 1 m/s and without current. A large deviation between the mean drift forces can be observed from the plot, especially for periods below 12 s. This indicates the importance of including current in the calculation of mean drift forces. Faltinsen (1999) reports that a current of 1 m/s may increase the drift forces with as much as 50%.

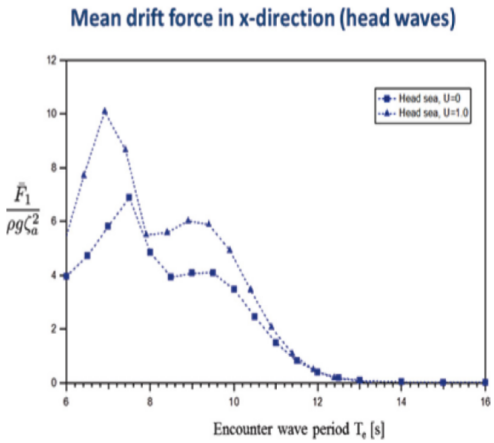

Figure 1.2: Wave drift coefficients for an FPSO with and without current present (Stansberg et al., 2015).

1.2 Objective

The main objective of this master thesis is to investigate the importance of nonlinear wave-body interaction effects on the FPSO drift loads in waves, focusing on the mean drift loads in surge. The target of the thesis will be completed using the Computational Fluid Dynamics (CFD) solver ComFLOW, and comparing the results to the outcome of the linear potential solver Wadam.

1.3 Thesis Outline

Chapter 1-5 and 7 contain contributions from the project thesis in addition to several new parts added in the master thesis. The analysis using the potential code Wadam, was completed as a part of the project thesis during the fall of 2019.

Chapter 2 gives a brief technical description of an FPSO and some typical locations.

Chapter 3 is devoted to the theory behind the software employed in the thesis, focusing on the mean drift loads.

Chapter 4 presents the state of the art methods and results from relevant literature.

Chapter 5 describes the assumptions and features of the software.

Chapter 6 focuses on the computational setup and extra computational resources utilized for the calculations.

Chapter 7 covers the convergence test and results from Wadam for three different bow geometries.

Chapter 8 presents the convergence test and the results from ComFLOW for a fixed and floating FPSO for three different wave steepnesses. The three different bow geometries are compared for both fixed and floating FPSO's for one period and one wave steepness.

Chapter 9 gives a conclusion and recommendations for further work.

Chapter 2

FPSO

FPSO stands for Floating Production, Storage and Offloading, and is a vessel type widely used within the oil and gas industry. The entity consists of a ship hull fitted with a production system for crude oil, separating oil and gas from water and other particles. These types of vessels are especially suitable at locations where the infrastructure for pipelines do not exist, locations with harsh weather and locations close to shore that do not have good market conditions, or political or local conditions that entice doing business (Leffler, Pattarozzi, & Sterling, 2003).

The North Sea is a typical location where harsh weather and lack of pipeline infrastructure are motivations for using FPSO's. The vessel is anchored up to minimize the impact of the weather. The vessel aims to position itself with the bow towards the incoming waves, wind, and current, to keep the drift forces and the roll motion to a minimum. This is called weathervaning (Van Dokkum, 2016). To be able to weather vane the FPSO, a turret is commonly used. A turret is a large mooring component located either internally or externally at the FPSO. The location depends on the weather conditions. If the FPSO is anchored at a location with harsh weather the turret is placed internally to protect the risers coming from the seabed. For locations with milder environmental conditions, like outside the coast of Africa, the turret can be cantilevered off the stern or the bow.

Typical natural periods of an FPSO are given in Table 2.1. The most relevant degrees of freedom when considering the drift forces for a moored vessel are the surge, heave, and pitch motions.

Table 2.1: Natural periods in all six degrees of freedom for an FPSO (Nestegård & Fonseca, 2017).

Natural periods	Surge	Sway	Heave	Roll	Pitch	Yaw
FPSO $[s]$	>100	>100	5-12	5-30	5-12	>100

The design and characteristics of an FPSO depend on its location and the environmental condition there. Typical sea states for different locations are given in Table 2.2 (DNV GL, 2015). As can be observed from the table, there are large differences in T_p and H_s, with more than 10 m difference in 100 years return period H_s between West Africa and the North Sea. Such large differences in weather conditions are one of the reasons for the diversity in the design of FPSO's.

Table 2.2: Typical 100 year sea states for West Africa, Brazil and the North Sea (DNV GL, 2015).

	West Africa	Brazil	North Sea
H_s $[m]$	2.5 - 6.1	8.0	14.0 - 16.5
T_p $[s]$	7.5 - 19.1	13.0	15.0 - 19.0

Norne, Brasil, and Adolo are examples of FPSO's located at three different sites and represent three distinctive designs. Figure 2.1 illustrates the vessels. Norne is located in the North Sea and has a narrow front with flare, while Brasil operated outside Brazil, but is now recycled, and had a more oval shape with a bulb. BW's FPSO Adolo is situated outside the coast of West Africa and is even wider than Brasil, and has no flare close to the free surface. Their design is a direct consequence of the environmental conditions at the site of operation, making the requirements for sea-keeping far more demanding for Norne than for Adolo. Looking at Figure 2.1 Adolo has a hull with vertical sides making it a cheaper construction, while Norne has a more complex shape. The three distinctive FPSO's are used as inspiration for the geometries tested in this thesis.

(a) The FPSO Norne (Equinor, 2008)

(b) The FPSO Brasil (Sea2Cradle, 2015)

(c) The FPSO Adolo (BW Offshore, 2018)

Figure 2.1: The FPSO's Norne, Brasil and Adolo.

Chapter 3

Theoretical Framework

3.1 Second-order loads

3.1.1 Potential theory

In the first part of this thesis, the potential flow theory is used to calculate the second-order loads. The problem is linearized using the perturbation method, assuming small waves and small body motions. For the potential flow theory to be valid, the fluid is assumed inviscid and incompressible, wile the fluid motion is assumed irrotational. The free surface boundary conditions are satisfied at the mean free surface, at z = 0. The motivation for a higher-order solution is to model the physics more accurately, taking into account the instantaneous position of the body. Another motivation is to improve the predictions of the non-linearities in the velocities of the fluid particles at the free surface. When considering second-order problems, the solution is still not exact, only a more accurate approximation than the linear solution.

The mean drift forces within potential flow theory are caused by the ability of the structure to generate waves. It is found by integrating the fluid pressures on the submerged part of the vessel. In an ideal fluid the drift forces have four contributions. The first is the pressure from the relative water elevation. The second is due to a drop in pressure because of the first-order velocity squared. The third originates from pressure from first-order pressure on a moving object due to first-order motions, and the last component comes from pressure from the product of the first-order initial forces and the first-order rigid body rotations (Hanssen et al., 2013). Waves that give large relative motions between the structure and the fluid cause significant drift forces. These drift forces are, to be shown in the following sections, proportional to the square of the wave amplitude. Short waves cause small relative motions but contribute to the drift forces because the

body diffracts the waves back into the incoming waves.

There are two ways of calculating the mean wave loads from the second-order effects using linear potential flow theory; the direct pressure integration method and the method of conservation of fluid momentum (Faltinsen, 1999).

3.1.2 Nonlinear theory

In the second part of the thesis, CFD is used to enable to study a more authentic situation of the drift forces since the problem becomes simplified in potential flow theory. A more realistic procedure is to calculate the pressure from the Poisson equation, with its parameters calculated from the Navier-Stokes equation. The Navier-Stokes equation considers the fluid as incompressible, but viscous and rotational. CFD permits the calculation of the pressure taking into account the instantaneous position of the free surface and the actual location of the body. When the pressure is calculated, the mean drift forces can be found using the direct pressure integration method (Van Der Plas, 2018).

Many parameters are affecting the drift forces, among them are the environmental data, significant wave height, wave period, and direction. As demonstrated in Figure 1.2 the current may significantly affect the mean drift forces. Also, the mooring and forward speed in addition to the geometrical shape of the structure may affect the slow drift motions (Greco, 2018).

3.2 The direct pressure integration method

One way to calculate the mean drift forces is by directly integrating the pressure on the surface of the body, Equation (3.1). $\boldsymbol{F}$ is a vector with the forces on the body in x-, y- and z-direction, S_B is the body surface, p is the pressure and $\boldsymbol{n}$ is the normal vector (Greco, 2018).

$$\boldsymbol{F} = \int_{S_B} p\,\boldsymbol{n}\,dS \tag{3.1}$$

The mean drift forces come from the body-wave interaction. In second-order solutions, the time variation of the relative motion between the vessel and the water is taken into account. Parts of the body will partly be over and under water. Integrating the pressure over the instantaneous wetted surface will result in a non zero mean force. The motion

of the body modifies the linear dynamic pressure, and if there are rotations, the normal vector will be affected by time variations. Another contribution to the second-order loads is the quadratic part of the pressure from the Bernoulli equation at the structure. Assuming no forward speed, steady state condition, and regular deep water incident waves, the solution of the second-order problem with two wave frequencies, ω_1 and ω_2, is presented in Equation (3.2). $\phi_1(\omega)$ is the first-order velocity potential and $\phi_2(\omega_1, \omega_2)$ is the second-order solution, consisting of the difference wave frequency velocity potential $\phi_2(\omega_1 - \omega_2)$, the sum wave frequency velocity potential $\phi_2(\omega_1 + \omega_2)$ and a mean value. In regular incident waves, only one wave frequency is present, meaning that the second-order effects originate from the sum wave frequency behavior and the mean value (Greco, 2018).

$$\phi = \phi_1(\omega_1) + \phi_1(\omega_2) + \phi_2(\omega_1, \omega_2) \xrightarrow{\omega} \phi = \phi_1(\omega) + \phi_2(2\omega) \tag{3.2}$$

The Bernoulli equation is used to find the pressure when potential theory is assumed. Equation (3.2) introduced in the Bernoulli equation gives the correct pressure up to the second-order:

$$p = -\rho \left(gz + \frac{\partial \phi_1}{\partial t} + \frac{\partial \phi_2}{\partial t} + \frac{1}{2} \nabla \phi_1 \cdot \nabla \phi_1 \right) \tag{3.3}$$

p is the pressure, ρ is the density of the fluid, g is the gravitational acceleration, z is a coordinate in the z-direction, and t is time. As seen from the equation, both the linear and the second-order problem must be solved to find the second-order loads. To be shown, only the square power of the first-order velocity contributes to the mean drift forces. Defining the first-order velocity potential for the incident waves as $\phi_1 = C(z)cos(\omega t - kx)$, the square power of the first-order velocity potential will depend on $cos^2(\omega t - kx)$ which has a non zero mean value. $C(z)$ is a function of z, ω is the wave frequency, t is time, k is the wave number, and x is the coordinate in the x-direction. Let $\phi_2 = A + Bcos(2\omega t + \epsilon)$, where A and B are constants, be the second-order velocity potential. Using the Bernoulli equation, keeping all terms that are proportional to ζ_a^2, gives:

$$-\rho \frac{\partial \phi_2}{\partial t} = \rho 2\omega B sin(2\omega t + \epsilon) \tag{3.4}$$

Hence, taking the mean over one period of Equation (3.4) will result in a mean value of

zero. All information needed is therefore found in the linear first-order solution. Another way to justify that Equation (3.4) does not need to be solved, is by observing that it consists of a sum frequency, which is not relevant for slowly varying forces. Setting the term depending on the second-order potential to zero in Equation (3.3) gives Equation (3.5).

$$p = -\rho g z - \rho \frac{\partial \phi_1}{\partial t} - \frac{\rho}{2}\left(\left(\frac{\partial \phi_1}{\partial x}\right)^2 + \left(\frac{\partial \phi_1}{\partial z}\right)^2\right) \tag{3.5}$$

Rewriting Equation (3.5) and generalizing the equation to cover all structures, the result is presented in Equation (3.6) (Faltinsen, 1999). β is the wave propagation angle, positive counter-clockwise when the waves propagate in the positive x-direction. n_i is the normal vector in direction i and l is the tangential vector. θ is the angle between the x-axis and the tangential vector.

$$\overline{F}_i = \frac{\rho g \zeta_a^2}{2} \int_{L_1} sin^2(\theta + \beta) n_i dl \qquad i = 1, .., 6 \tag{3.6}$$

When the expression for the mean drift forces is established for regular waves, the expression for the irregular sea can be obtained. The sea state is described by a wave spectrum S(ω). Examining Equation (3.6), it reveals that the drift loads are proportional to the wave amplitude squared, ζ_a^2. Correspondingly $\bar{F}_i/\zeta_a^2$ is independent of the wave amplitude, which makes it a transfer function for the mean drift forces for a regular sea state (Greco, 2018). By multiplying the transfer function with the wave amplitude $A_j^2 = S(\omega_j)\frac{\omega_{max}-\omega_{min}}{N}$ and summing all the N wave components for the mean wave drift forces, the expression for an irregular sea states is obtained. Writing it on the integral form:

$$\bar{F}_i^s = 2 \int_0^\infty S(\omega)(\frac{\bar{F}_i(\omega, \beta)}{\zeta_a^2}) d\omega \qquad i = 1, ..., 6 \tag{3.7}$$

3.3 The method of conservation of fluid momentum

Another way to calculate the mean wave drift force is by the conservation of fluid momentum. If S is a closed surface, Equation (3.8) expresses the conservation of momentum inside the surface.

$$\boldsymbol{M}(t) = \iiint_{\Omega} \rho \boldsymbol{V} d\tau \tag{3.8}$$

$\boldsymbol{M}(t)$ is the fluid momentum that changes with time. Ω is the volume of the fluid, and $\boldsymbol{V}$ is the fluid velocity in x-, y- and z-direction. Both volume and velocity may change with time, which gives Equation (3.9). Where U_n is the normal component of the velocity of the surface.

$$\frac{d\boldsymbol{M}}{dt} = \rho \iiint_{\Omega} \frac{\partial \boldsymbol{V}}{\partial t} d\tau + \rho \iint_{S} \boldsymbol{V} U_n ds \tag{3.9}$$

Assuming an incompressible fluid and using Gauss theorem to integrate over the surface instead of the volume, Equation (3.10) can be derived. The equation below gives the forces in both horizontal and vertical directions. V_n denotes the normal component of the fluid velocity at the surface.

$$\frac{d\boldsymbol{M}}{dt} = -\rho \iint_{S} ((\frac{p}{\rho} + gz)\boldsymbol{n} + \boldsymbol{V}(V_n - U_n))ds \tag{3.10}$$

For a freely floating structure, the force acting on the body is equal to the pressure integrated on the surface of the body. Since the $\iint_s p_0 \boldsymbol{n} ds = 0$, the pressure can be defined as equal to the difference between the atmospheric pressure and the pressure in the fluid, which implies that p equals zero on the free surface. When time averaging Equation (3.10) over one period the change in momentum depending on time is zero. This gives the expression for the average force in surge and sway, Equation (3.11). The term including $\rho g z$ in Equation (3.10) does not contribute in the horizontal direction. The equation is independent of the second-order velocity potential for the same reason explained in Section 3.2. The velocities and normal vectors are defined in Figure 3.1.

$$\bar{F}_i = -\overline{\iint_{S_\infty} (p n_i + \rho V_i V_n) ds} \tag{3.11}$$

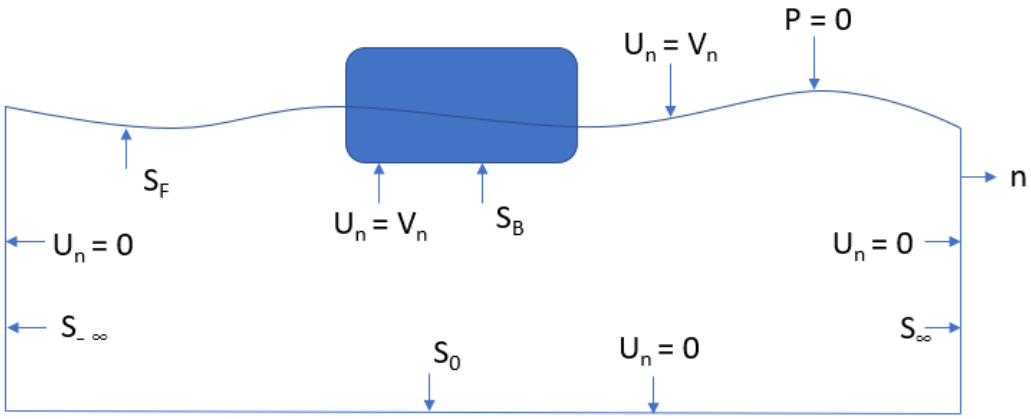

Figure 3.1: Control surface.

3.4 Quadratic transfer function

A structure moored in the open sea is subjected to waves, current, and wind causing slow drift motions. At least two wave frequencies are needed to cause second-order difference frequency effects creating low-frequency motions (Greco, 2018). The slow drift loads are usually considered to be inviscid forces, and can therefore be calculated from potential wave theory. This is an approximation that for severe sea states may turn out to be inaccurate. In extreme sea states, the nonlinear viscous contribution may be significant (DNV GL, 2019a). However, when viscous effects are neglected the relation between the slowly varying forces and and the squared wave amplitude can be expressed using a set of quadratic transfer functions. This is further described below.

In a sea state with N incoming wave frequencies ω and with wave amplitudes $A_i = \sqrt{2S(\omega_i)\partial\omega}$, where S($\omega_i$) is the wave spectrum, the slowly varying forces oscillates with the difference frequency $\omega_k - \omega_j$. According to Faltinsen (1999) the second-order slowly varying loads can be written as in Equation (3.12). Where T_{jk}^{ic} and T_{jk}^{is} are quadratic transfer functions (QTF), the real and the imaginary part respectively.

$$F_i^{SV}(t) = \sum_j^N \sum_k^N A_j A_k (T_{jk}^{ic} cos((\omega_k - \omega_j)t + (\epsilon_k - \epsilon_j)) + T_{jk}^{is} sin((\omega_k - \omega_j) + (\epsilon_k - \epsilon_j))) \quad (3.12)$$

The expression includes both mean and slow drift forces. Rewriting the equation above

for two incoming regular waves, the mean and slow drift components can be written separately, Equation (3.13).

$$\begin{aligned} F_i^{SV} &= (A_1^2 T_{11}^{ic} + A_2^2 T_{22}^{ic}) \qquad [mean \quad drift] \\ &+ A_1 A_2((T_{12}^{ic} + T_{21}^{ic})cos((\omega_2 - \omega_1)t) + (T_{12}^{is} - T_{21}^{is})sin((\omega_2 - \omega_1)t)) \qquad [slow \quad drift] \end{aligned} \tag{3.13}$$

For N incoming waves the mean drift force can be stated as $\sum_{j=1}^{N} A_j^2 T_{jj}^{ic}$. This corresponds to the diagonal terms for the transfer function where $\omega_j = \omega_k$. The mean drift forces are also expressed in Equation (3.7). Setting the expressions equal to each other, and rearranging it to consider the transfer function, the following equation is obtained:

$$T_{jj}^{ic} = \frac{\bar{F}_i(\omega_j, \beta)}{\zeta_a^2} \tag{3.14}$$

Equation (3.14) demonstrates that the second-order transfer function T_{jj}^{ic} depends on the slow drift load in i-direction, $\bar{F}_i$, caused by waves with frequencies ω_j and the amplitude squared. β is in this thesis, which only considers head sea waves, a constant of 180°. The mean slow drift force only depend on the linear first-order solution, proved in Section 3.2, consequently the second-order transfer function T_{jj}^{ic} only depend on the linear first-order potential solution.

3.4.1 Newman's approximation

The off diagonal terms do not only depend on the first-order solution, thus they are more complicated and time consuming to calculate. To reduce the computer time and avoid calculating the second-order velocity potential, Newman proposed an approximation to the problem. The contribution to the off diagonal terms depends on the difference in frequency $\omega_k - \omega_j$. Hence, the off diagonal transfer functions are the second-order difference frequency forces, see the second term in Equation (3.13). The most significant contribution by the difference frequency is when it is close to resonance. The approximation is good when $\omega_k = \omega_j$, which corresponds to small frequencies, coinciding with large motions, and this is the case for the surge motion of a catenary moored FPSO. Another reason this is a good approximation is that T_{jk}^{ic} and T_{jk}^{is} normally does not change much with the frequency.

Newman proposed the definitions $T_{jk}^{ic} = T_{kj}^{ic}$ and $T_{jk}^{is} = -T_{kj}^{is}$. Which implies that:

$$\begin{aligned} T_{jk}^{ic} = T_{kj}^{ic} &\simeq \frac{1}{2}(T_{jj}^{ic} + T_{kk}^{ic}) \\ T_{jk}^{is} = T_{kj}^{is} &\simeq 0 \end{aligned} \tag{3.15}$$

From the two approximations in Equation (3.15) it follows that $T_{jj}^{ic} \simeq T_{kk}^{ic}$. By setting the arithmetic average equal to the geometric average the following relation is obtained: $\frac{1}{2}(T_{jj}^{ic} + T_{kk}^{ic}) \simeq \sqrt{T_{jj}^{ic} T_{kk}^{ic}}$ (Greco, 2018). The consequence of applying these relations is that the double summation can be reduced to the square of a simple summation. This reduces the computational cost from adding N^2 terms to only adding N terms. This simplification is derived in Equation (3.16).

$$\begin{aligned} F_i^{SV} &= \sum_{j=1}^{N}\sum_{k=1}^{N} A_j A_k \sqrt{T_{jj}^{ic} T_{kk}^{ic}} (cos((\omega_k - \omega_j)t + (\epsilon_k - \epsilon_j)) + cos((\omega_k + \omega_j)t + (\epsilon_k + \epsilon_j))) \\ &= 2\sum_{j=1}^{N}\sum_{k=1}^{N} A_j A_k \sqrt{T_{jj}^{ic} T_{kk}^{ic}} cos(\omega_j t + \epsilon_j) cos(\omega_k t + \epsilon_k) \\ &= 2(\sum_{j=1}^{N} A_j \sqrt{T_{jj}^{ic}} cos(\omega_j t + \epsilon_j))^2 \end{aligned} \tag{3.16}$$

According to DNV GL (2019a) the Newman approximation gives satisfactory results for horizontal slow drift motions for large volume structures with low natural frequencies in surge, sway, and yaw when there is no current and no forward speed. On the other hand, it can be shown that the Newman approximation may underestimate the drift forces especially for the vertical motions of an FPSO (Nestegård & Fonseca, 2017). In such cases, the full transfer matrix should be applied. Also, for shallow water, the full matrix should be used, because the Newman approximation is based on the first-order solution which may be inaccurate for shallow water.

3.5 Governing equations

With CFD more realistic cases can be solved, with fewer simplifications of the problem and fewer approximations in the calculations.

3.5.1 Navier-Stokes equation

The Navier-Stokes equation is in practical marine application the equation of conservation of fluid momentum (Greco, 2018). The Navier-Stokes equation for an incompressible fluid is presented in Equation (3.17).

$$\rho\frac{\partial \boldsymbol{u}}{\partial t} + \rho\boldsymbol{u}\cdot\nabla\boldsymbol{u} = -\nabla p + \mu\nabla\cdot\nabla\boldsymbol{u} + \rho\boldsymbol{F} \tag{3.17}$$

Where the $\rho\frac{\partial \boldsymbol{u}}{\partial t}$ gives the fluctuation of pressure with respect to time. $\rho\boldsymbol{u}\cdot\nabla\boldsymbol{u}$ is the convective term, while $-\nabla p$ is the gradient of pressure, and $\mu\nabla\cdot\nabla\boldsymbol{u}$ is the viscous diffusion term (H.T. Ok & Choi, 2016). $\boldsymbol{u}$ is the velocity vector, t is time, ρ is the water density, p denotes the pressure, μ is the dynamic viscosity and $\boldsymbol{F}$ is the external force, for instance, the gravitational force (Van Der Plas, 2018).

Equation (3.18) is the continuity equation for an incompressible fluid, and serves as a kinematic constraint for Equation (3.17) assuring mass conservation. ∇ is the gradient operator.

$$\nabla\cdot\boldsymbol{u} = 0 \tag{3.18}$$

3.5.2 Poisson equation

To derive the coupling between velocity and pressure, the divergence operator is applied to the Navier-Stokes equation, and together with the continuity equation, the Poisson equation for pressure is obtained. To get the discretized Poisson equation, Equation (3.17) needs to be discretized forward in time. Then the pressure is given at n+1 with the corresponding velocity at n+1.

$$\boldsymbol{u}^{n+1} = \boldsymbol{u}^n + \Delta t\left(-\boldsymbol{u}^n\cdot\nabla\boldsymbol{u}^n - \frac{1}{\rho}\nabla p^{n+1} + \nu\nabla^2\boldsymbol{u}^n\right) \tag{3.19}$$

In Equation (3.19) n is the time step number, Δt is the size of the time step, and $\nu = \frac{\mu}{\rho}$ is the kinematic viscosity. The divergence of the discretized momentum equation gives Equation (3.20).

$$\nabla \cdot \boldsymbol{u}^{n+1} = \nabla \cdot \boldsymbol{u}^{n} + \Delta t \left(-\nabla \cdot (\boldsymbol{u}^{n} \cdot \nabla \boldsymbol{u}^{n}) - \frac{1}{\rho} \nabla^2 p^{n+1} + \nu \nabla^2 (\nabla \cdot \boldsymbol{u}^{n}) \right) \tag{3.20}$$

To satisfy continuity, the divergence of $\boldsymbol{u}$ has to be zero at the next time step, but because of numerical error the current step gives $\nabla \cdot \boldsymbol{u}^{n} \neq 0$. The divergence of the velocity is therefore not zero. To correct for this, the momentum equation is first solved as an intermediate step. Then the Poisson equation is solved for the pressure, forcing the divergence of the velocity to be zero. The velocity is then corrected to satisfy the continuity equation.

The Poisson equation is presented in Equation (3.21).

$$\nabla^2 p^{n+1} = \rho \frac{\nabla \cdot \boldsymbol{u}^{n}}{\Delta t} - \rho \nabla \cdot (\boldsymbol{u}^{n} \cdot \nabla \boldsymbol{u}^{n}) + \mu \nabla^2 (\nabla \cdot \boldsymbol{u}^{n}) \tag{3.21}$$

3.6 Boundary Conditions

To solve the Navier-Stokes equation, given in Equation (3.17), boundary conditions are needed at the boundaries of the domain, the geometry and the free surface (Van Der Plas, 2018). For solid geometries or solid domain surfaces, the requirement of no passing fluid is set, which is presented in Equation (3.22).

$$\boldsymbol{u} = \boldsymbol{u_b} \tag{3.22}$$

Where $\boldsymbol{u}$ is the velocity. For a fixed geometry and solid domain boundaries, the no slip condition is given by $\boldsymbol{u_b} = \boldsymbol{0}$.

3.6.1 Free surface

At the free surface two boundary conditions are needed, one for the pressure and one for velocities. The displacement of the free surface is given by Equation (3.23) (Van Der Plas, 2018).

$$\frac{Ds}{Dt} \equiv \frac{\partial s}{\partial t} + (\boldsymbol{u} \cdot \nabla) s = 0 \tag{3.23}$$

$s(x,t) = z - \zeta(x,z,t)$ where $z = \zeta$ is the instantaneous position of the free surface, t is time, $\boldsymbol{u}$ is the velocity vector and ∇ is the gradient operator. Equation (3.23) is the kinematic boundary condition. The advection of the free surface is discretized using a multi-dimensional advective conservative hybrid operator (MACHO) direction-split scheme.

At the free surface the pressure is equal to the atmospheric pressure. Starting with the continuity for normal and tangential stress, Equation (3.24) and Equation (3.25) can be deduced (Van Der Plas, 2018).

$$-p + 2\mu\frac{\partial u_n}{\partial n} = -p_0 + 2\sigma H \tag{3.24}$$

$$\mu\left(\frac{\partial u_n}{\partial t} + \frac{\partial u_t}{\partial n}\right) = 0 \tag{3.25}$$

u_n is the normal component of the velocity, u_t is the tangential component of the velocity, p_0 is the atmospheric pressure, p is the fluid pressure, σ is the surface tension and $2H$ denotes the total curvature. If the viscous term is very small relative to the other terms, the condition can be simplified to $p = p_0 - 2\sigma H$ (Veldman, Gerrits, Luppes, Helder, & Vreeburg, 2007).

3.6.2 Domain

A considerable challenge in CFD is the application of boundary conditions at the boundaries of the computational domain. A small domain yields less computational cost, but a too small domain can result in large reflections from the boundaries, and therefore not give representative results. Hence, efficient boundary conditions can enable a reduction of the domain size.

The following is a presentation of the absorbing boundary condition given by Düz, Borsboom, Veldman, Wellens, and Huijsmans (2017). The absorbing boundary condition is only derived for one side of the domain, but the same procedure can be applied to find the other boundary conditions. The boundary condition accounts for dispersive and directional effects. Starting with the two-dimensional wave equation given in Equation (3.26).

$$\frac{\partial^2 \phi}{\partial t^2} = c^2 \left(\frac{\partial^2 \phi}{\partial x^2} + \frac{\partial^2 \phi}{\partial z^2} \right) \tag{3.26}$$

Where ϕ is the velocity potential, t is time and c is the phase speed of the wave. A solution of Equation (3.26) is presented in Equation (3.27).

$$\phi(x, z, t) = e^{i(k_x x + k_z z - \omega t)} \tag{3.27}$$

Where ω is the angular frequency, t is time and k_x an k_z are the wave numbers in x- and z-direction. Inserting the solution above into Equation (3.26), the following dispersion relation is achieved

$$\omega^2 = c^2(k_x^2 + k_z^2) \tag{3.28}$$

By demanding the suppression of waves reflected by the boundary on the right side, Equation (3.29) is obtained. This equation is a first-order non reflective boundary condition.

$$\left(\frac{\partial}{\partial t} + c \frac{\partial}{\partial x} \right) \phi = 0 \tag{3.29}$$

A higher-order non reflective boundary condition is the second-order Engquist-Majda boundary condition presented in Equation (3.30), (Düz et al., 2017)

$$\left(\frac{\partial}{\partial t} + c \frac{\partial}{\partial x} \right)^2 \phi = 0 \tag{3.30}$$

Transferring this to three-dimensions, the waves can have an angle of incidence α with the outflow boundary. The higher the order, p, of the boundary condition, the more angles can be chosen. For the three dimensional case, the boundary condition can be expressed with the Higdon's condition in Equation (3.31).

$$\prod_{p=1}^{P} \left(cos\ \alpha_p \frac{\partial}{\partial t} + c \frac{\partial}{\partial x} \right) \phi = 0 \tag{3.31}$$

The solution of Equation (3.31) is presented in Equation (3.32). The velocity potential is rewritten as the sum of outgoing and reflected waves. It now considers the presence of false reflections that are generated by each scheme as a function of the incident waves. The first term in the equation has an amplitude equal to the unit amplitude affecting the boundary, while the second part represents the false reflections from the boundary with an amplitude R.

$$\phi(x, y, t) = e^{i(k_x x + k_z z - \omega t)} + Re^{i(-k_x x + k_z z - \omega t)} \tag{3.32}$$

Imposing Equation (3.32) into the general Higdon boundary conditions in Equation (3.31), gives the reflection coefficient R_H presented in Equation (3.33). θ is the real angle of the incidence, measured in either clockwise or counter-clockwise direction from the positive x-axis, $|\theta| < \pi/2$. Düz et al. (2017) demonstrates that the second-order method outperforms the first-order method in terms of directional effects, by comparing the reflection coefficients.

$$|R_H| = \prod_{p=1}^{P} \left| \frac{cos\ \alpha_p - cos\ \theta}{cos\ \alpha_p + cos\ \theta} \right| \tag{3.33}$$

Dispersive absorbing boundary condition

The phase velocity in Equation (3.31) for the first-order, when $p = 1$, can be replaced by the dispersion relation in Equation (3.34). c is the phase speed, g is the gravitational force, h is the water depth and k is the wave number.

$$c = \sqrt{gh}\sqrt{\frac{tanh(kh)}{kh}} \tag{3.34}$$

The Higdon relation can be rewritten into Equation (3.35).

$$\left(cos\ \alpha \frac{\partial}{\partial t} + \sqrt{gh}\sqrt{\frac{tanh(kh)}{kh}} \right) \phi = 0 \tag{3.35}$$

Equation (3.35) is a perfectly absorbing boundary condition for one single wave frequency. As seastates normally consists of several wave frequencies that are superimposed, the

dispersion relation can be approximated to account for a range of wave frequencies present in the sea state. Equation (3.36) gives the approximation for the dispersion relation in Equation (3.34).

$$c_a \approx \sqrt{gh}\frac{a_0 + a_1(kh)^2}{1 + b_1(kh)^2} \tag{3.36}$$

c_a is the approximated phase velocity, and a_0, a_1 and b_1 are coefficients to be optimized. Choosing a_0, a_1, and b_1 wisely, this approximation is very accurate for a large range of kh values.

Approximating the wave potential to be $\phi \approx e^{ik(x-ct)}cosh\ k(h+z)$, Equation (3.37) is obtained. The wave number can then be calculated locally from the potential itself, which has the benefit that the wave number can be calculated during the analysis, and there is no need to set a value for k beforehand.

$$k^2\phi = \frac{\partial^2\phi}{\partial z^2} \tag{3.37}$$

Combining Equation (3.36) and Equation (3.37) into Equation (3.35), the final dispersion relation is obtained and presented in Equation (3.38).

$$cos\ \alpha\ \left(1 + b_1h^2\frac{\partial^2}{\partial z^2}\right)\frac{\partial\phi}{\partial t} + \sqrt{gh}\left(a_0 + a_1h^2\frac{\partial^2}{\partial z^2}\right)\frac{\partial\phi}{\partial x} = 0 \tag{3.38}$$

Dispersive directional absorbing boundary condition

The approach above only accounts for the dispersive effects. To also include the directional effects, a second-order Higdon's relation is applied. As mentioned, it outperform the first-order relation in terms of directional effects. When $p = 2$, the Higdon's relation can be expanded with Equation (3.31). Observed from the equation, is the fact that the velocity potential can only be included in one of the operators, $cos\,\alpha_p\frac{\partial}{\partial t} + c\frac{\partial}{\partial x}$. This is because the product of two approximations will require a fourth derivative in the z-direction causing complications in the discretization of the boundaries. This gives Equation (3.39).

$$\left(cos\ \alpha_1\frac{\partial}{\partial t} + c\frac{\partial}{\partial x}\right)\left(cos\ \alpha_2\frac{\partial\phi}{\partial t} + c\frac{\partial\phi}{\partial x}\right) = 0 \tag{3.39}$$

Substituting Equation (3.36) and Equation (3.37) into Equation (3.39) gives the dispersive and directional absorbing boundary condition, Equation (3.40).

$$\left(cos\ \alpha_1 \frac{\partial}{\partial t} + c\frac{\partial}{\partial x}\right)\left(\left(1 + b_1 h^2 \frac{\partial^2}{\partial z^2}\right) cos\ \alpha_2 \frac{\partial \phi}{\partial t} + \sqrt{gh}\left(a_0 + a_1 h^2 \frac{\partial^2}{\partial z^2}\right)\frac{\partial \phi}{\partial x}\right) = 0 \tag{3.40}$$

In ComFLOW, a generating part, a wave maker, is added to the absorbing boundary condition for the inlet condition, making it a generating and absorbing boundary condition (GABC) (Van Der Plas, 2018).

3.7 Definition of grid and geometry

The governing equations are solved in a Cartesian staggered grid with a right-handed coordinate system. The velocities are solved at the faces of the grid, while the pressure is calculated in the center, as illustrated in Figure 3.2.

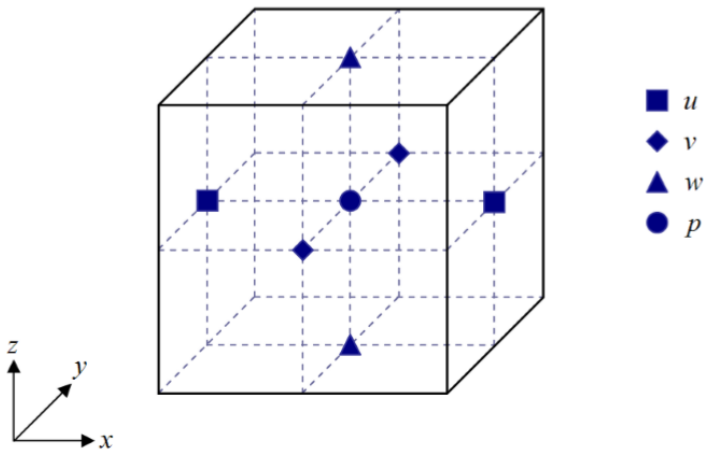

Figure 3.2: Fixed Cartesian grid with the locations of the velocities and pressure (Düz, Borsboom, Veldman, Wellens, & Huijsmans, 2017).

A disadvantage with a staggered Cartesian grid is that curved geometries are difficult to render. The geometry is not aligned with the grid. To avoid staircase geometries, the geometry is reconstructed with a piecewise linear approach, cutting through the cells, namely a cut-cell approach (Veldman et al., 2007). The geometry cuts through the cells to avoid regenerating the grid for each time step.

3.7.1 Grid setup and refinement

The grid is constructed by giving the number of cells desired in each direction of the domain. To save computational time and power and/or to obtain more accurate results, a local grid refinement or coarsening can be used. The change in the grid refinement is implemented such that the number of cells given in each direction forms level zero. For each new level higher than zero a refined grid with the refinement ratios r_i, r_j and r_k is created, and for levels lower than zero, a coarser grid is created with the same ratio r_i, r_j and r_k. The refinement ratios are by default set to 2, but can be chosen freely, including anisotropic combinations (Van Der Plas, 2018). Figure 3.3 demonstrates a grid with three different levels and a refinement ratio of 2. To capture the shape of the incident wave at least 60 cells per wave length are needed, and 6 cells in the wave height. For very steep waves a minimum of 10 cells in the wave height is recommended (Van Der Plas, 2018).

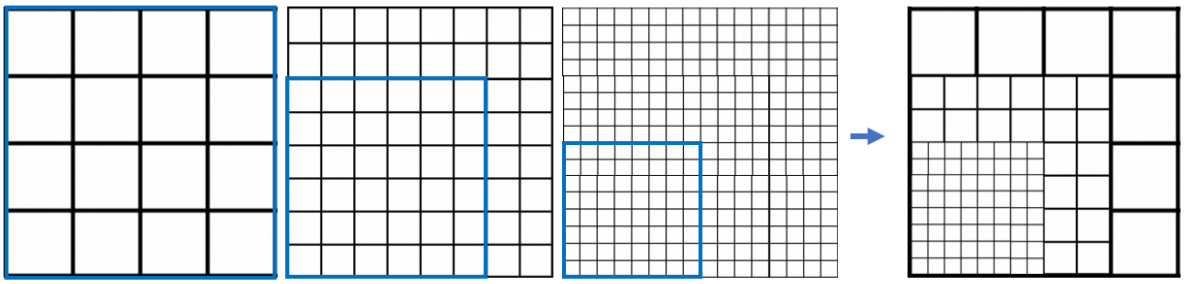

Figure 3.3: 2D grid refinement with a refinement ratio of 2 in both directions.

3.7.2 Volume and edge apertures

To be able to define the geometry, a finite element description is chosen, by introducing integration points in each grid cell. It controls if the points are inside or outside the geometry, and this is mapped to the staggered Cartesian grid (Kleefsman, 2005). Volume and edge apertures are introduced to define which part of the cell that are occupied by the geometry, and which part that is open for fluid. The edge apertures consist of two edges, A^x and A^z in 2D and three edges, A^x, A^y and A^z, in 3D, and are the integration points at the edge of the cell, indicated with crosses in Figure 3.4. The edge apertures are obtained by counting the points laying outside the geometry at the cell edge, circled in black, and dividing it on the total number of cells at the corresponding edge. The volume aperture is denoted F^b and calculated from the integration points inside the cell, indicated with small dots in Figure 3.4. F^b is found by summarizing the integration

points outside the geometry, encircled with blue, and dividing it on the total number of internal integration points. The volume and edge apertures indicate a fraction between zero and one.

More integration points yield higher accuracy. In Figure 3.4, the left cell has 2x2 integration points, which gives $A^x = \frac{1}{2} = 0.5$, $A^z = \frac{1}{2} = 0.5$ and $F^b = \frac{3}{4} = 0.75$. The right cell has 4x4 integration points, resulting in the edge apertures $A^x = \frac{2}{4} = 0.5$ and $A^z = \frac{1}{4} = 0.25$. The volume aperture for the cell is $F^b = \frac{11}{16} = 0.69$, the significant change of the apertures underlines the importance of sufficient discretization.

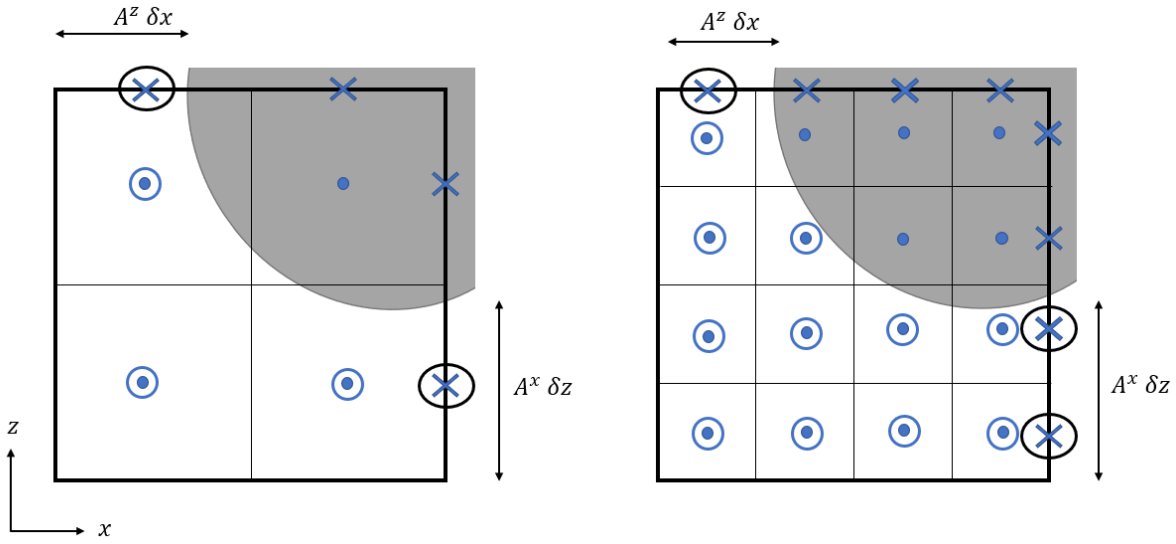

Figure 3.4: Volume and edge apertures.

ComFLOW has implemented two methods to calculate the volume and edge apertures, the *Legacy method*, and the *Exact method*. The *Legacy method* form on a point test. A lattice of integration points covers the grid, and every point located in the geometry contributes to the volume apertures. The *Exact method* is based on the exact intersections of polyhedrons. All intersections between the geometry and the computational cells are calculated, and their contribution adds up to the volume and edge aperture (Van Der Plas, 2018). For a moving geometry, the volume and edge apertures need to be recalculated for each time step.

3.7.3 Cell labeling

A fixed Cartesian grid is used when performing the computations of the governing equations in ComFLOW. When introducing the grid, cells of different characteristics emerge.

Volume and edge apertures are introduced, and handle the different characters as described in Section 3.7.2. Depending on the volume and edge apertures, the cells are labeled to explain what kinds of cells they are. Figure 3.5 demonstrates an example of cell labeling of the bow of an FPSO. The labels are E-Empty, S-Surface, F-Fluid, and B-Boundary. The cells labeled E does not contain fluid. S is used to indicate the cells containing fluid in addition to having an empty neighbor cell. The cells that are completely inside the geometry are denoted B, while the rest are labeled F and contains fluid.

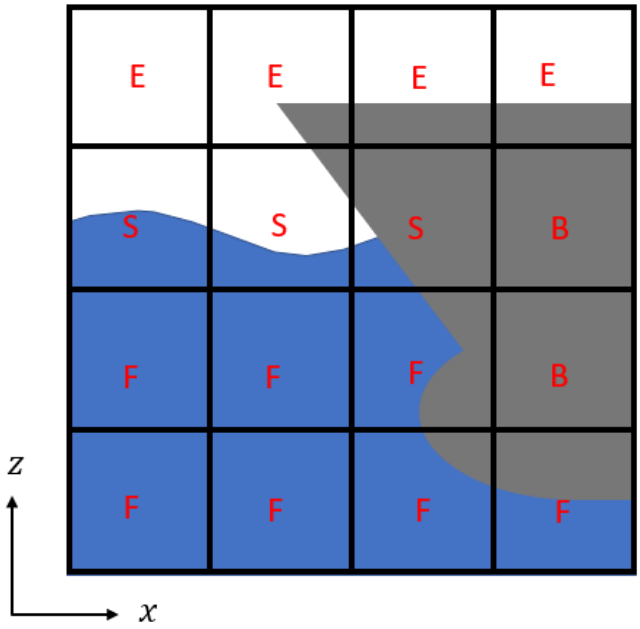

Figure 3.5: Cell labeling.

3.8 Volume of fluid method

The volume of fluid (VOF) method is used for tracking the free surface using a volume fraction function, F^s. The function is also called a free surface aperture and gives the fraction of fluid in a surface cell (Veldman et al., 2007). The free surface is displaced using the advection equation, Equation (3.41). Where F^s is the volume fraction function with values between zero and one, t is time, $\boldsymbol{u}$ is the velocity vector and ∇ is the gradient operator (Kleefsman, 2005). The relation between the volume aperture for the free surface and the geometry is given by $0 \leq F^s \leq F^b \leq 1$.

$$\frac{DF^s}{Dt} \equiv \frac{\partial F^s}{\partial t} + (\boldsymbol{u} \cdot \nabla)F^s = 0 \tag{3.41}$$

The free surface is reconstructed at each time step from VOF data, thereafter displaced using Equation (3.41). The VOF data is discretized using a piecewise linear interface calculation (PLIC) scheme (Van Der Plas, 2018). The scheme reconstructs the surface by a linear plane, defined by a normal vector and a plane constant. To calculate these variables the central method is applied.

3.8.1 Local Height Function

In the VOF method, the fluid is moved without considering where the main part of the liquid is positioned. A consequence is that nonphysical drops detach from the fluid during the advection of the free surface. These droplets are known as *jetsam* and *flotsam* (Wellens, 2012). It can lead to both gain and loss of mass. A Local Height Function (LHF) can be used to prevent the *jetsam* and *flotsam*, and secure mass conservation. For each surface cell, denoted S in Figure 3.5, a local function is defined giving the local height of the fluid in a column or row of three cells. The function is implemented for the surface cells because it is in this region the *jetsam* and *flotsam* occur. The spatial direction of the three cells is chosen depending on the normal of the free surface (Veldman et al., 2007).

Pressure in the free surface cells

The pressure at the free surface can be calculated from Equation (3.24). The pressure depends on the curvature, $2H$, of the free surface, and needs to be calculated for each surface cell and for each time step. The procedure for the calculation of the curvature follows in Section 3.8.1. When the curvature is known, the pressure can be calculated from Equation (3.24). The pressure is calculated in the center of each cell, as demonstrated in Figure 3.2, and can in the finite volume method (FVM) be assumed constant for the entire cell (Gerrits, 2001). Hence, the equation for the boundary condition for the pressure can be added directly to the Poisson equation, Equation (3.21).

Curvature of the free surface

The curvature of the free surface is needed for each surface cell to be able to solve Equation (3.24) for the pressure. If the free surface is described by the level set function

$s(x, z, t)$ from Equation (3.23), then the curvature can be described by Equation (3.42). Where H is the curvature, ∇ is the gradient operator, $\boldsymbol{n}$ is the normal vector of the free surface and s is the level set function (Gerrits, 2001).

$$H = \nabla \cdot \boldsymbol{n} \longrightarrow \boldsymbol{n} = \frac{\nabla s}{|\nabla s|} \tag{3.42}$$

The free surface is described locally in each surface cell by a height function. Depending on the orientation of the free surface, a horizontal or vertical height function is defined using the VOF fractions given in each cell in Figure 3.6. A grid of 3x3 around the surface cell for a 2D example, encircled in red in Figure 3.6, is used to decide if a horizontal or vertical local height function is to be applied. The absolute value of the difference between the values in the left and right center cells, and the top and bottom center cells, marked with blue in Figure 3.6, gives the orientation of the function. In the example in Figure 3.6 the difference in the horizontal plane corresponds to $|0.0 - 0.9| = 0.9$ and the vertical direction gives $|0.0 - 0.7| = 0.7$. Following the example of Gerrits (2001), the horizontal difference is large than the vertical, which corresponds to applying a vertical height function, see the right figure in Figure 3.6.

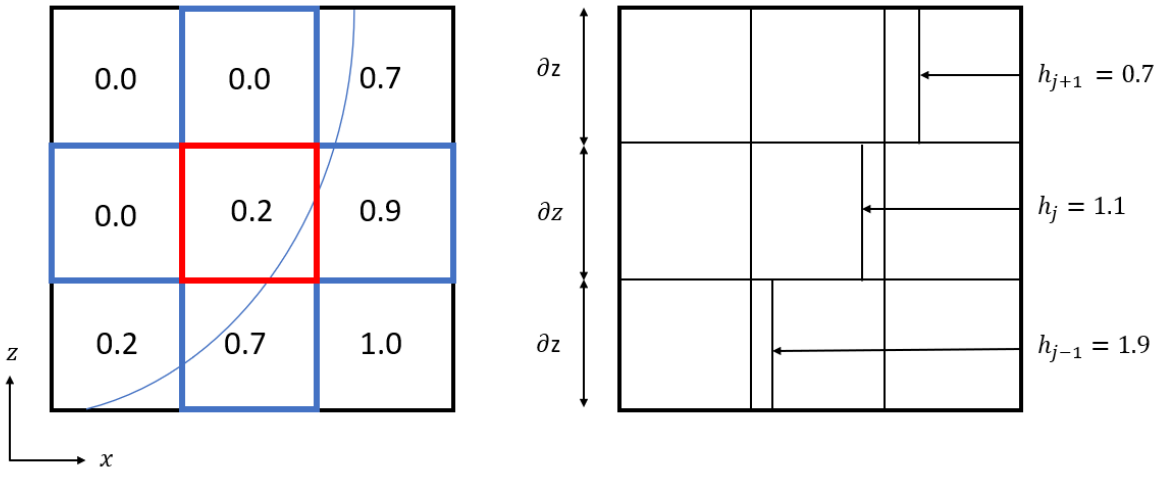

Figure 3.6: [Left] Free surface function, indicated with a blue line, and the VOF fractions in each cell. [Right] Discrete, vertical local height function corresponding to a surface cell S (Gerrits, 2001).

Another method to determine the orientation of the LHF is by inspecting the reconstructed normal of the free surface, $\boldsymbol{n} = (n_x, n_z)^T$. If $|n_x \partial x| > |n_z \partial z|$, a vertical local

height function is applied. Where ∂x and ∂z are the grid sizes in x- and z-direction with the corresponding normal vectors n_x and n_z respectively.

When the direction of the function is settled, a local height function is defined. In connection with the level set function, this coincide with $s(x, z, t) \equiv h(z, t) - x = 0$ where $x = h(z, t)$ is the LHF. Then the mean curvature can be described by Equation (3.43), (Gerrits, 2001). Where H is the curvature, h is the LHF, and ∂z is the grid size in the z-direction.

$$H = \frac{\partial}{\partial z}\left(\frac{\partial h/\partial z}{\sqrt{1 + (\partial h/\partial z)^2}}\right) \tag{3.43}$$

3.9 Motions

The coordinate system is a right-handed coordinate system. The positive directions and motions are illustrated in Figure 3.7.

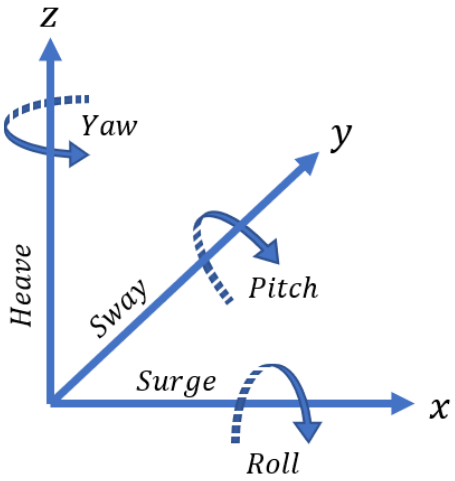

Figure 3.7: Right-handed coordinate system with positive motions and rotations labeled on the axis.

The full rotation matrix is given in Equation (3.44). It consists of the rotation matrices around the x-, y- and z-axis, where α denotes roll, β gives the pitch angle, and γ indicates yaw.

$$R(\alpha,\beta,\gamma) = \begin{bmatrix} cos\,\beta\,cos\,\gamma & -cos\,\beta\,sin\,\gamma & sin\,\beta \\ cos\,\gamma\,sin\,\alpha\,sin\,\beta + cos\,\alpha\,sin\,\gamma & cos\,\alpha\,cos\,\gamma - sin\,\alpha\,sin\,\beta\,sin\,\gamma & -cos\,\beta\,sin\,\alpha \\ -cos\,\alpha\,cos\,\gamma\,sin\,\beta + sin\,\alpha\,sin\,\gamma & cos\,\gamma\,sin\,\alpha + cos\,\alpha\,sin\,\beta\,sin\,\gamma & cos\,\alpha\,cos\,\beta \end{bmatrix} \tag{3.44}$$

The geometry rotates around its center of gravity, and the position of any point is given by Equation (3.45), (Kleefsman, 2005), where COG is the center of gravity, $R(\alpha,\beta,\gamma)$ is the general rotation matrix, x_{P_0} is the initial coordinates of the point and COG_0 is the original position of the center of gravity.

$$x_p = COG + R(\alpha,\beta,\gamma)(x_{P_0} - COG_0) \tag{3.45}$$

3.10 Waves

3.10.1 Airy waves

Equation (3.46) is the wave elevation for an Airy wave, which is a linear wave. A is the wave amplitude, ω is the wave frequency, k is the wave number and ϵ is the phase.

$$\eta(x,t) = A\,cos(\omega t - kx + \epsilon) \tag{3.46}$$

Because of the simplicity of the Airy wave theory, it is widely used by engineers (Fenton, 1985). Nevertheless, the theory is only valid for very low wave steepness, which in general is not representative for real waves of finite height.

3.10.2 Stokes waves

Stokes waves are defined according to Buffoni and Toland (2003) as a steady periodic irrotational water wave of finite depth, subjected to a gravitational force, but without surface tension. The theory for Stokes waves is derived using a trigonometric series (Skjelbreia & Hendrickson, 1960). The velocity potential for the fifth-order Stokes wave presented by Fenton (1985) is given in Equation (3.47). The fifth-order Stokes wave is commonly used in offshore and wave engineering, but the Stokes wave can be written out in any order. Because of the computational cost compared to accuracy, the first up

to fifth-order Stokes waves are commonly used. The waves are assumed periodic and the fluid is considered nonviscous, the water depth is constant, and that the waves are assumed to have infinite extent in the normal direction.

$$\phi(x,z) = -\bar{u}x + C_0 \left(\frac{g}{k^3}\right)^{1/2} \sum_{i=1}^{5} \epsilon^i \sum_{j=1}^{i} A_{ij}\, cosh(jkz)\, sin(jkx) + O(\epsilon^6) \tag{3.47}$$

$\bar{u}$ is the mean horizontal fluid speed, C_0 is a constant given by Fenton (1985), g is the gravitational acceleration, k is the wave number, ϵ denotes the order of accuracy, A_{ij} is the wave amplitude and the Landau symbol $O(\epsilon)$ gives the order of the terms that are neglected.

The equation for the free surface profile is presented in Equation (3.48). B_{ij} are different constants tabulated by Fenton (1985).

$$\begin{aligned} k\eta(x) = {} & kd + \epsilon\, cos\, kx + \epsilon^2\, B_{22}\, cos\, 2kx + \epsilon^3\, B_{31}\, (cos\, kx - cos\, 3kx) \\ & + \epsilon^4\, (B_{42}\, cos\, 2kx + B_{44}\, cos\, 4kx) \\ & + \epsilon^5\, (-(B_{53} + B_{55})\, cos\, kx + B_{53}\, cos\, 3kx + B_{55}\, cos\, 5kx) + O(\epsilon^6) \end{aligned} \tag{3.48}$$

Looking into the properties of the Stokes waves, it can be showed that the crests are higher, and the troughs are shallower, compared to the Airy waves (Myrhaug, 2000). For shallow water, the height of the crest increase and the depth of the troughs decreases. The Stokes waves are symmetric considering a vertical line through the crest or trough, hence it cannot describe nonlinear asymmetric waves.

For the highest Stokes waves, some additional properties apply. In the wave crest, the fluid particle velocity is the same as the wave velocity. To avoid breaking waves, the crest angle cannot become smaller than 120°. The steepness, s, can be expressed as a function of the wave height, see Equation (3.49), H, and the wavelength, λ. The critical value for a breaking Stokes wave is $1/7$ (Myrhaug, 2000).

$$s = \frac{H}{\lambda} \tag{3.49}$$

3.11 Spatial integration

The FVM is used for the spatial discretization of the Navier-Stokes equation, Equation (3.17), (Kleefsman, 2005).

3.11.1 Convective term

The convective term in Equation (3.17) is discretized using a first-order upwind scheme, which is the most stable numerical scheme. The scheme maintains the skew symmetric property of the convective term, which has beneficial consequences when assuring stability of the method, see Kleefsman (2005) for further details. The scheme can induce artificial viscosity causing damping of the waves (Kleefsman, 2005). A second-order upwind scheme can be utilized to achieve more accurate results but at the expense of stability. Artificial diffusion can be implemented to stabilize the discretization (Van Der Plas, 2018).

3.11.2 Diffusive term

ComFLOW supports two discretization schemes for the diffusion term in the Navier-Stokes equation. The first is a Legacy scheme that is based on a staircase approximation of the geometry, and the second is a LS-STAG scheme. They give quite similar results, but LS-STAG provides better results for the viscous stress, especially for cells cut by the geometry (Van Der Plas, 2018).

3.12 Temporal integration

3.12.1 Adams-Bashforth method

Adams-Bashforth method is a second-order accurate time discretization method. Equation (3.50) is the second-order Adams-Bashforth equation (Zeltkevic, 1998). h is the time step size, f denotes the derivatives of y at the time t, and y is the solution value. The reader is encouraged to explore the literature from Bashforth and Adams (1883) and Butcher (1999), for further details about the method.

$$y_{n+1} = y_n + \frac{h}{2}(3f(y_n, t_n) - f(y_{n-1}, t_{n-1})) \tag{3.50}$$

3.12.2 CFL-number

The Courant-Friedrichs-Lewy (CFL)-number is used to control that the fluid flow and the wave do not travel more than one cell in the grid for each time step. The number supports the control of the numerical results and regulates the time step. There is no need for a very fine grid if the time step is so large that the waves propagate several cells during one time step. That is a waste of computational power and will give inaccurate results.

Equation (3.51) gives the 3D CFL-number (Van Der Plas, 2018). u, v, and w are the velocities in the corresponding x-, y- and z-direction. ∂t is the time step, and $h_{x,i}$, $h_{y,j}$ and $h_{z,j}$ denote the mesh size in their respective directions. A minimum and a maximum number for the CFL-number are defined both for the flow and the waves.

$$CFL = max_{i,j,k}(\frac{|u_{ijk}|\partial t}{h_{x,i}} + \frac{|v_{ijk}|\partial t}{h_{y,j}} + \frac{|w_{ijk}|\partial t}{h_{z,k}}) \tag{3.51}$$

If the CFL-number exceeds the defined maximum or minimum, the time step is automatically adjusted, to avoid defining unnecessarily small time steps. If the CFL number is lower than the minimum CFL-number value during ten following time steps, the time step is divided once by the factor *dtfact*, a variable defined in $comflow.cfi$. If the CFL-number exceeds the maximum value, the time step is directly multiplied by the *dtfact*.

3.13 Linear solver

A linear solver is utilized to calculate the pressure from the Poisson equation, Equation (3.21). ComFLOW has several solvers implemented, among them are the Successive Over Relaxation (SOR) and the Biconjugate Gradient Stabilized (BiCGSTAB). The SOR solver is limited to one phase simulations, and cannot be used for generating and absorbing boundary condition (GABC). The BiCGSTAB with the Incomplete Lower Upper (ILU) preconditioner is on the other hand compatible with all simulation settings in ComFLOW. The solver is suitable for both OpenMP parallel and MPI parallel. The ILU preconditioner handles the matrix structure near the GABC and takes care of the large difference in the density in the two phase simulations (Van Der Plas, 2018). The BiCGSTAB + ILU is the solver which typically has the best convergence rate. It is the only solver permitting moving bodies without having the risk of slower calculations.

The preconditioner has a drop tolerance implemented. The drop tolerance for pressure, velocity, and GABC is defined by the user.

A stopping criterion is set to ensure stability. A maximum number of iterations is given. Also, the tolerance on the residual is defined. An inner and outer iteration loop is implemented. The inner loop is defined on a two norm of the residual, and the outer iteration loop is based on a maximum norm of the residual. The tolerance of the inner and outer loop in the stopping criteria affects the accuracy of the result.

3.14 Convergence ratio

The convergence ratio can be used to investigate convergence, needing at least three data points. This gives a one term estimation of the convergence rate. If five solution points are used, a two term estimation can be calculated. To find the convergence ratio R_i, Equation (3.52) is used. The difference between the medium and fine solution, $\epsilon_{i,21} = Iq_{i,2} - Iq_{i,1}$, and the medium and coarse solution, $\epsilon_{i,32} = Iq_{i,3} - Iq_{i,2}$, are divided to obtain the convergence ratio. $Iq_{i,j}$ is the numerical result for the corresponding refinement (ITTC, 2017).

$$R_i = \frac{\epsilon_{i,21}}{\epsilon_{i,32}} \tag{3.52}$$

A R_i between zero and one implies a monotonic convergence. If the convergence ratio is negative, a oscillatory convergence is entailed, while a R_i larger than one indicates divergence. For a convergence ratio between zero and one a estimation for the error and the order of accuracy can be done. In cases with oscillatory convergence more than three solutions is required to estimate the error. If the convergence ratio is larger than one the error and order of accuracy cannot be estimated.

3.15 Order of accuracy

If the convergence ratio is between zero and one, the order of accuracy (OA) can be used to quantify the order of convergence. Assuming that the |error|=Δx^{OA} for a quantity q. The order of accuracy can then be defined as in Equation (3.53). Δx is the mesh size and Iq(Δx) is the corresponding numerical value. Iq($\Delta x = 0$) is the exact integral of |q|. With the ratio below, the OA provides information about the convergence of the

numerical solution. A Positive OA indicate convergence, and higher OA gives higher order of convergence (Colicchio, Greco, & Faltinsen, 2007).

$$OA = -\frac{log\frac{|Iq(\Delta x_2)-Iq(\Delta x=0)|}{|Iq(\Delta x_1)-Iq(\Delta x=0)|}}{log\frac{\Delta x_2}{\Delta x_1}} \tag{3.53}$$

The exact solution Iq($\Delta x = 0$) is not known. Assuming a linear relation between Iq and Δx, three mesh sizes and their corresponding numerical value can be used to solve Equation (3.54) to find the exact solution Iq($\Delta x = 0$).

$$-\frac{log\frac{|Iq(\Delta x_2)-Iq(\Delta x=0)|}{|Iq(\Delta x_1)-Iq(\Delta x=0)|}}{log\frac{\Delta x_2}{\Delta x_1}} = -\frac{log\frac{|Iq(\Delta x_3)-Iq(\Delta x=0)|}{|Iq(\Delta x_2)-Iq(\Delta x=0)|}}{log\frac{\Delta x_3}{\Delta x_2}} \tag{3.54}$$

Chapter 4

Methods and results from literature

There exist several papers on the topic of mean and low-frequency wave forces. The papers have different focal points, some papers investigate the effect of current, wind or swell, while others investigate the effect of extreme weather conditions. Some papers look into numerical methods, others present findings from experiments, and some compare numerical and experimental results.

4.1 Experimental methods

In phase I of the EXWAVE JIP, a state of the art model test in scale 1:70 was conducted with the target of determining the slowly varying forces and the slow drift damping in severe sea states. The interaction between waves and current was also a topic for the test. The experiment was carried out at the Ocean Basin Facility at Sintef Ocean during March 2016, focusing on the response of an FPSO subjected to waves and current at fully loaded draught (Fonseca, 2016).

The focus in the EXWAVE JIP was on extreme waves. Tests were carried out for different significant wave heights, peak periods, and current velocities. Regular and irregular waves were tested, and the Torsethaugen wave spectra was used for the irregular waves. A broad banded spectrum, Pink noise, was used to identify the RAO's and phase angles. The experiment was conducted for both collinear and non-collinear wave and current, and the combinations were tested for the three wave headings, 0°, -20°, and -50°, see Figure 4.1 for the definition of the coordinate system.

To obtain the correct draught and radii of gyration, massive weights were used, and to achieve horizontal natural periods above 100 s, see Table 2.1, a horizontal mooring system was utilized. The mooring system had close to linear restoring characteristics and the system was adjustable for different wave headings.

The experiment measured actual wave elevation with wave probes, the vessel motions, accelerations, relative motions, and the forces in the mooring lines. In the post processing, first-, second- and third-order harmonic amplitudes and periods, some statistics, and the RAO's and relative phase angles were calculated.

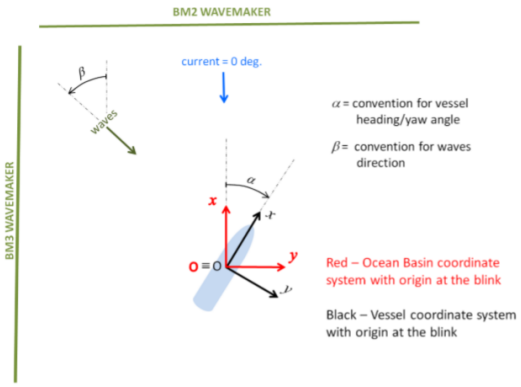

Figure 4.1: The coordinate system in the Ocean Basin for the EXWAVE JIP experiment (Fonseca, 2016).

The results from the experiment indicate that the surge motion increases with increasing current velocity. The interaction between the waves and the current affects the mean offset of the FPSO. The increase of the mean offset may be larger than the steady offset in current alone. This is an indicator that the mean drift increases with current. The mean drift force increases for current in the same direction as the waves but decreases for current in the opposite direction. Surge, sway, and yaw are dominated by the contribution from the low-frequency response. The low-frequency response energy is located around the natural frequency (Fonseca, 2016). It also becomes clear that the heave and pitch damping was underpredicted, which leads to underestimations of the mean drift forces in surge at high periods. The experiment shows that the heave and pitch damping have a viscous drag contribution (Fonseca, Hellan, Stansberg, Nestegård, & Birknes-Berg, 2019).

Another experiment focusing on the topic of drift forces was performed by the Maritime Research Institute Netherlands (MARIN). The experiment focused on the sensitivity of the bow shape of an FPSO on the drift forces and green water loading (Buchner, 1996). Three different bow shapes were tested, a traditional tanker with a small flare in the bow region, a sharp bow without flare, and a bow with significant flare above the waterline, keeping the other main dimensions and the stern unchanged.

The experiment was conducted in both regular and irregular head sea waves. For the regular waves, five different frequencies were tested, while the irregular waves used the JONSWAP wave spectrum with a significant wave height of 13.2 m and a peak period of 12.9 s. A linear spring mooring system made by four springs kept the FPSO in place.

In this experiment, the translation of the vessel was measured with an optical system, the roll and pitch with a gyroscope, and the relative motion of the bow with a wave probe.

The forces between the ship and the mooring system was also measured, in addition, to the mean pressure on a force panel.

The experiment concludes that the sharp bow without flare experience less mean drift and low-frequency forces than the traditional tanker with a small flare. Although larger wave frequency motions were measured for the bow without flare. The observations of non-linearities in the experiment questions the use of linear transfer functions for FPSO's in severe seastates.

4.2 Numerical methods

4.2.1 Potential codes

Drift forces can be estimated from experiments or with several different numerical tools. The motivation for experiments is often to validate the numerical results.

Both the experiments described in Section 4.1 were used to verify numerical results. The EXWAVE JIP concludes that the drift forces are underpredicted by the state of the art potential flow codes for severe sea states where viscous effects are important, especially for semi submersibles. The reason for the underestimation is found to partly originate from Newman's approximation, Section 3.4.1. The JIP states that Newman's approximation can be conservative and non-conservative depending on the peak period of the sea state, and therefore recommends the calculation of full QTF to become common industrial practice. Although the full QTF's also underpredict the drift forces, they can be shown to be more accurate than the Newman approximation (Fonseca, Hellan, et al., 2019). Several other issues are addressed, like the viscous effect on the damping coefficient in heave and pitch, the effect of mooring lines, and higher than second-order effects induced by high steep waves. The latter is to be further investigated in this thesis.

The results from the experiment executed by MARIN are compared with results from a linear diffraction analysis. The paper demonstrates that the calculated RAO and phase coincide well with the experimental results for small wave amplitudes (Buchner, 1996). For high irregular waves, the diffraction analysis overpredicts the pitch motion and the relative motion between the vessel and the waves. The analysis also overpredicts the mean wave drift forces for high periods, but significantly underpredicts the mean drift forces for low periods. The drift forces calculated numerically demonstrates that the mean drift

force in surge is equal for large wave periods for all the geometries, but the traditional tanker has a larger mean drift force in surge than the sharp alternative bows for low periods. The explanation given for this discrepancy is that for short waves the motion of the vessel is low, and the mean drift force, therefore, depends on wave diffraction. The traditional tanker has more volume in the bow compared to the alternative sharp bows, making it more capable of reflecting the waves back into the incoming waves.

The conclusion drawn is that the motion of the vessel, the relative motions, and drift forces are non-linear for wave heights associated with severe sea states for an FPSO. To assure reliable results, this paper recommends performing experiments in both regular and irregular survival waves (Buchner, 1996).

The benchmark study *Wave Forces and Low Frequency Drift Motions in Extreme Seas* by Fonseca, Ommani, et al. (2019) compares four wave-current codes: Muldif by Sintef, HydroStar by Bureau Veritas and Wadam and Wasim by DNV GL. Despite that there has been presented several numerical solutions to the wave-current interaction problem over many years, the implementation and validation is still not finished. Table 4.1 gives an overview of the four software, where Muldif, HydroStar, and Wadam are very similar and Wasim stands out. The benchmark study investigates if the codes are ready for implementation and to be used by the industry.

All the codes solve the problem using the boundary element method in 3D, and they all satisfy the free surface boundary condition to the order of τ. $\tau = \omega U_c/g$ is the dimensionless Brard number. Muldif, HydroStar, and Wadam are frequency domain solvers, while Wasim operates in the time domain. The two former uses a Green function to solve the velocity potential which satisfies the boundary condition. In Wadam, the Green function is Taylor expanded to the first order of τ when τ is assumed to be much smaller than one. Wasim is different from the three others. The velocity satisfies the free surface boundary condition to the order τ^2 and it is based on the Rankine source distribution.

The tools in the benchmark study were tested for a semi-submersible, and excellent agreement between the numerical tools became evident. Even the case with a current of $0.82\ m/s$ gave very similar results. The results even coincide with the results from Wasim that do not assume a small τ. The study concluded that the software gives consistent results for the semi-submersible in head sea waves with collinear wave and current.

Table 4.1: Characteristics for Muldif, HydroStar, Wadam and Wasim (Fonseca, Ommani, et al., 2019)

	Muldif	HydroStar	Wadam	Wasim
Green function	Free surface	Free surface	Free surface	Rankine
Solver	Frequency domain	Frequency domain	Frequency domain	Time domain
B.E.M.	3D	3D	3D	3D
User	Sintef Ocean	Bureau Veritas	DNV GL	DNV GL
Wave-current	O(τ)	O (τ)	O(τ)	Full

Today's common practice is to use programs such as Muldif, HydroStar, Wadam, and Wasim, which are based on linear potential theory and do not in general include nonlinear phenomena in severe sea states. Features such as wave-current interactions are being implemented to improve the programs.

Hanssen et al. (2013) studied the *Aspect of the Mean Surge Drift Force for Single-Point Moored Vessel*. The paper investigates the effect of the bow shape and the linear heave and pitch motions on the surge drift force. The potential theory code Wadam was used for the calculations, where the bow shape, pitch radius of gyration, and water depth was varied. The three different bow shapes analyzed are presented in Figure 4.2. Rather than having the same main dimensions on the FPSO's, the displacement, longitudinal center of buoyancy, heave, and pitch restoring coefficients and the natural periods are strived to be kept equal. The lengths are between 300 and 316 m, the draft is 12 m and the widths are between 50 and 60 m. The paper concludes that the mean drift force in surge is highly sensitive to the bow shape, see Figure 4.3a. For head sea waves, *Bow variation 1* gave the lowest mean drift force in surge. Nevertheless, if the incoming waves had an angle of $\pm 30°$, the bow caused a high sway drift force, concluding that selecting a bow based on the minimum second-order forces is not a trivial task.

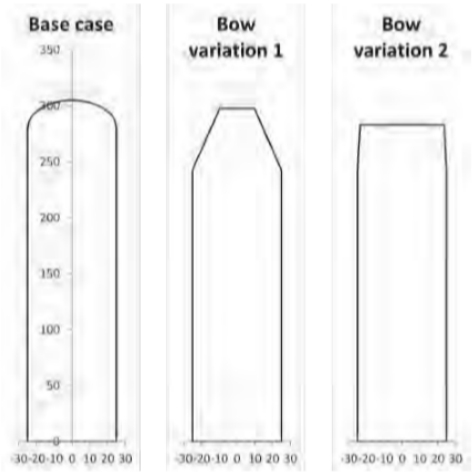

Figure 4.2: The water lines of the FPSO hulls (Hanssen et al., 2013).

The mean drift force in surge was calculated for the water depths 1000 m, 100 m, and

50 m for the *Base case*. The analysis showed, Figure 4.3b, that for periods below 14 s, both the motions and drift forces were almost identical for all the water depths. Even for periods above 14 s the difference between the results for 1000 m and 100 m was marginal. While the water depth of 50 m, gave the significant lower pitch and heave motions, and a higher mean drift force in surge. It was also demonstrated that a higher pitch radius gives larger pitch motions for the *Base case*. The result is presented in Figure 4.3c. As a consequence of larger motions, higher mean drift forces in surge are calculated, because of increased relative motion between the vessel and the waves.

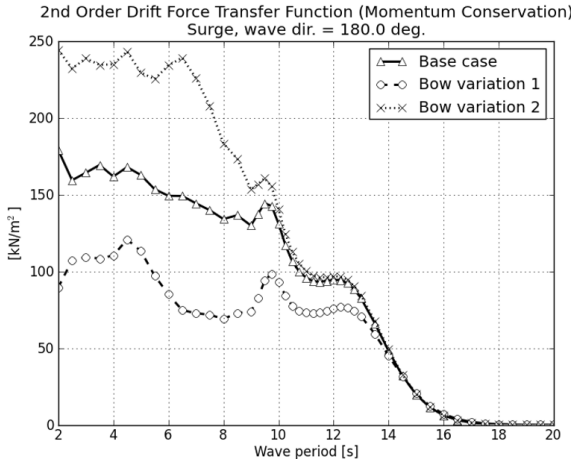

(a) Mean drift force in surge for three different bows.

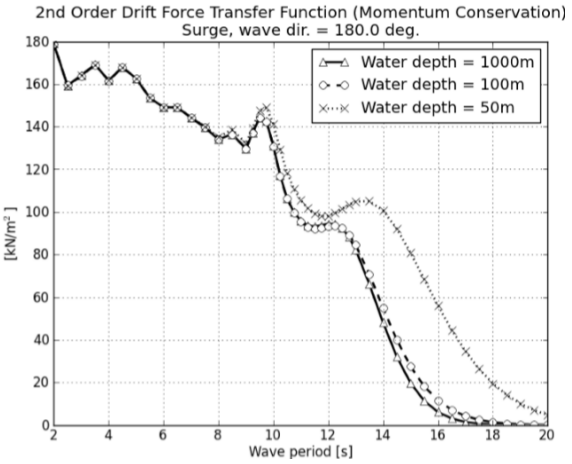

(b) Mean drift force in surge for three different water depths.

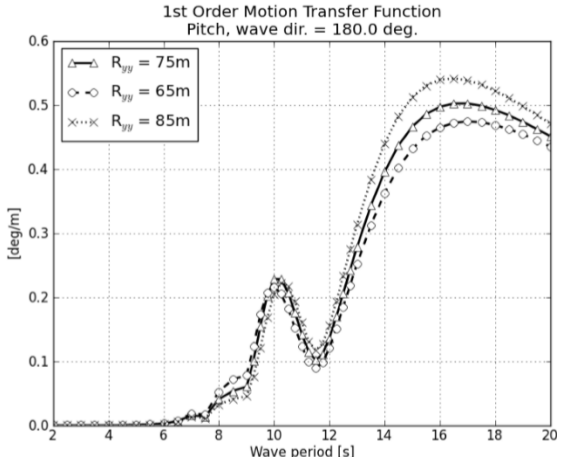

(c) The linear pitch motion for three different radius of gyration.

Figure 4.3: Results from *Aspect of the Mean Surge Drift Force for Single-Point Moored Vessel* (Hanssen, Bruschi, & Pettersen, 2013).

4.2.2 Nonlinear codes

To be able to investigate nonlinear problems numerically, CFD codes can be used. There exist several CFD-codes for example openFOAM, Star CCM+, Fluent, and ComFLOW.

A CFD analysis of a semi-submersible was conducted by Bøckmann (2016) using Star CCM+. The purpose of the analysis was to investigate how drift forces can be estimated using CFD. Another object was to further enhance the understanding of the physics behind the drift forces.

Regular waves with different wave heights, current, and investigation of viscous effects and turbulence were considered. The numerical results were compared against experimental results. Because of symmetry, only half the geometry of the semi-submersible was modeled, see Figure 4.4. Five different cases with regular or colinear regular waves and current and one case with current alone was looked into.

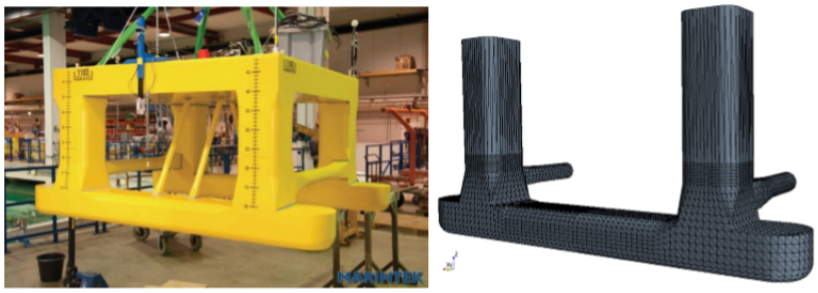

Figure 4.4: [Left] Model used in the experiment by MARINTEK [Right] The numerical model, not with the final mesh (Bøckmann, 2016).

Comparing the measured waves from the experiment with the imposed fifth-order Stokes waves from the CFD, reveals some deviations for the cases with the steeper waves. To correct for the discrepancy, the wave height was tuned to match the results from the experiment. The semi-submersible and the domain were modeled in Star CCM+ utilizing the Euler Overlay Method to minimize the domain size by removing reflections (Bøckmann, 2016). Simplifications of the problem were implemented in the CFD analysis, among them were higher mooring tension, no rotational mooring stiffness, symmetry conditions resulting in no sway motion and correlated vortex shedding and the diagonal braces were excluded.

The paper concludes that in 3 out of 5 cases the mean drift forces deviated less than 5% from the experimental results. Nevertheless, the comparison reveals some differences

between the numerical and experimental results, and for some of the discrepancies, the reasons are unclear. The convergence test conducted demonstrated sufficient resolution.

Another article focusing on the drift forces calculated with a CFD code is the paper titled *Estimation of the drift forces and added resistance in waves of the KVLCC2 tanker* by Fournarakis, Papanikolaou, and Liu (2017). The research paper examines different numerical techniques for estimating drift forces, yaw moment, and added resistance of a ship. The numerical results were compared against experimental results. The aim of the study was to validate and complement the results for the mean drift forces calculated with potential theory.

The numerical tools used in the analysis were a potential theory in-house 3D panel code called NEWDRIFT, and an unsteady Reynolds averaging Navier-Stokes (URANS) CFD solver Star CCM+. The numerical results were compared against experimental results from the SHOPERA project (Fournarakis et al., 2017).

The KVLCC2 stands for **K**orean Institute of Ship and Ocean Engineering (**K**RISO) **V**ery **L**arge **C**rude **C**arrier. It is a has typically a voluminous ship with a bulb and a U-shaped stern.

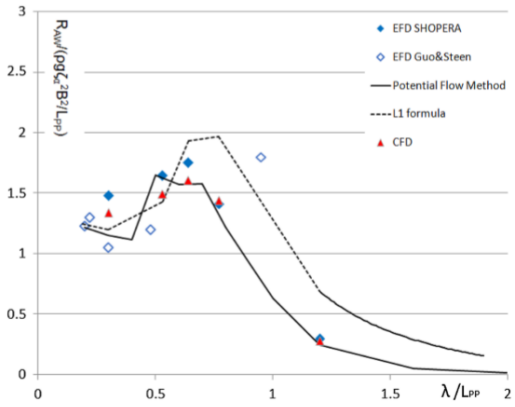

Figure 4.5: Mean drift force in surge for the KVLCC2 ship at zero speed in head sea waves (Fournarakis, Papanikolaou, & Liu, 2017).

The paper concludes that the results for the mean drift forces in surge are satisfactory for practical applications. Nonetheless, as can be seen from Figure 4.5, the largest deviations between the linear results and the results from the CFD calculations for the mean drift force in surge, are located at the short and hence steep waves.

Chapter 5

Software

The following chapter is a description of the software utilized in this thesis for the calculation of the mean drift forces. The geometries are based on the FPSO's described in Chapter 2. The Sesam software, from DNV GL, is a package of state of the art tools widely used in the industry for solving different hydrodynamic and structural problems and was therefore chosen as the linear potential solver. An overview of all the software is demonstrated in Figure 5.1. GeniE and HydroD are categorized as main tools and were used to model and mesh the geometries and to interactively execute Wadam. Wadam was utilized to calculate the drift forces and body motion in the frequency domain. Postresp was used to post process the data together with MATLAB.

The nonlinear problem was solved with ComFLOW, a CFD solver. The geometry was extracted from HydroD and meshed in Star CCM+, before it was converted to a suitable geometry file for ComFLOW. The results were post processed using ParaView and MATLAB.

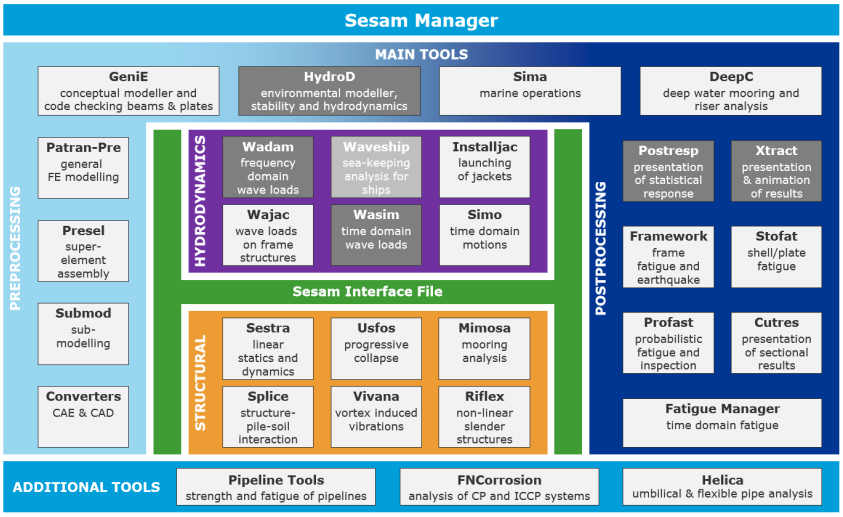

Figure 5.1: Overview of the DNV GL software (DNV GL, 2019c).

5.1 GeniE

GeniE is a structural design analyzing tool. The software enables the user to model the desired geometry, but can also work as a complete analysis tool permitting modeling, calculations, post processing results and checking the results against standards (DNV GL, 2018). A JS-file containing the geometry of a typical tanker scaled to a Brazilian sized FPSO was provided by Equinor. With the shape of the provided FPSO as a starting point, other geometries were made by moving points in the original JS-file. The shapes were inspired by the FPSO's Norne, Brasil, and Adolo illustrated in Chapter 2. Making one with a bulb, one without a bulb, but with a flare, and the third one with a wall sided bow without a bulb nor flare, see Figure 5.2. More figures of the geometries are enclosed in Appendix A.

The command file starts with stating all the points defining the geometry. Then the curves between the points are given before the hull and curved patches are constructed. The normal vectors are defined out into the fluid, as in Figure 3.1. For some of the patches, the normal vectors need to be flipped to point into the fluid. When all the points, curves, and patches are defined correctly the panel model is assembled, and then meshed. The JS-file provided also contained the command for meshing the geometry. Specifying the length of a grid cell, GeniE aims at making square elements with the defined length. The file also included a command for exporting the meshed geometry as a *FEM*-file to be able to import the geometry to HydroD. Since the FPSO is x-z-symmetric, only half the ship needs to be modeled. This makes the model simpler to handle, saves computational power, disk space, and time.

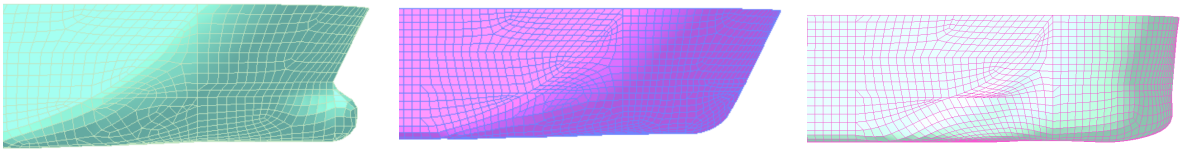

(a) FPSO with bulb. **(b)** FPSO without bulb. **(c)** FPSO with wall sided bow.

Figure 5.2: The three meshed geometries from GeniE illustrated in HydroD.

5.2 HydroD

HydroD is one of the main tools in the Sesam package, Figure 5.1. It is an interactive software that utilizes Wadam, frequency domain, or Wasim, time domain, to calculate wave loads and motions. In HydroD the geometry from GeniE is imported and the mass model is specified. In Table 5.1 the main particulars for the FPSO are specified. HydroD uses two different coordinate systems: the input coordinate system and the global coordinate system. The global coordinate system is used when defining a loading condition where the trim, heels, and change in draft needs to be specified, and it is located at the still water line at z=0. Wadam gives the hydrodynamic loads in the global coordinate system. All the input data and models are given in the local coordinate system. Results from Wadam that refer to coordinates at the body, like the center of gravity and the center of buoyancy, are given in the local coordinate system (DNV GL, 2017). The global coordinate system is located at the free surface midships in HydroD, while in GeniE, the coordinate system is located at the keel. This makes it necessary to translate the model to correspond with the global coordinate system defined in HydroD.

Table 5.1: Main particulars of the FPSO.

Lpp	320	$[m]$
Breadth	58	$[m]$
Draught	20.8	$[m]$
Mass	336952	$[ton]$
Vertical COG	-2.94	$[m]$
Longitudinal COG	2.87719	$[m]$
Roll radius of gyration	18.6	$[m]$
Pitch radius of gyration	73.5	$[m]$
Yaw radius of gyration	74.5	$[m]$

The periods for the analysis were chosen to be between 3 s and 40 s, with a time step of 0.5 between 3 s and 24 s, and the values 25, 27, 30, 35, and 40 were added to complete the tail. These periods are the same as the ones for the analysis provided, to make the results as comparable as possible. Damping of the roll motion was specified to be 5% of the critical damping.

After all the necessary parameters of the model and the environment are defined in

HydroD, the calculations can be conducted by starting Wadam from HydroD. When Wadam successfully finishes the calculations, Postresp can be initiated from HydroD to post process the results.

5.3 Wadam

Wadam executes hydrodynamic calculation of wave structure interaction for freely floating or fixed structures of all types. The program uses linear potential wave theory, and represent the state of the art technology for solving wave-structure interactions (DNV GL, 2019b). Since Wadam uses first and second order potential theory, the problem is only calculated up to the still water level at z=0. The program can be used to calculate hydrostatic data, inertia properties, global response both for single and multi-body systems including other features. The analysis is performed in the frequency domain and uses the Morison's equation for slender structures and first and second-order three dimensional potential wave theory to solve the large volume structure problems. The theories can also be combined for structures consisting of both slender elements and large volumes. The results are presented as complex transfer functions.

The different model types in Wadam are hydro model, mass model, and structural model. The hydro model is used for calculating the hydrodynamic forces, including the panel model, the Morison model, and the composite model. The mass model is suitable for floating structures were the structure could be defined as a finite element model with mass properties or a global mass matrix. The structural model represents the hydrodynamic and static loads as finite element loads. In this thesis, a panel model was used to calculate the hydrodynamic loads, including mean wave drift forces.

Like all numerical programs, Wadam has its limitations. There are drawbacks considering both the geometry and the analysis. The limits considering the geometry are the maximum number of panels, nodes, elements, etc. The analysis has restrictions for the maximum number of wave frequencies, headings, currents profiles among others. Relevant limits for this thesis are the maximum number of panels in the geometry and the maximum number of wave frequencies in the second-order analysis. With the current version of Wadam up to 50 000 panels are permitted, and 60 wave frequencies in the second order analysis.

To calculate the second-order mean drift forces in Wadam, one can choose between the

method of conservation of fluid momentum in surge, sway and yaw, tagged *Hdrift*, or the direct pressure integration method in all six degrees of freedom, called *Drift*. The forces are based on linear surface waves interacting with the body. Hence, the problem is simplified according to the potential wave theory explained in Section 3.1. It is worth noting that direct pressure integration is a tedious operation. According to the HydroD user manual (DNV GL, 2017) the calculation of the drift forces using the direct pressure integration method may double the calculation time.

In Wadam the axis is defined according to the right hand definition where z is positive upward. The incident waves are given by the angle β defined counter-clockwise from the x-axis. The FPSO was modeled with the bow pointing in the positive x-direction. This means that to analyze head sea waves, the direction of the incident waves needed to be 180°. The coordinate system was located at the free surface at the zero crossing midship.

5.4 Postresp

Postresp is a software for post processing the results calculated by Wadam. The program can process and display the response variables, wave spectra, wave statistics, long and short term variables and statistics, workability analysis, and stochastic fatigue calculations among other features (DNV GL, 2019c). In this thesis, it is only of interest to look into the transfer functions for the motions, added mass, damping, excitation forces, and the drift forces. The transfer functions are denoted *Response variable* in Postresp. Since the interface in Postresp is a bit outdated, the data was exported to MATLAB via CSV-files. This also enabled post processing and plotting of the results across the geometries which were analyzed separately in HydroD.

5.5 ComFLOW

ComFLOW is a validated CFD tool for the marine and offshore industry to solve free-surface problems. ComFLOW solves the Navier-Stokes equation for one or two phases of fluids. The program was developed by the University of Groningen, and is further developed in close cooperation with MARIN (Van Der Plas, 2018). The program was initially developed to study sloshing of liquid fuel in spacecraft but was extended, and further developed to handle anti-roll tanks and water on deck. Latest, impact loading due to steep waves, green water loading and the motion of freely floating bodies has been

implemented. As of today, the program is developing continuously.

The geometry is defined by the preprocessor GEODEF and the fluid solver is ComFLOW. The results from ComFLOW were visualized in ParaView and MATLAB.

5.5.1 *GEODEF*

The preprocessor GEODEF defines the geometry, the computational domain, and grid, and sets up the folders and documents required to run the analysis with ComFLOW. It uses finite element modeling, enabling the definition of complex geometries (Van Der Plas, 2018).

GEODEF makes the file that contains the information about the volume and edge apertures, based on the *geometry.in* file. To make the process of defining the geometry efficiently, the volume and edge apertures are defined first in the process. Then the cells are checked if they are neighboring cells of a solid geometry. If a cell is not close to a geometry, all the integration points are set to zero, indicating that they are open for fluid flow. This approach saves computational power by not checking if every integration point is inside a geometry since every cell can contain several integration points, see Figure 3.4. After running GEODEF, the apertures can be visualized in ParaView.

geometry.in

To enable the use of the same geometry as modeled in GeniE, the geometry was converted into an *in*-file that is compatible with ComFLOW. The strategy to convert the file consisted of extracting a *gdf*-file from HydroD, converting it to an *stl* format using a Python script, then changing it to a *vtk*-file with Star CCM+, before it was finally transformed to an *in*-file with a MATLAB script.

To get the *gdf*-file from HydroD, the temporal Wamit files had to be saved. Since the output from Wamit and Wadam calculations only are given up to the free surface, the geometry was chosen to be fixed, and the waterline was moved to the top of the model. This permitted the whole model to be exported.

The meshing of the geometry was done using Star CCM+. A target value of 20 m, with a number of points per circle of 12 and a minimum size of 0.25 m was chosen for the coarse mesh. A refinement ratio of $\sqrt{2}$ was used to make a medium, fine, and extra fine mesh. This is the recommended refinement factor given by the ITTC (2017) for a convergence

study.

5.5.2 *ComFLOW*

ComFLOW requires two input files to calculate the forces on a structure. The program needs one file defining the geometry, and one specifying the run. The geometry is defined by the preprocessor, *GEODEF*, from the *geometry.in*-file, and given as an input for *ComFLOW* as a file called *aperture.in*. Other optional input files defining external forces, prescribed movements of a geometry, or irregular sea states, among others, can also be given.

comflow.cfi

comflow.cfi contains all the settings for the analysis. The following section presents an overview of the input settings and the parameters used in the analysis completed in this thesis. The one-phase solver was used for the calculations, since there were no slamming or breaking waves present.

Domain

The domain was specified by giving the maximum and minimum values in x-, y- and z-direction. Symmetry was specified to reduce the computational domain. The domain sizes used in the convergence test are presented in Table 8.2, and the very large domain was used for further calculations.

Geometry

The geometry was imported, and the *Exact method* for calculating the volume and edge apertures was stated, see Section 3.7.2 for an overview of the method. The number of integration points were set to 64.

Waves

The analysis can start with still water or directly with waves, as the initial condition for the fluid in the domain. The Stokes 5th order waves were used to model the waves, as presented in Section 3.10.2. Wave height, period, angle of the incident waves, and location of the crest were defined. See Table 8.1 for the overview of the periods and the wave heights used in the analysis. No current was present during these calculations.

Time

The length of the simulation was defined as the maximum time. The initial time step was set to 0.01 s for the first cycle of calculation. The time step was controlled against the diffusive restriction for the time step and was automatically adjusted. The minimum time step was set to 0.0 s, while the maximum time step was set to 1.0 s. After the first cycle, the time step is controlled against the CFL-number for the flow, and the wave, see Section 3.12.2 for the definition of the CFL-number. The minimum CFL-number for the flow was set to 0.25, and the maximum to 0.95. The CFL-number for the wave was given the minimum value of 0.0, and the maximum value 1.0. If the CFL-number is larger than the maximum numbers defined, the time step is multiplied by *dtfact* which is defined equal to 0.5. On the other hand, if the CFL-number is smaller than the minimum CFL-numbers ten successive times, the time step is divided on *dtfact*.

For time integration, the Adam-Bashforth method was used, see Section 3.12.1 for further details.

In ComFLOW Equation (3.50) is implemented as presented in Equation (5.1), with the following two conditions satisfied. The parameters in Table 5.2 are given as a common combination for the user.

$$\begin{aligned} ddtd\, u^{n+1} &= ddta\, u^{n} + ddtb\, u^{n-1} + f(feab1\, u^{n} + feab2\, u^{n-1}) + ... \\ 1 &= feab1 + feab2 \\ 0 &= ddtd - ddta - ddtb \end{aligned} \tag{5.1}$$

Table 5.2: Common combination of parameters for the second order Adam-Bashforth discretization scheme (Van Der Plas, 2018).

ddtd	ddta	ddtb	feab1	feab2
1.0	1.0	0.0	1.5	-0.5

Boundary condition

A Generating and Absorbing Boundary Condition (GABC) was defined at the inflow and the outflow of the domain. The boundary condition builds on the theory in Section 3.6.2. The GABC only works for one phase simulations and is not applicable for domain walls perpendicular to the wave direction. Hence, it would not have any effect implementing it on the sides of the domain. A simple solution to avoid reflections from the wall was to make the domain wider. To decide the variables a_0, a_1, and b_1 in Equation (3.36), a MATLAB script was provided by ComFLOW. The script optimizes the coefficients for a given range of kh and calculates the maximum reflection error made within the range of kh. Figure 5.3 shows the exact and approximated solution of the dispersion relation for the periods from 5 s to 40 s with a water depth of 400 m. As this thesis only focuses on regular waves, the dispersion relation, and hence the GABC, can be described exactly, since only one wave period is present in the sea state.

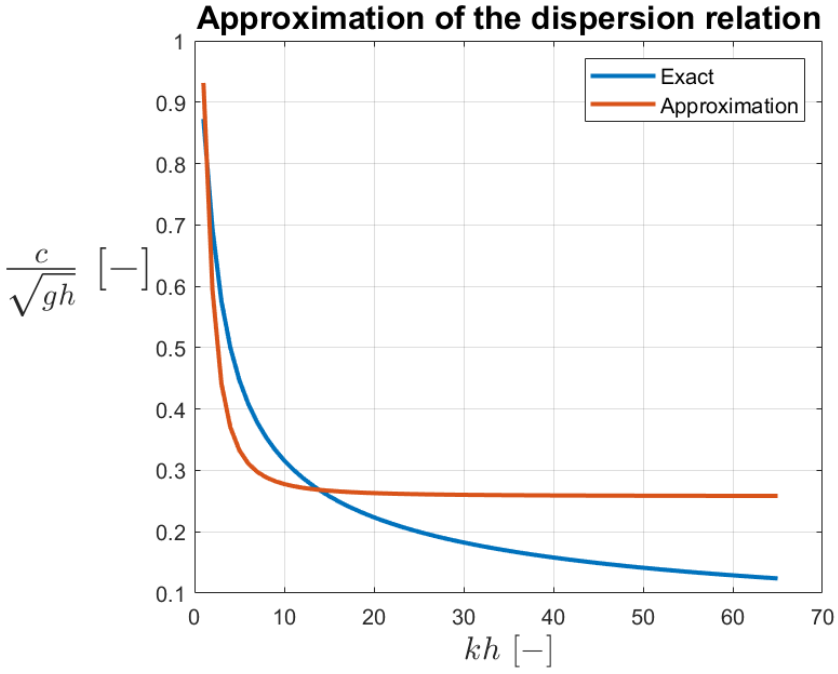

Figure 5.3: The exact dispersion relation and the approximated dispersion relation with optimized variables a_0, a_1 and b_0.

No wall model was used, and since the FPSO has quite a round shape both for the bulb and the stern, which will cut the cells, the LS-STAG scheme was the best choice for the diffusive term. This is also the recommended discretization scheme for diffusion (Van Der Plas, 2018).

Physical parameters

The physical parameters for water density, 1025 kg/m^3, and water viscosity of 0.001 $N \cdot s/m^2$, were defined in the *comflow.cfi*. The acceleration of gravitation was also given as 9.81 m/s^2 in the negative z-direction.

Grid

The grid was defined by giving the number of elements in each direction for the base level of the grid. The refinement rate was set to 2 in every direction, and no stretching was used. Sub grids are defined giving coordinates within the finest level defined. The properties and set up of the grid are more comprehensively described in Section 3.7.1, and the final set up is presented in Table 5.3.

Table 5.3: Set up of sub grid.

Coordinates $[m]$ / Sub grid levels	X_{min}	X_{max}	Y_{min}	Y_{max}	Z_{min}	Z_{max}
1	-∞	∞	-∞	∞	-∞	∞
2	-∞	∞	-200	∞	-60	∞
2	Outlet-40	∞	-∞	∞	-∞	∞
3	-200	200	-150	∞	-40	∞
3	Outlet-20	∞	-∞	∞	-∞	∞
4	-190	190	-80	∞	-30	∞
5	-185	185	-75	∞	-25	10

The sub grid levels indicate a refined grid within the area defined. The second line for the sub grid levels 2 and 3 in Table 5.3, defines a finer grid close to the outlet. The reason is that if the grid became too coarse close to the outlet, the water level dropped. The drop was avoided by introducing the refinement at the outlet. See Figure 5.4 for the sub grids and the refinement at the outlet.

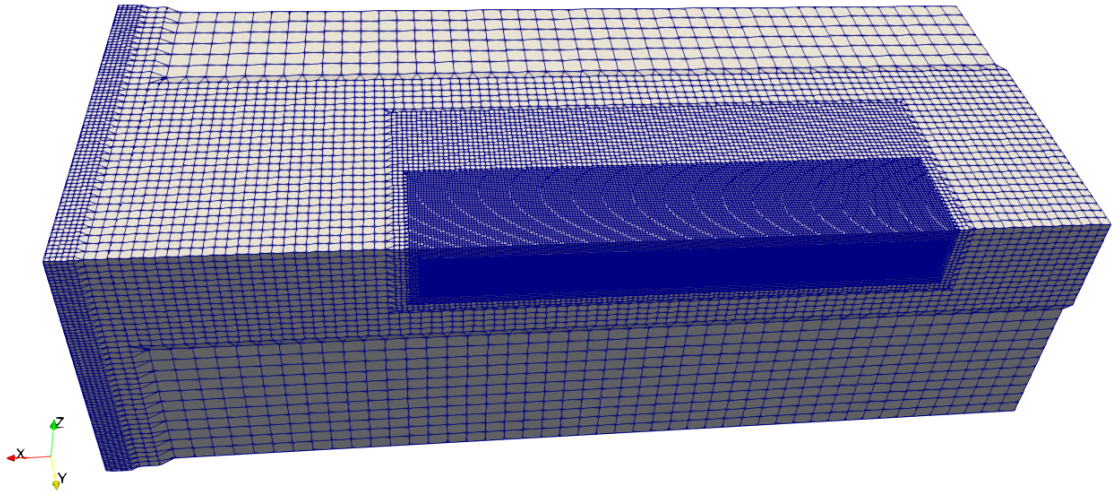

(a) Sub grids for the medium domain.

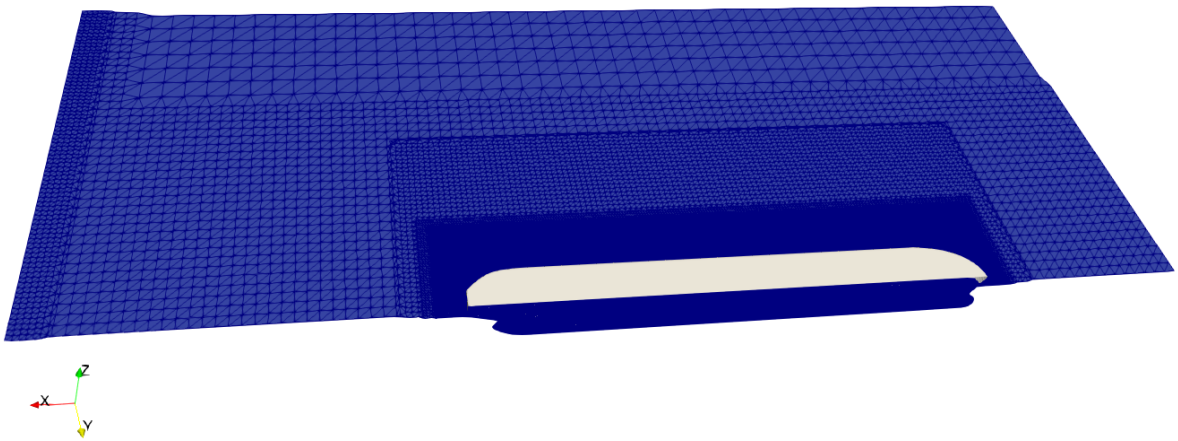

(b) Sub grids at the free surface.

Figure 5.4: Grid refinement for the medium domain in ComFLOW.

Linear solver

BiCGSTAB-ILU was used as the solver for the calculations. That is because, as described in Section 3.13, this solver is compatible with all of the settings in ComFLOW. The documentation manual gives some recommended settings for the BiCGSTAB-ILU. A default value for the general drop tolerance was given, and it was combined with a stricter drop tolerance for the GABC-related equations. The drop tolerance for the pressure was equal to 10^{-3}, the wave drop tolerance was 10^{-2}, and the drop tolerance for the GABC was equal to 10^{-6} (Van Der Plas, 2018).

To control the calculations a stopping criterion for the pressure, velocity, and the maximum number of iterations must be defined. As explained in Section 3.13 an inner and outer criteria were specified. The inner and outer pressure stopping criteria were set to 10^{-6}, while the inner and outer velocity stopping criteria were given the value -1. The maximum number of iterations was set to 10 000.

Volume of fluid method

The VOF method was used to construct the free surface by the use of the PLIC. The normal vector of the surface was calculated utilizing the central method. The advection was discretized with a MACHO scheme, and a basic correction, the LHF, was implemented. The features are described more in detail in Section 3.8.

Output settings

Relative water height line is a setting defining a line, where the total water height is calculated by PLIC. The line works as a wave probe and gives the water height for each time step. Lines were defined at different locations in the xy-plane with coordinates from -10 m to 10 m in the z-direction.

A *Force box* can be used to calculate the forces and moments on a geometry. It uses the direct pressure integration method explained in Section 3.2. A force box can be defined on any part of a structure or the structure as a whole. A *Force box* was defined with a good margin around the geometry, and gave the total integrated forces and moments in x-, y- and z-direction.

movingobject.in

The *movingobject.in* is a file containing the properties of the FPSO as presented in Table 5.1. The mass and inertia properties are required, while the spring and damping properties are elective. The motion was set to interactive in heave and pitch, and locked in the other degrees of freedoms, meaning that ComFLOW calculates the motions simultaneously to solving the Navier-Stokes equation. The motions are defined as given in Section 3.9.

5.6 ParaView

ParaView was used to visualize the simulations from ComFLOW. It is an open-source, multi-platform scientific data analysis and visualization tool (Avila, Osterdahl, McKenzie, & Jordan, 2020). The program is suitable for a wide range of data sets depending on the hardware the application is applied to, ranging from machines with only one processor to high performance computers (HPC). It is based on the Visualization Toolkit (VTK), which converts data into images for a better overview and interpretation of the results.

VTK-files are generated by ComFLOW and can be visualized in ParaView. The program has a broad selection of filters and settings enabling the user to extract or further investigate the data. The mesh, velocity, and pressure, among other things, can be simulated.

Chapter 6

Computational setup and resources

A personal computer with a Microsoft Windows operating system was used for running ComFLOW. Since the provided version of ComFLOW needs a Linux operating system a virtual machine was installed. Besides, access to additional computational power was granted to enable larger simulations.

6.1 Oracle VM VirtualBox

Oracle VM VirtualBox Manager with Linux operating system was installed on the personal computer to enable analysis with ComFLOW. The operating system can be launched from the Oracle VM VirtualBox Manager app, and the system can run simultaneously with the Windows operating system (Oracle Corporation, 2020). Results were extracted using a shared folder between the operating systems. 200 GB of disk memory was allocated to the virtual machine.

6.2 Extra computational power

To be able to run longer and more extensive simulations within an acceptable time frame, additional computational power was needed. The supercomputer Saga, NTNU's cluster Idun, and DNV GL's cluster Tyr were used for the CFD simulations.

6.2.1 Supercomputer - Saga

Saga is a national supercomputer placed at NTNU in Trondheim and managed by the National Infrastructure for HPC and Data Storage in Norway. The supercomputer has been operative since mid-2019 and has a life expectancy of four years. The supercomputer has a computational capacity of around 85 million CPU hours a year. Table 6.1 gives

an overview of the main components and key figures for Saga, (Sigma2, 2020). The supercomputer was used by the Norwegian government to COVID-19 related research, causing queue and days with waiting for results.

Table 6.1: Technical details of Saga.

Main components		
200 Standard computer nodes	40 cores	192 GB memory
28 medium memory compute nodes	40 cores	384 GB memory
8 big memory nodes	64 cores	3 TB
Key figures		
Processor Core	10080	
GPU units	32	
Internal Memory	75 TB	
Internal disk	91 TB NVMe	
Central disk	1 PB	
Theoretical Performance	645 TFLOPS	

6.2.2 Cluster - Idun

The Idun cluster is a joint founding between several of the faculties at NTNU. The cluster has more than 70 nodes and 90 GPGPUs. Every node possesses at least 128 GB of memory and holds two Intel Xeon cores. The node is connected to an InfiniBan network (Själander, Jahre, Tufte, & Reissmann, 2019). A variety of software is applicable. The cluster was available through a virtual private network (VPN) during the period the university was closed.

6.2.3 Cluster - Tyr

Access was disposed to Tyr, a DNV GL cluster. The cluster is owned, used, and managed by DNV GL. The cluster has 16 CPUs per blade, and every node has 128 GB.

6.3 Terminal and Vim

The terminal in the virtual machine was used for launching ComFLOW, to access the supercomputer Saga and the cluster Idun, while power shell was used to access and run

the analysis on Tyr. ComFLOW requires the set up of a folder named *input_folders*, containing the ComFLOW setup-file, *comflow.cfi*, the file defining the geometry, *geometry.in*, and any other additional files such as a file with external forces. The preprocessor GEODEF is executed by writing *geodef* as a command in the terminal, within the folder containing the input folder. Following, the command *comflow* is used to carry out the calculations with ComFLOW. A batch file can also be used to run ComFLOW. Then the direction to the location of the folder is specified, and the commands *geodef* and *comflow* are stated.

For general text editing, Vim has been used. Vim stands for **V**i **IM**proved and was written by Bram Moolenaar and released in November 1991 (Schulz, 2007), and is still one of the most used text editors. The editor supports syntax highlighting for a wide range of programming language and is rich in additional features like supporting Python and the possibility for the user to write their proper scripts for Vim, enabling further costume made the expansion of the editor.

Chapter 7

Results from Wadam

This Chapter presents the convergence test conducted for the geometry and the motion and forces calculated with Wadam.

7.1 Testing for convergence

For a numerical method, the results may be sensitive to the discretization of the body. It is important to check for numerical convergence to assure numerically stable results. The geometry with bulb, see Figure 5.2a, was used for the convergence test in both Wadam and ComFLOW. The largest mesh size found to be acceptable in the convergence study was also used for the geometry without bulb and the wall sided geometry. Since the shape of the bow is the only difference between the geometries, the other cases were assumed to converge for the same criteria. Nevertheless, there could be important individual differences caused by the shape of the bows causing this assumption to be inaccurate. The convergence ratio, presented in Section 3.14, indicates convergence and the order of accuracy, explained in Section 3.15, quantifies the convergence.

For calculation assuming potential theory, and using Wadam, the geometry was meshed in GeniE with elements with lengths from 1 to 10 m, with a step of 1 m. In Wadam, a good convergence test is to check if the conservation of fluid momentum method and the method of direct pressure integration provides the same results (Nestegård & Fonseca, 2017). Figure 7.1 shows the relative difference between the two methods. *Drift* is the notation for the direct pressure integration method, and *Hdrift* is the notation for the method of conservation of fluid momentum, as named in Postresp. To make the difference between the two theories dimensionless, Equation (7.1) was utilized. This equation takes the difference between the two methods and divides it by the mean value, then it sums the contributions for the frequencies from 3 s to 14.5 s. This is the region where the

discrepancy between the methods was observed to be most significant, see Figure 7.9a and Figure 7.8a. For periods higher than 15 s the drift forces goes quickly towards zero, causing the contribution from the relative difference to become very large. Periods over 15 s was therefore not representative. The mesh size is the length of the elements of the geometry and is given in $meter$. If not otherwise specified, the forces are given in $Newton$ and the wave amplitude in $meter$.

$$\sum_{3s}^{Periods=14.5s} \frac{|Hdrift| - |Drift|}{(|Hdrift| + |Drift|) \cdot \frac{1}{2}} \tag{7.1}$$

In Figure 7.1 the relative difference and hence the solution, stabilizes from a mesh size with length 3 m, corresponding to around 4500 panels.

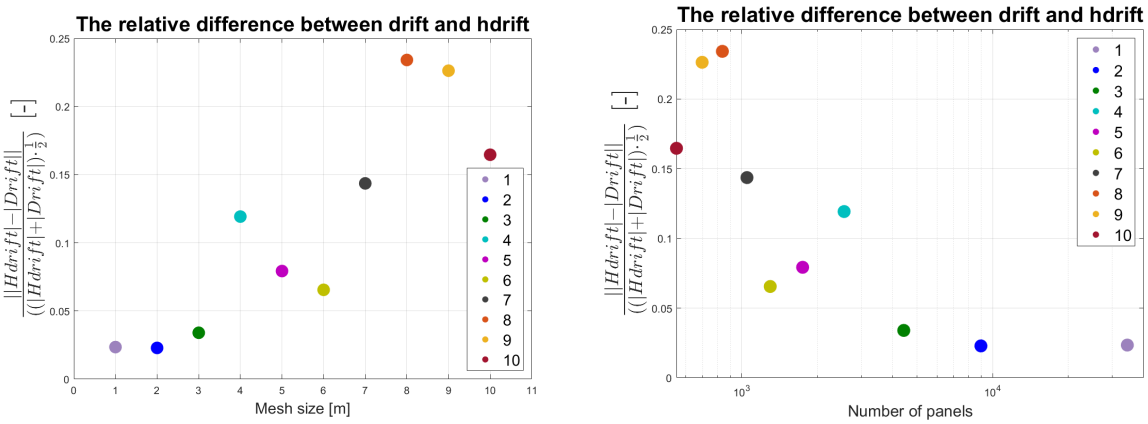

(a) Linear axis.

(b) Logarithmic x-axis.

Figure 7.1: Relative difference between *Drift* and *Hdrift* for different mesh sizes.

Equation (7.1) sums over the periods from 3 s to 14.5 s without differentiating the gap between the methods as a function of the period. The relative difference is therefore further investigated for convergence for the periods of 4 and 11 s, see Figure 7.2 and Figure 7.3. The period of 4 s was selected because it is in the area where the difference between the methods is large, and 11 s was chosen since it is in the area of the peak period for the drift force in surge.

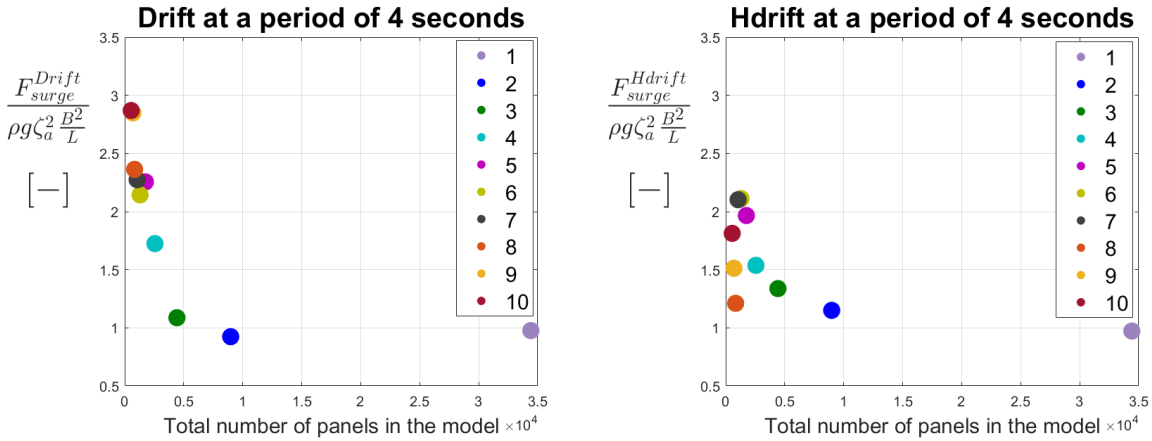

(a) *Drift* at T = 4 *s*. **(b)** *Hdrift* at T = 4 *s*.

Figure 7.2: *Drift* and *Hdrift* at T = 4 *s*.

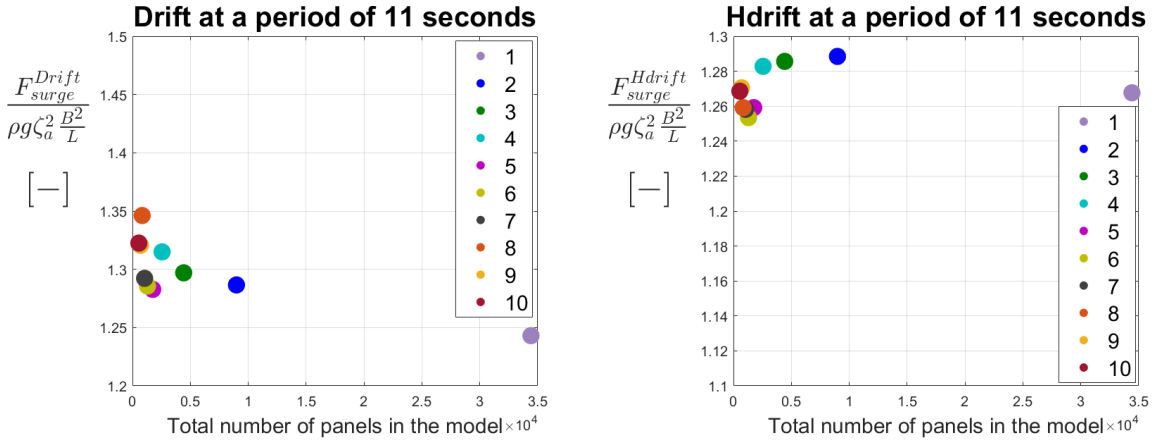

(a) *Drift* at T = 11 *s*. **(b)** *Hdrift* at T = 11 *s*.

Figure 7.3: *Drift* and *Hdrift* at T = 11 *s*.

The three finest mesh sizes for *Drift* and *Hdrift* were used to check for convergence with the convergence ratio and the order of accuracy. Table 7.1 gives the order of accuracy (OA), standard deviation (Std), variance (Var), and convergence ratio (R) for *Drift* and *Hdrift* at the periods 4 *s* and 11 *s*. The standard deviation is a measure of the spreading of the data points, and it is the square root of the variance. As can be seen from Table 7.1 the spreading of the data is less when the method of conservation of fluid momentum is used.

According to the convergence ratio in Table 7.1 only the *Hdrift* at 4 *s* converges. The *Drift* at 4 *s* and *Hdrift* at 11 *s* has oscillatory convergence, and *Drift* at 11 *s* is diverging.

It therefore only make sense calculating the OA for *Hdrift* at 4 s. The OA are calculated for all the cases, but marked in gray for the cases where the convergence ratio does not indicate convergence.

Table 7.1: Statistic for the convergence and spreading of the data for *Drift* and *Hdrift* for the period 4 and 11 s. Gray cells indicates OA of no interest because R does not indicate monotonically convergence.

	T = 4 s				T = 11 s			
	Std	Var	R	OA	Std	Var	R	OA
Drift	0.73	0.54	-0.32	2.43	$2.84 \cdot 10^{-2}$	$8.09 \cdot 10^{-4}$	4.18	0.79
Hdrift	0.41	0.16	0.95	2.06	$1.25 \cdot 10^{-2}$	$1.56 \cdot 10^{-4}$	-7.33	0

When doing a mesh convergence test it is beneficial to consider the time spent on the total calculation done in Wadam. A finer grid can give a more accurate numerical result but requires more computational power or time. In Figure 7.4 the time is plotted against the total number of panels in the model with linear and logarithmic axis. The labels are the mesh sizes. As can be seen from the figure, increasing the number of panels in the model, increases the calculation time almost linearly. For the mesh sizes from 8 m to 10 m, Wadam uses around 20 s to calculate the results for this specific case. The finest mesh used almost 14 hours on the same calculation, while the second finest mesh size only used about 18 minutes, see Table 7.2.

Based on the relative difference in Figure 7.1, the order of accuracy, the convergence ratio, variance, and the standard deviation for the data from Table 7.1, and considering the time spent on calculating the results, the mesh size with a panel length of 2 m was chosen. This mesh size uses around 18 minutes to run and gives satisfying results.

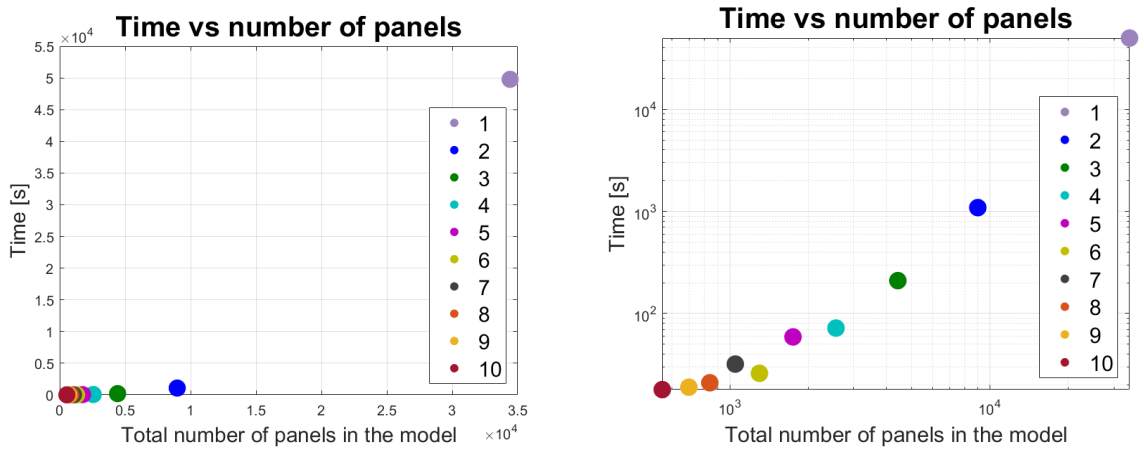

(a) Linear axis.

(b) Logarithmic axis.

Figure 7.4: Time vs number of panels.

Table 7.2: Total number of panels for each mesh size and the corresponding time spent on the calculation in Wadam.

Mesh size $[m]$	Number of panels	Time $[s]$
1	34418	49774
2	8982	1089
3	4426	210
4	2560	72
5	1750	59
6	1300	26
7	1050	32
8	838	21
9	696	19
10	550	18

7.2 Verification of the results

In order to verify the results from the HydroD analysis, the results were compared against results provided for the typical tanker scaled to a Brazilian FPSO size. The mesh size used in the calculation of the provided FPSO were not available, but the total number of panels was provided. The results are based on a calculation with 7598 panels, while the chosen mesh size of 2 m gave 8982 panels. From the mesh convergence study, a mesh

size from around 3 m which has 4426 panels should yield comparable results. Hence the difference in mesh size should not be an issue when comparing the results. Plotting the RAO and the drift forces calculated with the conservation of fluid momentum method in surge shows that the agreement between the calculations was excellent. The graphs are attached in Appendix B.

7.3 RAO

The RAO's for surge, heave and pitch for the three geometries are plotted in Figure 7.6. The three geometries have the same mass, but the wall sided geometry has less draft than the two others because it has more volume at the bow of the ship, see Figure 5.2. This extra volume results in extra buoyancy which reduces the draft from 20.8 m for the geometries with and without bulb, to 20 m. A reduction of 0.8 m corresponds to 3.85% of the original draft. The center of gravity was moved 4 m forward to keep an even keel. Figure 7.6 shows that the response of the ship with or without bulb is more or less identical for surge, heave, and pitch. Nevertheless, the wall sided geometry differs from the two others.

Compared to the geometry with and without bulb, the wall sided geometry has a larger block coefficient (C_B) and higher beam-draft ratio (B/D), see Table 7.3. Figure 7.5 demonstrates that a larger C_B gives a higher response in heave, but a higher beam-draught ration leads to a smaller response. Note that the graph is for heave motion at resonance for a 2D problem in head sea waves, hence the block coefficient is a sectional area coefficient in this graph. The graph is therefore not fully representative for the 3D problem but could give an indication.

Table 7.3: Geometrical parameters.

	Geometry with bulb	Wall sided geometry	% change
B/D	2.789	2.9	3.98
C_B	0.857	0.889	3.73
Water plane area	$1.749{\cdot}10^4$	$1.755{\cdot}10^4$	0.34

The increase in percentage for B/D and C_B are almost identical, the parameters will therefore contradict each other, and this graph cannot be used to draw any conclusion for the heave motion.

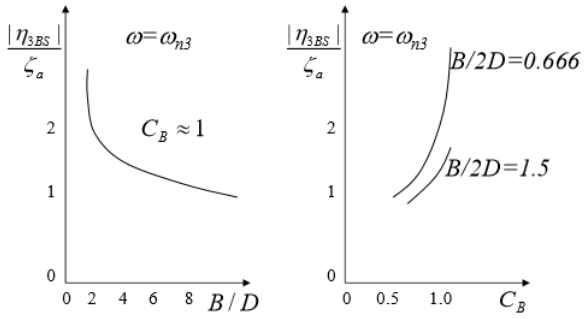

Figure 7.5: Heave amplitude response at resonance for different beam-draught ratios and different block coefficient in 2D for head sea waves (Greco, 2018).

In the experiment done by MARIN (Buchner, 1996) the pitch response for the traditional tanker is smaller than the sharp alternative geometries they tested for. Looking at Figure 7.6c, the wall sided geometry, which is the most similar geometry to the traditional tanker, also has a smaller pitch motion than the geometries with and without bulb.

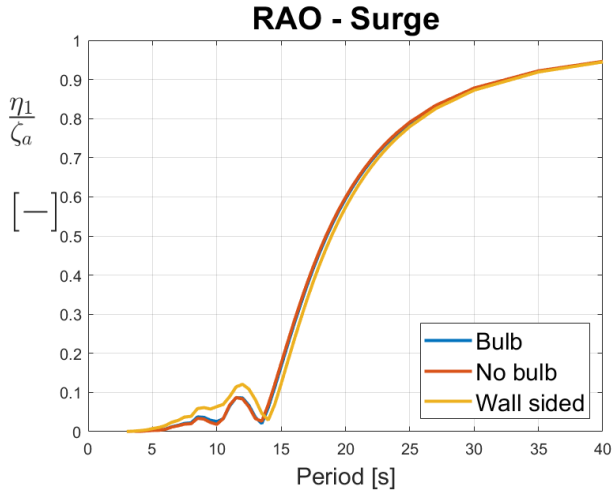

(a) Surge for the three geometries.

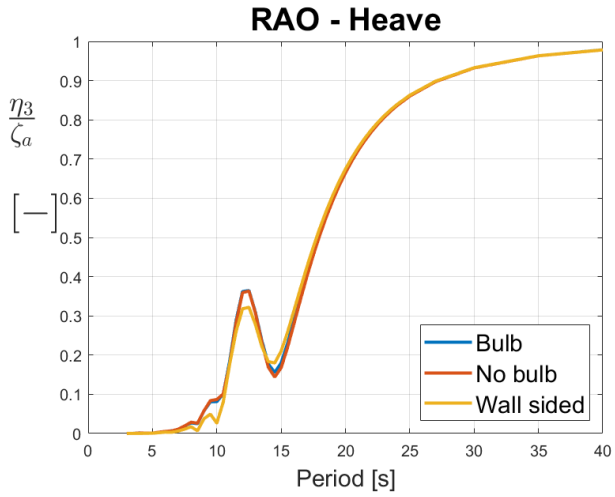

(b) Heave for the three geometries.

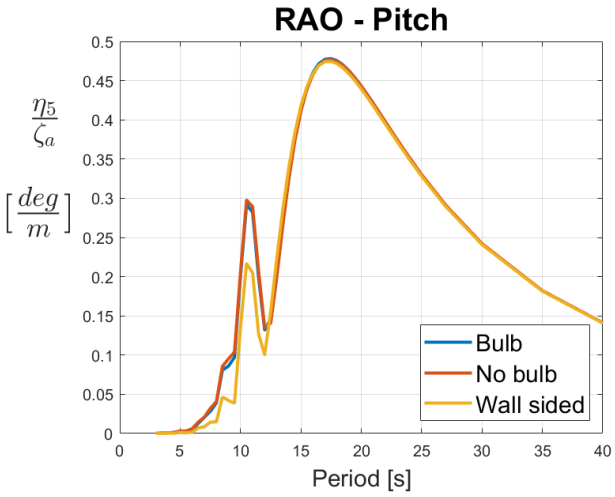

(c) Pitch for the three geometries.

Figure 7.6: RAO's for the three geometries.

In Figure 7.7 the frequency dependent excitation force and damping are plotted for surge, heave and pitch for the geometry with bulb and the wall sided geometry. Figure 7.6 demonstrates that the geometries with and without bulb have very similar RAO's, while the wall sided geometry has higher surge and smaller heave, and pitch motions. The geometry with bulb is therefore used to represent both the geometry with and without a bulb in Figure 7.7. The wall sided geometry has the largest response, excitation force, and the largest damping in surge, while in heave the geometry with bulb has the largest motion. The heave damping is close to equal for the geometries. Studying the graphs, the excitation force is the variable that affects the RAO's the most, since the highest excitation force also gives the largest motions. The excitation forces and damping are 10 times larger in heave than in surge. In pitch, the geometry with a bulb has the largest motion and damping.

The wall sided geometry has a larger water plane area and more volume in the front causing higher damping and added mass in the vertical direction, which cause a smaller heave and pitch motion. The voluminous wall sided bow diffracts more waves inducing higher surge motion than the geometries with and without bulb which has more flare and less volume.

Since the geometries are not fore-aft-symmetric the heave and pitch motions will be coupled. In Appendix C the graphs show the coupled damping B_{13}, B_{15}, and B_{35}. The coupled damping is significant, and the RAO's can therefore not be explained by the uncoupled damping alone.

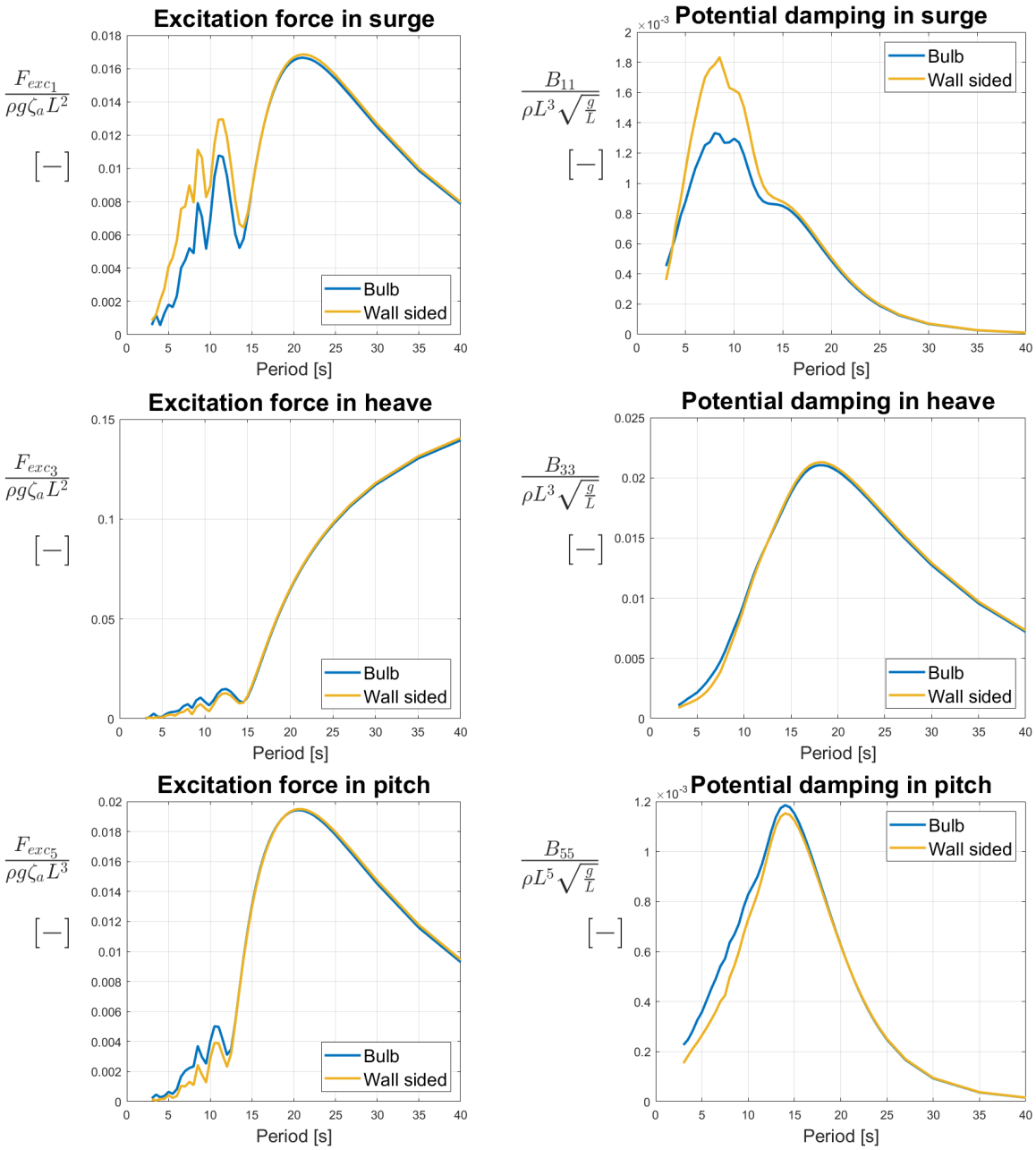

Figure 7.7: Excitation force and potential damping in surge, heave and pitch.

7.4 Drift forces

The mean drift force in surge is plotted in Figure 7.9a and Figure 7.8a. In Figure 7.9a the results are calculated with the direct pressure integration method, while Figure 7.8a shows the results calculated with the method of conservation of fluid momentum. The drift forces for the geometries with and without bulb are very similar for the two methods, but the results for the wall sided geometry has a large deviation for periods lower than 10 s.

The second-order forces in surge, sway, and yaw for all the geometries are attached in Appendix D. The mean drift coefficient in sway is of an order 10^{-5} while the forces in yaw are of the order 10^{-3}, computed with the direct pressure integration. With the conservation of fluid momentum method, the mean drift coefficient in sway and yaw are of the order 10^{-7} and 10^{-5}. These forces are small compared to the mean drift force in surge, which has a coefficient of the order 10, and are therefore not dimensional for the problem. Since the analysis are done in head sea waves, the sway and yaw are expected to be small.

The study on *The Influence of the Bow Shape of FPSO's on Drift Forces and Green Water* by Buchner (1996), showed that the calculated drift force for the traditional tanker in surge was larger for small periods than for the alternative geometries with sharper bows. The paper concluded that the reason for this was that the traditional tanker has a wider bow that was capable of diffracting waves back into the incoming waves, causing a larger drift force. The same can be observed in Figure 7.8a.

Hanssen et al. (2013) also compared the drift forces in surge for three different bow shapes. Figure 4.3a demonstrates that *Bow variation 2*, illustrated in Figure 4.2, cause the largest mean drift force in surge. This substantiates Buchner's conclusion, that the ability of the vessel to diffract the waves is important when considering the mean drift forces. The plot in Figure 4.3a is calculated using the conservation of fluid momentum method and can be qualitatively compared with Figure 7.8a. The width and length of the FPSO's are similar, but the draught differs with 8 m since the draft is 12 m for the *Bow variation 2* and 20 m for the FPSO with wall sided bow. Since the wave amplitude is assumed small as a consequence of using potential theory, the difference in the draft will only have a small impact because the effect of the waves declines with submergence. The linear effects decrease exponentially, while the second-order slowly varying effects

subsides more slowly. Nevertheless, the mean drift force in surge for the *Bow variation 2* can be used as a tentative maximum limit for the second-order forces, because it is shaped like a straight wall, causing all the diffracted waves to contribute to the mean drift force in surge for head sea waves. Comparing Figure 7.8a with *Bow variation 2*, all the bows in this thesis results in smaller mean drift forces in surge.

Looking at the shapes of the bows in the paper from Hanssen et al., 2013, and the bows in this thesis, the *Base case* looks comparable to the FPSO with wall sided bow. The drift force in surge for the *Base case*, given in Figure 4.3a and Figure 4.3b, goes from around 170 to 130 kN/m^2 for the periods lower than 9 s. The *Base case* is 305 m long and 55 m wide. Making the force non-dimensional the drift force coefficient in surge for the periods lower than 9 s vary from 1.7 to 1.3. This corresponds well with the results in Figure 7.8a. Both cases peaks at 11-10 s, and the drift coefficient goes quickly to zero for periods higher than around 14 s.

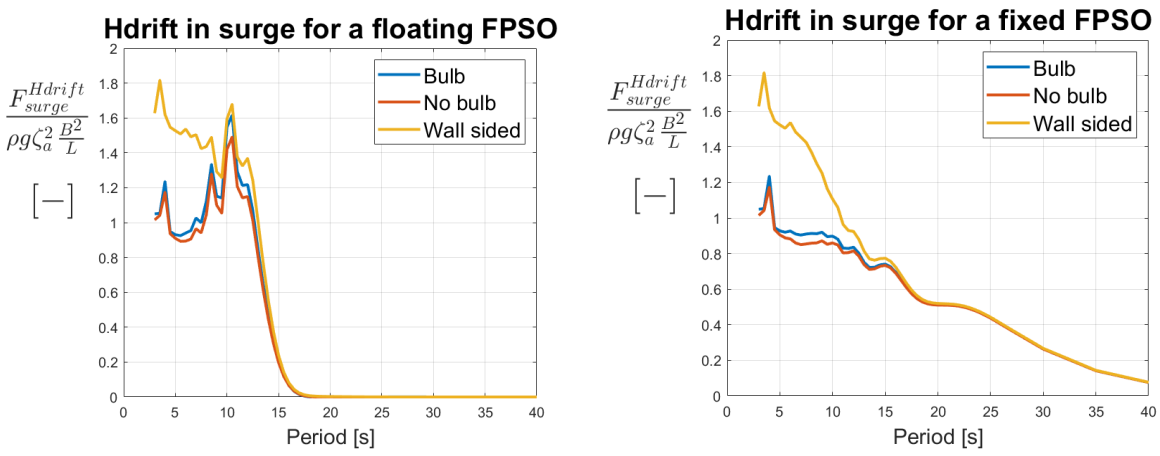

(a) Floating FPSO. **(b)** Fixed FPSO.

Figure 7.8: Mean drift forces in surge calculated with the conservation of fluid momentum method for three different bow geometries for freely floating and fixed FPSO's.

The direct pressure integration method and the conservation of fluid momentum method yields quite similar results. Both graphs demonstrate results in the same order, nevertheless, *Hdrift* gives almost identical results for the geometries with and without bulb, while *Drift* gives clearly higher drift forces for the geometry with bulb.

In Figure 7.8b and Figure 7.9b the drift forces for the fixed FPSO's are given. Comparing them to the floating FPSO's in Figure 7.8a and Figure 7.9a the drift forces from 3 s to

around 6 s are identical, meaning that the drift forces for the lower periods mainly originates from the diffraction of waves. For the higher periods for the freely floating case the drift forces has a peak at the natural period of the FPSO, around 10.5 s, and goes quickly towards zero for higher periods. The increase in the drift forces at the natural period comes from the increased relative motion between the vessel and the free surface. At periods higher than 17 s the drift force in surge is almost zero. That is because at these high periods the FPSO follows the waves, causing small relative motions and little diffraction of the waves. The peak at 10-11 s in the mean drift force in surge is naturally not observed for the fixed FPSO because the vessel does not move. Hence, it cannot follow the motion of the waves, giving a slowly decrease in the drift force for higher periods.

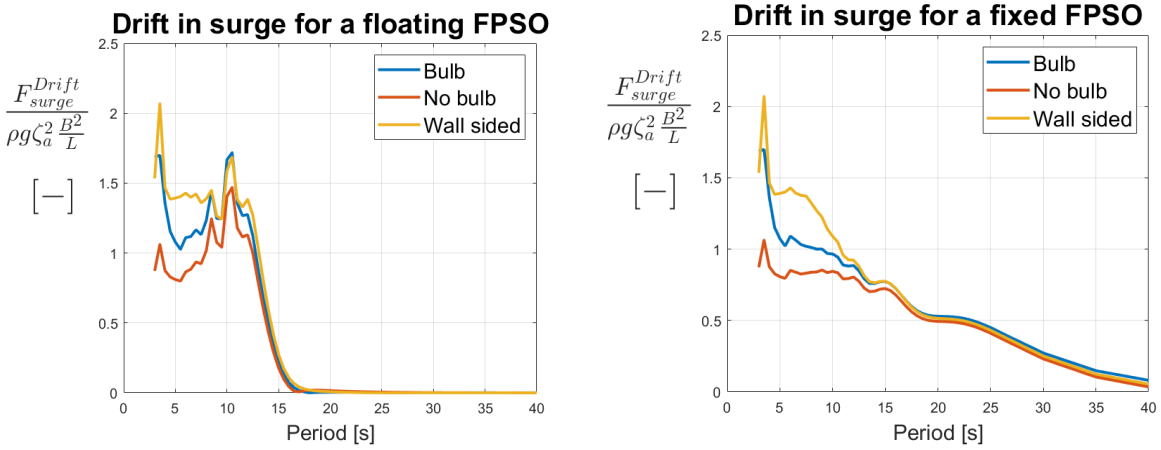

(a) Floating FPSO. **(b)** Fixed FPSO.

Figure 7.9: Mean drift forces in surge calculated with the direct pressure integration method for three different bow geometries for freely floating and fixed FPSO's.

7.4.1 Comparison of the direct pressure integration method and the conservation of fluid momentum method

In the preliminary work for the master thesis, the project thesis, the three different bow geometries were created. To make the wall sided geometry several points, lines and panels needed to be moved and recreated in the bow part of the FPSO. Due to limited time during the project thesis, the wall sided geometry turned out rough as presented in Figure 7.10c. Later the geometry was improved and smoothed out, pictured in Figure 7.10d. The improved geometry was used for the calculations presented in the previous part of the Chapter. The drift forces calculated with the direct pressure integration method, *Drift*, and the conservation of fluid momentum, *Hdrift*, are given in

Figure 7.10a and Figure 7.10b respectively. Observed from the plots, the direct pressure integration method gives diverging results for periods below 10 s. The method of fluid momentum provide more consistent results.

The direct pressure integration method calculates velocity gradients at the surface of the geometry, while the conservation of fluid momentum uses the far-field approach. Hence, the direct pressure integration method is more sensitive to geometrical approximations, especially geometrical singularities on the body surface, which could be a source for numerical errors (Greco, 2018). The Wadam user manual states that a higher mesh refinement is normally needed when the pressure integration method is used to obtain the mean drift forces (DNV GL, 2019b).

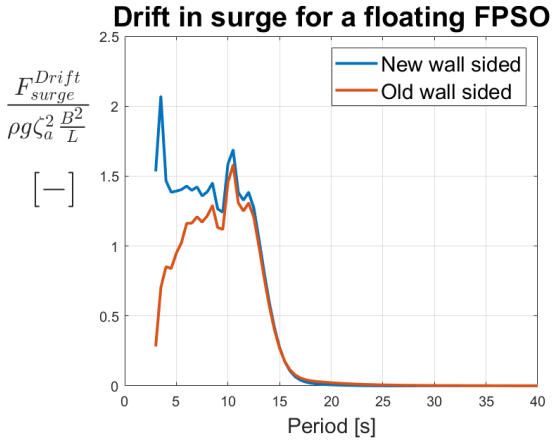

(a) *Drift* in surge for the old and the new bow geometry.

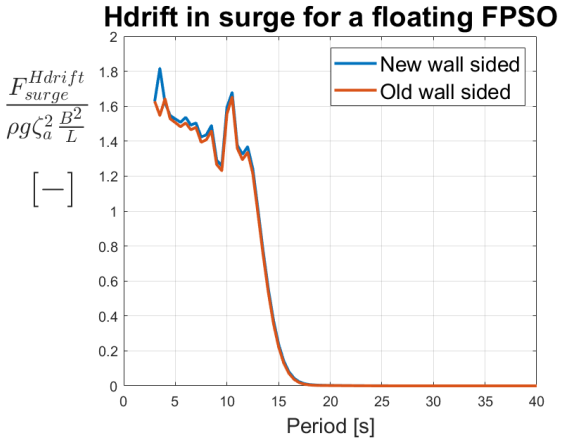

(b) *Hdrift* in surge for the old and the new bow geometry.

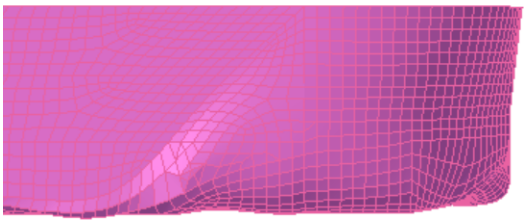

(c) Old bow geometry.

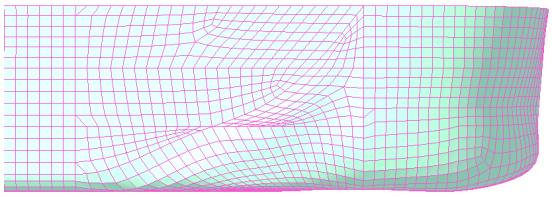

(d) New bow geometry.

Figure 7.10: *Drift* and *Hdrift* in surge for an uneven and a smooth geometry with the respectively geometries.

Chapter 8

Results from ComFLOW

In the following Chapter, the results from ComFLOW are presented. First, a convergence test is conducted for the domain size, meshing of the surface of the geometry, and refinement of the grid in the domain. The period of the waves was 10 s and the amplitude was 1 m in all the cases. Then the results for the floating and fixed FPSO with a bulb is presented. The periods and steepnesses analysed are presented in Table 8.1. Waves with 90% of maximum steepness was only analyzed for the floating FPSO. Finally, the results for the three different bows are presented. The bows were subjected to waves with a period of 11 s and an amplitude corresponding to a steepness of 10% of the maximum steepness defined as the breaking criteria in Section 3.10.2 as $s_{max} = H/\lambda = 1/7$.

The analyzes with a steepness of 10% of the maximum wave steepness is expected to provide close to linear results which should be comparable to the results from Wadam. For increased wave steepnesses more nonlinearities are introduced which is anticipated to predict relatively higher mean drift forces.

Table 8.1: Overview of the periods and amplitudes, as a percentage of the maximum steepness ($s_{max} = H/\lambda = 1/7$), analyzed. The amplitudes corresponding to 90% of maximum steepness were only checked for the floating case.

	Amplitude $[m]$			
Steepness[%] / Period $[s]$	10	50	70	90
4	0.18	0.90	1.25	1.61
8	0.72	3.57	5.00	6.43
11	1.35	6.75	9.45	12.15

8.1 Testing for convergence for a fixed FPSO

CFD analysis is, in addition to the mesh size of the geometry as in Wadam, sensitive to the extent of the domain, the time step, and grid size of the domain. In ComFLOW four different extents of the domain, mesh sizes of the surface of the geometry, and the grid sizes of the domain were tested for convergence, with a refinement ratio of $\sqrt{2}$. The time step was automatically adjusted and was therefore not necessary to check. All the tests had a wave period of 10 s and a wave amplitude of 1 m, to make them comparable with the linear results from Wadam. When testing the convergence for the domain size the geometry with the medium mesh refinement was used. The fine grid refinement, see Table 8.8, was used both when investigating the domain size and the mesh size of the geometry for convergence.

8.1.1 Domain

To ensure no reflections or other interferences from the boundaries of the domain, four different domain sizes were investigated. The smallest domain was chosen slightly larger than the ship, and a scaling ratio of $\sqrt{2}$ was used to dimension the other domains. An overview of the domain sizes is tabulated in Table 8.2. As can be observed from the table, the dimension in the z-direction was kept constant. This dimension was chosen large enough not to get bottom effects but was not further optimized.

Table 8.2: Different domain sizes.

	Coordinates $[m]$					
Domain	X_{min}	X_{max}	Y_{min}	Y_{max}	Z_{min}	Z_{max}
Small	-220	300	-220	0	-200	20
Medium	-312	425	-312	0	-200	20
Large	-441	601	-441	0	-200	20
Very large	-623	849	-623	0	-200	20

Figure 8.1 shows the forces in x- and z-direction for the domains. Since the analysis starts with still water, the time it takes the waves to reach the FPSO depends on the domain. Observed from Figure 8.1a, the small and medium domain have declining amplitudes, while the large and very large domain looks more constant. In the z-direction, the force amplitudes are more varying. A time interval with relatively constant amplitudes was

subjectively chosen for each domain size and direction. In Appendix E.1 the forces are presented with the indicated stationary time intervals used for the convergence test of the domains. It should be pointed out that the smallest domain does not have a clear time interval with relative constant amplitudes. Nevertheless, the two most representative periods were subjectively chosen. Hence, the smallest domain was affected by the boundaries and was not a suitable domain size for further calculations.

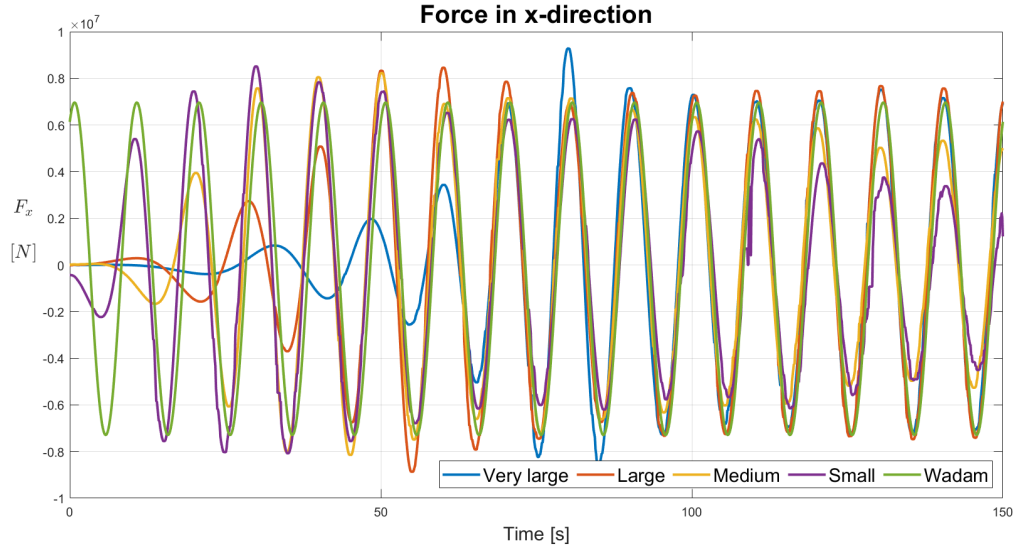

(a) Force in x-direction.

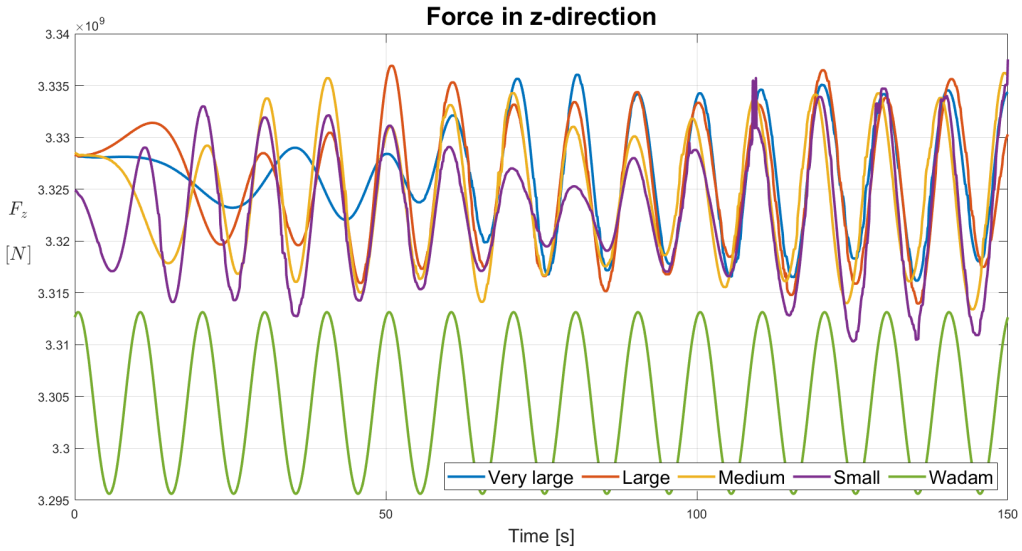

(b) Force in z-direction.

Figure 8.1: The forces for the different domains in x- and z-direction from ComFLOW plotted with the results from Wadam over time.

Reflections

The lateral boundary of the domain does not have any specific boundary condition implemented. Reflections from that side are therefore expected. The domain needs to be large enough so the reflections from the side do not have time to build up and contaminate the results within the chosen time frame. The reflected waves from the FPSO will have the same group velocity as the regular incident waves. Equation (8.1) presents the expression for the group velocity for waves at deep water. ω is the angular frequency of the wave, and k is the wave number. A wave period of 10 s gives a group velocity of 7.80 m/s.

$$c_g = \frac{\partial \omega}{\partial k} \overset{Deep\,water}{=} \frac{1}{2}\frac{\omega}{k} \tag{8.1}$$

A prediction for when the reflections will occur can be done by calculating the time it takes the wave to travel from the wave maker at the inlet to the ship, and then the time it takes the reflected wave to propagate to the side of the domain and back again to the FPSO. Table 8.3 presents the time range for the expected first reflections to affect the results. The lower limit is the time it takes the incoming wave to reach the front of the bow, and then to the side and back again. While the upper limit is the reflections from when the waves hit the stern, and then to the side and back again. As can be seen from the table, both the small and medium domain are expected to have interferences in the results within the 150 s that are analyzed.

Table 8.3: Time range for the expected first reflections for the different domains.

Domain	Time range [s]
Small	77 - 97
Medium	113 - 133
Large	162 - 182
Very large	232 - 252

From Figure 8.1b the small domain can be observed to have very small amplitudes around 80 s, and this is also the time when the amplitudes start to decrease in Figure 8.1a. This corresponds well with the estimated time of interference from the reflected waves. Looking at the force in z-direction for the medium domain, lower amplitudes can be observed around 90 s. This is earlier than expected from the estimation in Table 8.3.

Fast Fourier transformation

There are several ways to extract the amplitude corresponding to a specific load frequency of the data from a time series. *Peak2Peak* is a Matlab function that returns the difference between the minimum and maximum value of the forces. This method does not take into account any variations of the amplitudes or contributions from slowly varying loads, consequently, it gives an upper limit for the amplitudes. Fast Fourier transformation (FFT) is used to extract the wave frequency part of the force, which is consistent with the results from Wadam. With this method contributions from other frequencies are avoided, see Figure 8.2. Because the FFT extracts the amplitude of the force corresponding to the incident waves, it is expected to be more comparable to the results from Wadam than the *Peak2Peak* methods which does not differentiate the contributions from distinctive frequencies. Looking at Table 8.4 the deviations from Wadam is significantly lower when using FFT than the *Peak2Peak* method.

Table 8.4: Amplitude of the force from Wadam and the amplitude of the force for the very large domain from ComFLOW found with *Peak2Peak* and FFT in MATLAB given in N and non-dimensional with respect to $\rho g \zeta_a (\frac{B^2}{L}^2)$ and the deviation from Wadam given in percent for the two methods.

Direction	Wadam		*Peak2Peak*			FFT		
x	$7.13 \cdot 10^6 N$	6.42	$7.43 \cdot 10^6 N$	6.69	4.21%	$7.29 \cdot 10^6 N$	6.56	2.24%
z	$8.76 \cdot 10^6 N$	7.88	$9.44 \cdot 10^6 N$	8.50	7.76%	$8.68 \cdot 10^6 N$	7.81	0.91%

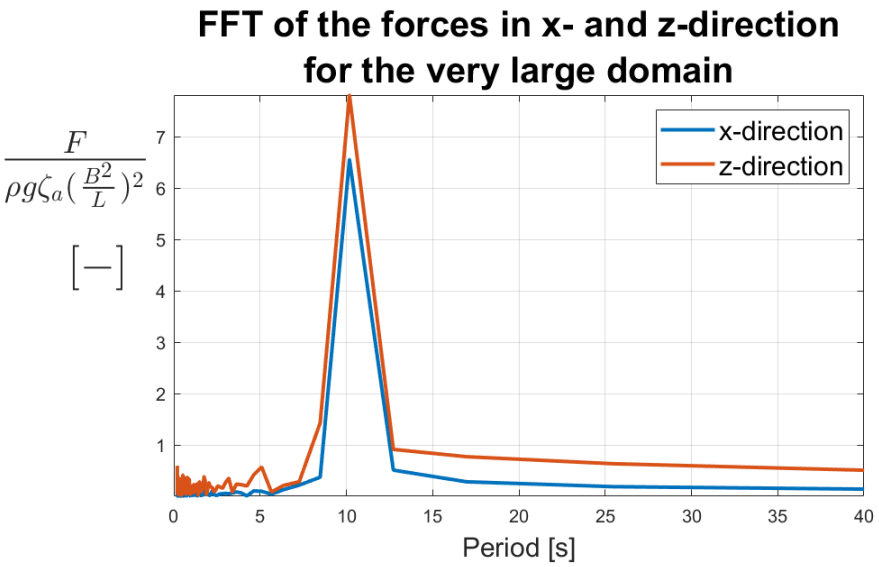

Figure 8.2: FFT for the force in the x- and z-direction for the very large domain.

Convergence ratio and order of accuracy

To investigate if the results numerically converge by enlarging the domain size, the results from ComFLOW were compared to the results from Wadam. The deviation is presented as the percent of deviation from the Wadam results. Note that in Figure 8.1b the mean value for the force in z-direction in ComFLOW, has an offset from the mean value from Wadam. The reason for this is not clear, but it could originate from an inaccurate draft. From Figure 8.3b it can be observed that the deviation is less than 1%. A 1% deviation is insignificant when the objective is to decide the effect of the domain size. Nevertheless, that is causing the deviation between the Wadam and ComFLOW results for the force in the z-direction to increase, because it converges away from the mean value from Wadam.

Since the force in surge oscillates around zero, and the mean value of the force is of the order 10^5 N and the amplitudes are of the order of 10^7 N, the mean value is very sensitive to the choice of the stationary time interval. By just shifting, expanding, or reducing the range with five time steps, corresponding to half a second, the mean value could in some cases doubled or halved. The results in z-direction have amplitudes in the order of 10^6 N and a mean value of 10^7 N. The mean value is therefore not so sensitive to the choice of the stationary time interval.

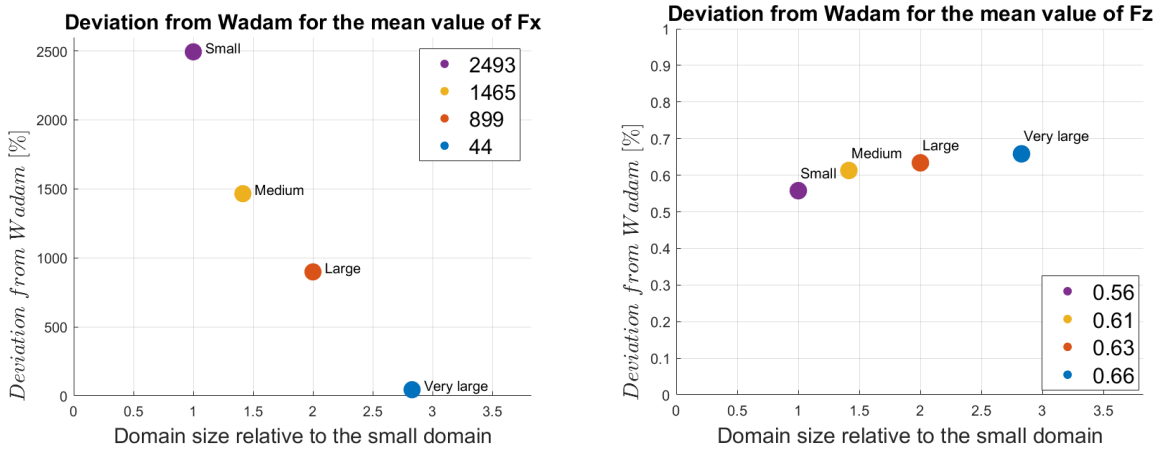

(a) Deviation from the Wadam results for the mean value of the force in x-direction.

(b) Deviation from the Wadam results for the mean value of the force in z-direction.

Figure 8.3: Deviation from the Wadam results for the mean value of the forces for the convergence of the domain size.

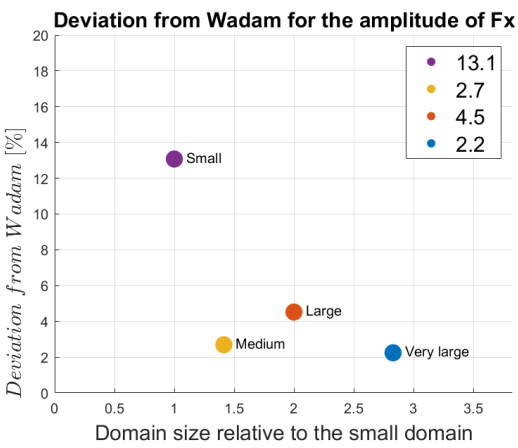

(a) Deviation from the Wadam results for the amplitude of the force in x-direction.

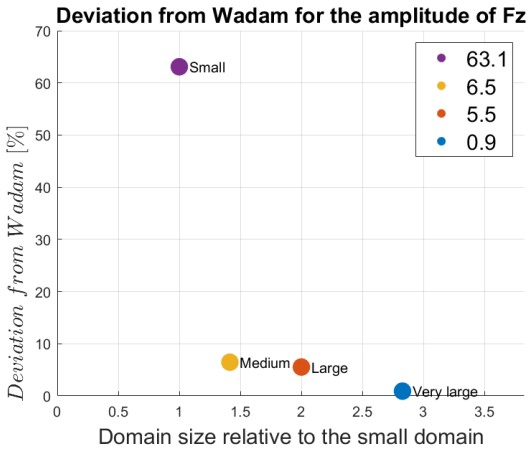

(b) Deviation from the Wadam results for the amplitude of the force in z-direction.

Figure 8.4: Deviation from the Wadam results for the amplitude of the force for the convergence of the domain size.

To check if the results in Figure 8.3 and Figure 8.4 converge, and if so quantifying it, the order of accuracy and the convergence ratio is calculated using the three largest domains. Table 8.5 presents the results. The convergence ratio indicates that none of the amplitudes nor the mean values converges monotonically. The amplitude for the force in x-direction has an oscillatory convergence, while the rest diverges. Since none of the cases shows monotonically convergence, the order of accuracy is not calculated.

Table 8.5: The convergence ratio for the domains giving the deviation between the results from Wadam and ComFLOW.

Deviation	Mean force X	Amplitude X	Mean force Z	Amplitude Z
R	1.51	-1.24	1.17	5.00

A simulation of the very large domain in ParaView is embedded in Appendix H. It presents a typical simulation used in the post-processing of the analysis.

Despite the fact that the convergence ratio does not indicate convergence, a larger domain gives smaller discrepancies from the Wadam results. Based on Figure 8.1, Figure 8.3, Figure 8.4 and Table 8.5, a very large domain is chosen to avoid interferences from the boundaries of the computational domain.

8.1.2 Geometry

Four different mesh sizes for the FPSO geometry were tested for convergence. The target size of the coarsest mesh had a triangle mesh size of 20 m. A refinement ratio of $\sqrt{2}$ was used to find the three other mesh sizes, see Table 8.6. Since the analysis started directly with waves, see Figure 8.6, the number of stationary periods increased compared to starting from still water. There is still a transient phase because the waves are defined as undisturbed waves, hence, during the first time steps the diffracted wave field is calculated. The stationary area was subjectively chosen from 50 to 140 s for all forces and directions.

Table 8.6: Different mesh sizes for the geometry.

Geometry	Coarse	Medium	Fine	Extra fine
Mesh size $[m]$	20.00	14.14	10.00	7.07

Figure 8.5 shows the extra fine mesh of the geometry. As seen from the figure the mesh is able to capture the complex shape of the FPSO quite good. The mesh is unstructured and provides finer grid near curves.

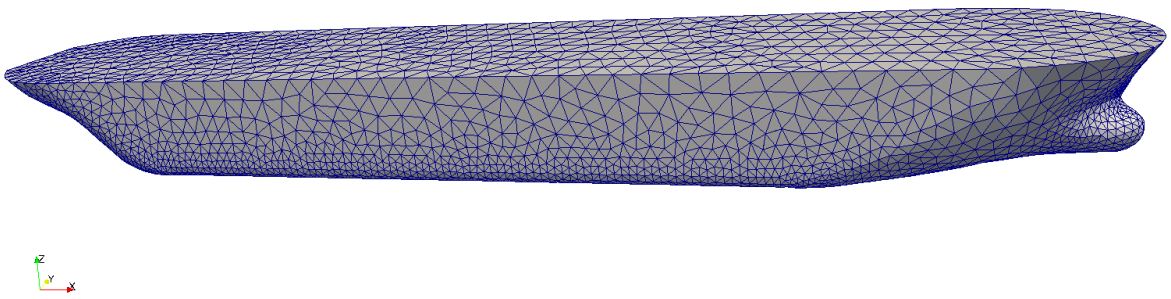

Figure 8.5: Extra fine mesh size of the geometry of the FPSO

Reflections

When starting directly with waves, the time it takes the waves to travel from the ship side and back to the ship is the time when the first reflections is expected. The time for the effect of the reflections to interfere was estimated to 153 s, which is just outside the time frame for the analysis. Based on this, the reflected waves should not have time to interfere with the results for a very large domain and periods up to 10 s.

The forces in x- and z-direction are presented in Figure 8.6. Studying Figure 8.6a, the graphs are almost inseparable from each other. While the forces in the z-direction are more have smaller amplitudes, which makes it easier to see the deviations between the plots for the different mesh sizes.

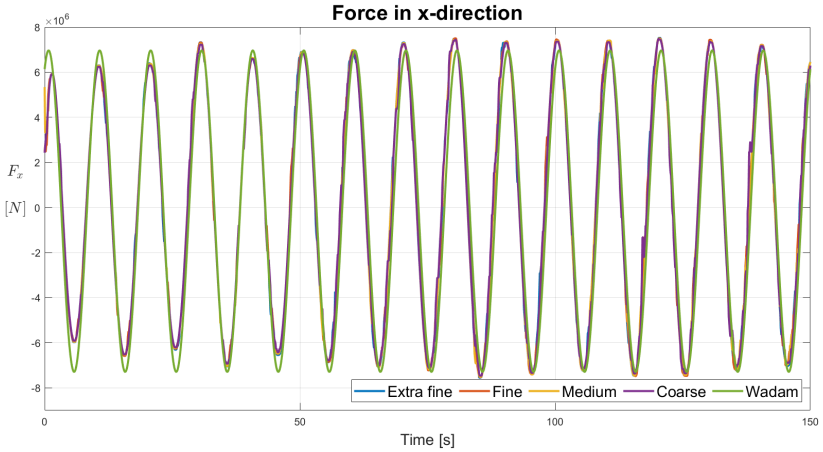

(a) Force in x-direction.

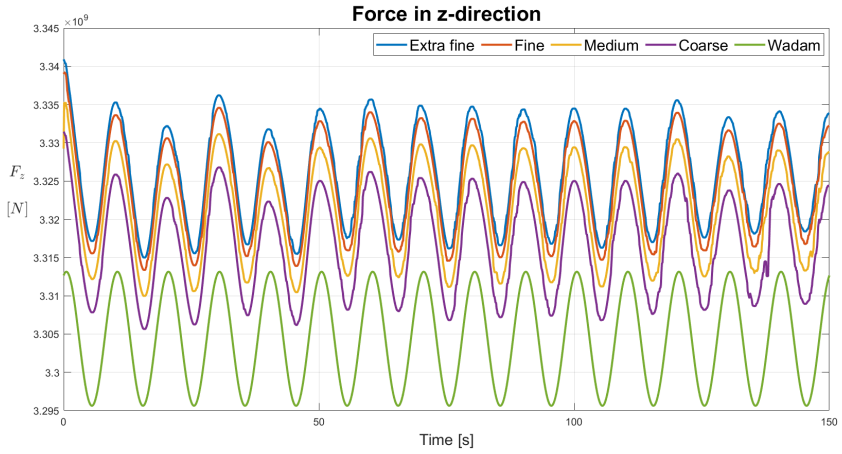

(b) Force in z-direction.

Figure 8.6: The forces for the different geometries in x- and z-direction from ComFLOW plotted with the results from Wadam over time.

Convergence ratio and order of accuracy

The deviation for the results from ComFLOW from Wadam is plotted for the different mesh refinements in Figure 8.7 and Figure 8.8. The amplitudes were found with FFT. Observed from the plots the coarse grid is the most accurate in x-direction, while not in the z-direction. The mean values for the force in the x-direction is very sensitive for the choice of the stationary time interval, which means that the similar results between Wadam and ComFLOW with the coarsest grid could just be a coincident. The deviations for all values except the mean value of the force in x-direction, are less than 3.5% for all the grid sizes.

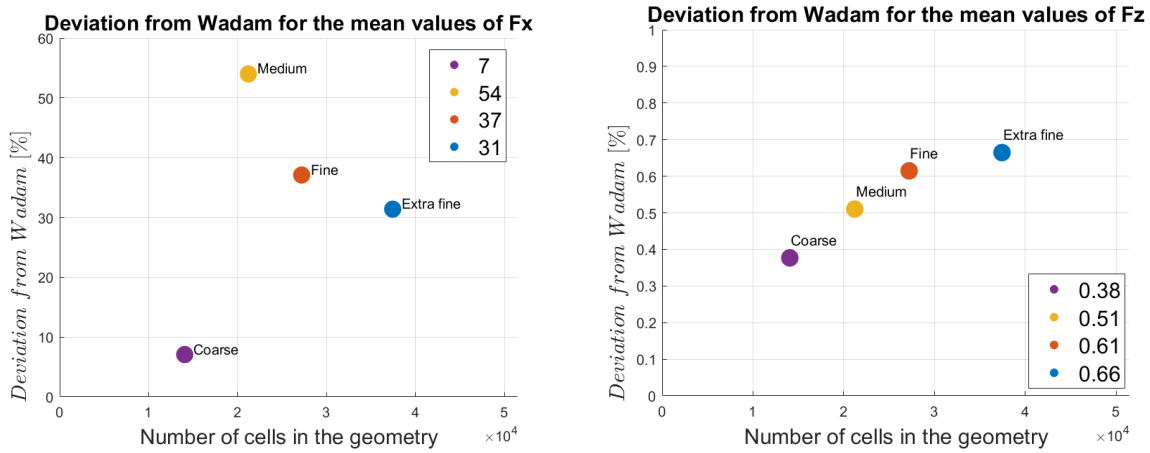

(a) Deviation from the Wadam result for the mean value in x-direction.

(b) Deviation from the Wadam result for the mean value in z-direction.

Figure 8.7: Deviation from the Wadam result for the mean value for the convergence of the surface grid of the geometry.

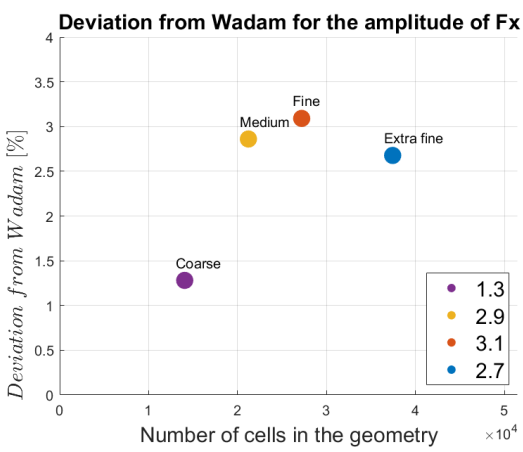

(a) Deviation from the Wadam result for the amplitude in x-direction.

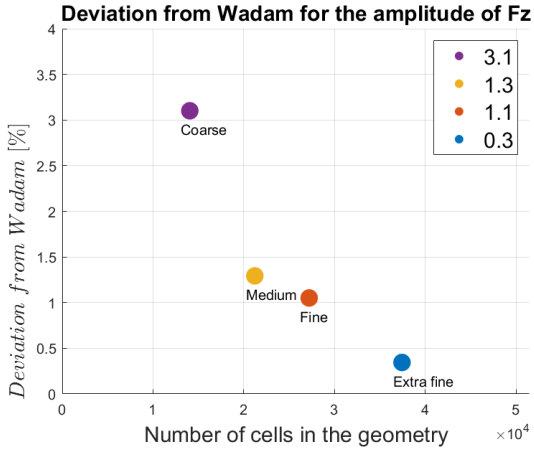

(b) Deviation from the Wadam result for the amplitude in z-direction.

Figure 8.8: Deviation from the Wadam result for the amplitude for the convergence of the surface grid of the geometry.

The convergence ratio and order of accuracy for the three finest mesh sizes for the deviations between the linear results from Wadam and non linear results from ComFLOW are given in Table 8.7. The convergence ratio indicates that the mean forces converge, while the amplitude for the force in x-direction has an oscillatory convergence, and the amplitude for the force in the z-direction diverges. The order of accuracy imply a convergence of an order of around 4 for the mean forces.

Table 8.7: Convergence ratio and order of accuracy for the geometries giving the deviation between the results from Wadam and ComFLOW. The gray cells indicates OA of no interest because the R does not indicate monotonically convergence.

Deviation	Mean force X	Amplitude X	Mean force Z	Amplitude Z
R	0.34	-1.80	0.48	2.92
OA	4.41	1.69	3.75	4.37

The number of cells in the domain was about 2.9 million cells in the analysis of the geometry mesh, while the vessel only occupies about 15% of those cells. A finer surface mesh would give a more accurate shape of the geometry, but because of the VOF method, explained in Section 3.8, the number of solid and open cells does not change much. It is therefore not surprising that the computational time does not vary significantly for the mesh size of the geometry. Considering Figure 8.6, Figure 8.7, Figure 8.8, and Table 8.7,

the finest grid refinement was chosen.

8.1.3 Domain grid

To investigate convergence for the grid refinement four different grid sizes were chosen. The number of cells at refinement level zero and the length, width, and height in meters for the finest refinement level is presented in Table 8.8. The finest grid had about 7.2 million cells, while the coarsest grid had about half a million cells in the computational domain.

Table 8.8: Overview of the grid refinement, where the number of cells at refinement level zero is given for x-, y- and z-direction, and the length, width and height is the size of the finest grid element.

Refinement	Number of cells at refinement level 0	Length $[m]$	Width $[m]$	Height $[m]$
Extra fine	69 27 14	0.67	0.72	0.49
Fine	49 19 10	0.94	1.03	0.67
Medium	34.5 13.5 7	1.33	1.44	0.98
Coarse	29.5 9.5 5	1.56	2.05	1.38

The forces in x- and z-direction for all but the coarsest grid refinement is presented in Figure 8.9. The coarsest grid did not give useful results and is therefore not included in the convergence study, see Appendix F for the plots of the forces in x- and z-direction. A stationary area was subjectively chosen from 50 to 140 s.

The results from the medium and fine grid appear smooth, while the extra fine grid looks pointy and uneven. The reason for this is not fully understood, but a very fine grids can become numerically difficult to handle

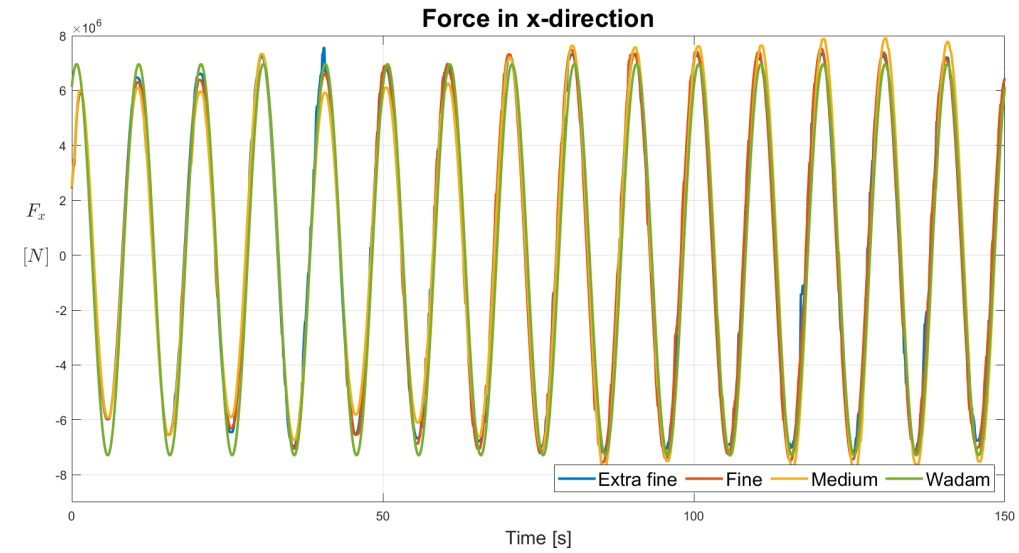

(a) Force in x-direction.

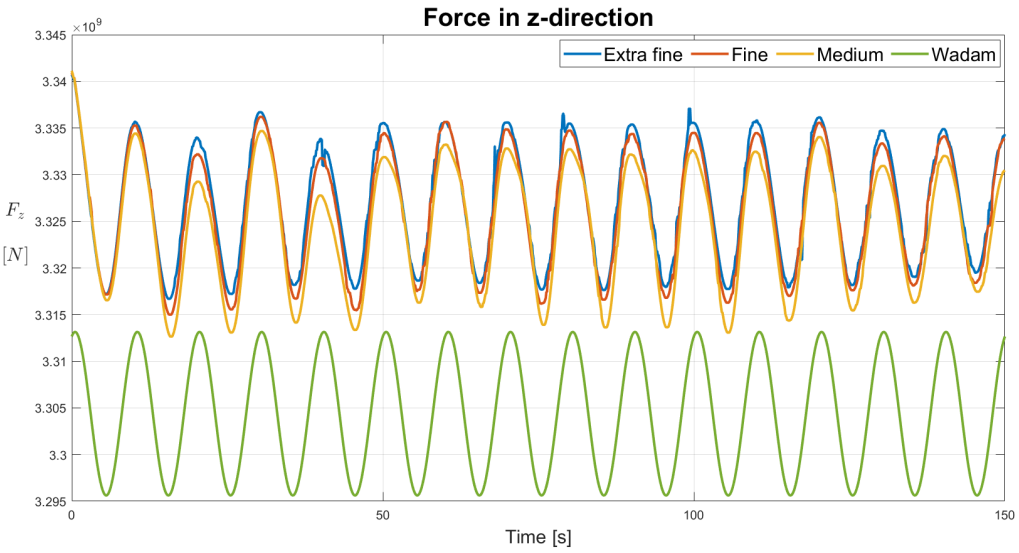

(b) Force in z-direction.

Figure 8.9: The forces for the different grids in x- and z-direction from ComFLOW plotted with the results from Wadam over time.

Convergence ratio and order of accuracy

The deviation of ComFLOW results from the Wadam results for the three finest grid refinements are plotted in Figure 8.9. For the finest grid the deviations from the Wadam results are less than 1% for the amplitudes and the mean value in z-direction. The mean value in x-direction has a discrepancy of only 11%.

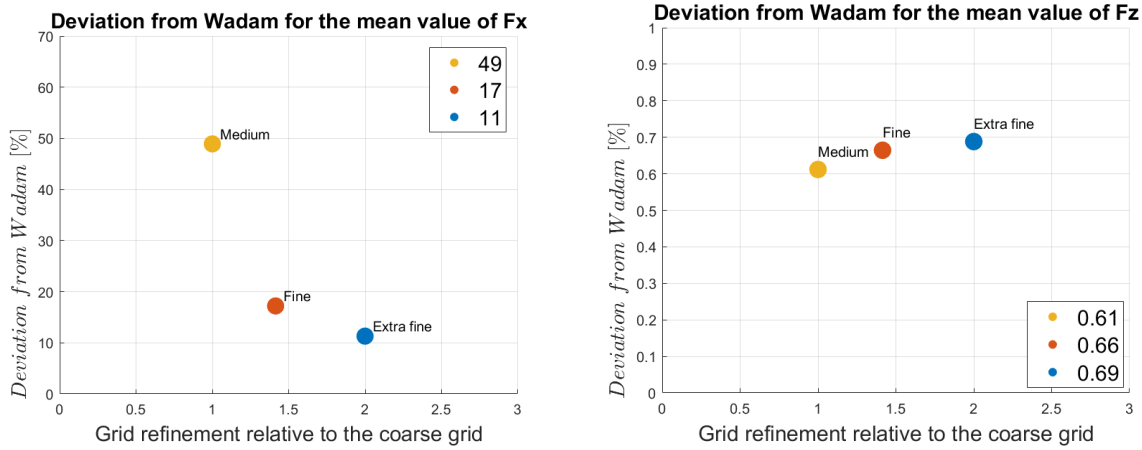

(a) Deviation from the Wadam result for the mean value in x-direction.

(b) Deviation from the Wadam result for the mean value in z-direction.

Figure 8.10: Deviation from the Wadam result for the mean value for the convergence of the grid.

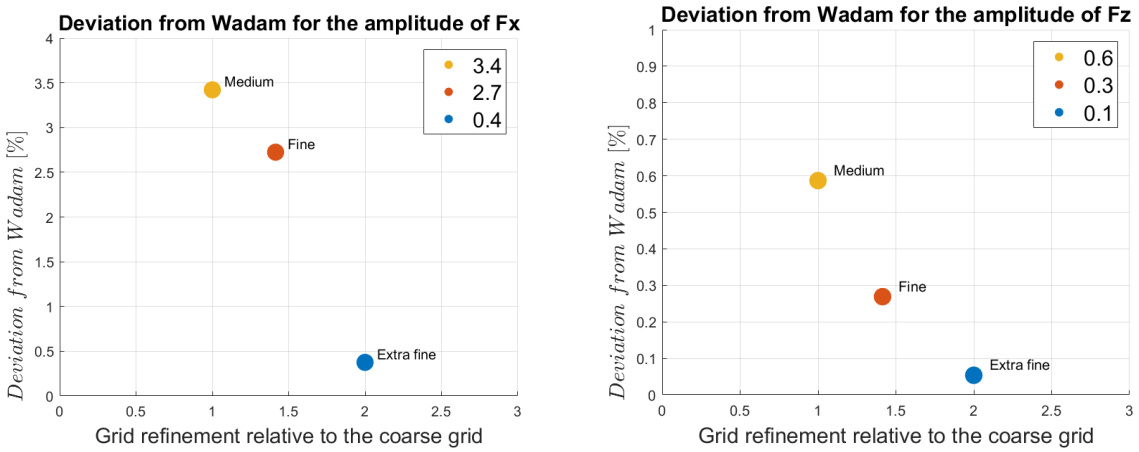

(a) Deviation from the Wadam result for the amplitude in x-direction.

(b) Deviation from the Wadam result for the amplitude in z-direction.

Figure 8.11: Deviation from the Wadam result for the amplitude for the convergence of the grid.

Table 8.9 presents the convergence ratio and the order of accuracy for Figure 8.10 and Figure 8.11. The convergence ratio implies that all but the amplitude in x-direction converges. The order of accuracy varies from 2 to almost 6.

Table 8.9: Refinement ratio and order of accuracy for the grid refinement giving the deviation between the results between Wadam and ComFLOW. The gray cell indicates OA of no interest because R does not indicate monotonically convergence.

Deviation	Mean force X	Amplitude X	Mean force Z	Amplitude Z
R	0.19	3.37	0.45	0.68
Order of Accuracy	5.67	4.67	3.84	2.02

CPU time

Refining the grid can exponentially increase the time of calculation. It is therefore important to evaluate the time spent versus the results gained. From Figure 8.12a the actual time used for the calculations for the different grid refinements can be read to be 11 days for the extra fine grid, and 6 days for the fine grid, while the two coarsest grids used less than 10 hours. Figure 8.12b gives the CPU time in days for each grid refinement. 16 CPU's were used for all the calculations. This is the computational time for a fixed FPSO, when studying a floating case the motions of the vessel needs to be calculated, making the analysis more complex and the expected CPU time to increase.

The computational time is not necessarily linearly increasing with the number of cells as was the case for the calculations done with Wadam. If the CFL-number is exceeded the analysis can sometimes get "stuck" trying to fulfill all the requirements. This typically occurs if the grid refinement is not fine enough which may happen if the waves becomes, for instance, very steep or too short, or if the grid is too fine, causing numerical instabilities.

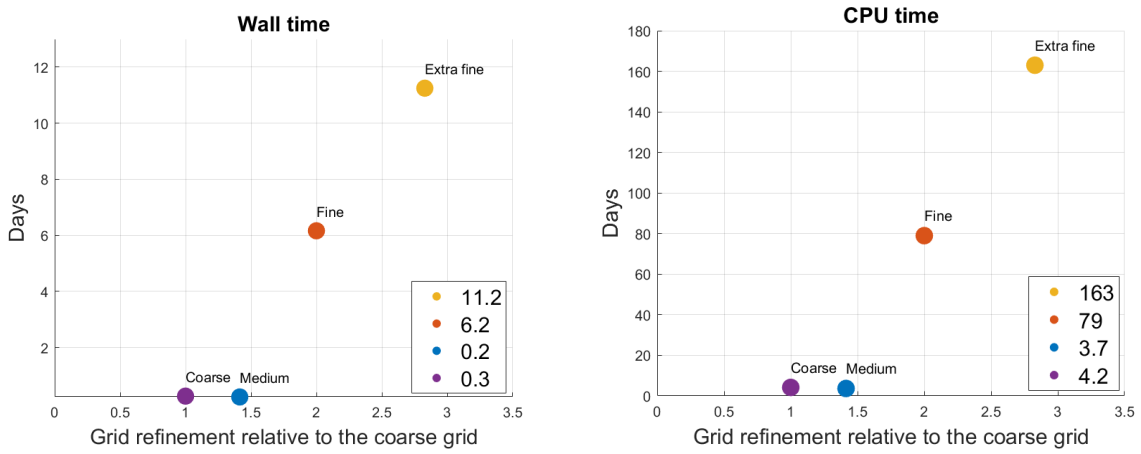

(a) Wall time.

(b) CPU time.

Figure 8.12: Deviation from the Wadam result for the amplitude for the convergence of the grid.

Based on Figure 8.10, Figure 8.11, Table 8.9 and Figure 8.12 the fine grid was chosen for further calculations. This grid takes significantly shorter time than the finest grid, and gives results that deviates less than 1% for the forces in z-direction, less than 5% for the amplitude, and less than 20% for the mean value for the force in x-direction. Considering the magnitude of the mean value in the x-direction a 20% deviation is not alarming.

8.2 Verification of the results

In addition to the forces from Wadam that were compared to the results from ComFLOW in the Section 8.1, other results from the Wadam analysis can also be used to compare and verify the results from ComFLOW. The following Section presents some aspects of the results from Wadam and ComFLOW.

8.2.1 Response

Results from Wadam were used to verify the results from ComFLOW. The results in Wadam are given on the form

$$Response = A \cdot cos(\omega \cdot t + \epsilon) \tag{8.2}$$

Where the *Response* is the surface elevation, force or motion, A is the amplitude of the response, ω is the wave frequency, t is time and ϵ is the phase.

8.2.2 Phase shift

Because of different coordinate systems in Wadam and ComFLOW, the results from Wadam were phase shifted to correspond to the coordinate system in ComFLOW. The coordinate system in Wadam was situated at the aft of the FPSO, while in ComFLOW, the origin was placed mid-ship. That gives a distance of 160 m between the coordinate systems. Equation (8.3) gives the expression for the phase shift of incident waves. The minus sign comes from the rotation of the axis in ComFLOW.

$$\epsilon = -(\epsilon_{Wadam} + \frac{distance\ between\ the\ coordinate\ systems - \lambda}{\lambda} \cdot 360°) \tag{8.3}$$

The waves, forces and motions had to be phase shifted. The pitch motion was 90° shifted and the surge motion was 180° off because the FPSO was rotated 180° in ComFLOW.

8.2.3 Estimated values

To evaluate the performance of the analysis it is important to have an idea of the order of magnitude of the forces to be calculated. The force in the z-direction was expected to oscillate around the value of the buoyancy force. From Wadam the buoyancy was found to be $3.30 \cdot 10^9$ N. Studying the plots in Section 8.1 it is clear that the buoyancy is close to the expected buoyancy from Wadam deviating with less than 1%.

Since only half the ship was simulated in ComFLOW, the force in y-direction had a mean value different from zero. A rough estimate of the mean value in the y-direction is given in Equation (8.4).

$$Fy = \frac{\rho \cdot g \cdot h \cdot A}{2} = \frac{1025kg/m^3 \cdot 9.81m/s^2 \cdot 20m \cdot 320m \cdot 20m}{2} = 6.44 \cdot 10^8\ N \qquad (8.4)$$

ρ is the water density, g is the gravitational acceleration, h is the draft, and A is an estimation of the area of the ship side. In appendix G.1 the forces for the different grid sizes of the domain is plotted. The values in y-direction oscillates between $6.67 \cdot 10^8$ and $6.75 \cdot 10^8$, which is about 4-5% off the estimated value in Equation (8.4).

Both the mean buoyancy and the mean value in z-direction are both higher for the results from ComFLOW than the results from Wadam. Nevertheless, the deviation is so small that it could originate from a small numerical error caused by for instance the grid refinement, the change in the wet surface or the water depth in the domain.

8.2.4 Surface elevation

In Appendix G the surface elevation from probe 2 in Figure 8.13, for a domain without a geometry, is plotted against the result from Wadam. The wave has a period of 10 s and an amplitude of 1 m. This was done to verify that the surface elevation had amplitudes and periods as expected. If a domain is too shallow, the waves can become affected by the sea bed. From the graph it can be observed that the periods and amplitudes are almost identical, but there are small discrepancies. The peaks deviate with an average of 3.36% from the expected amplitude of 1 m. This disparity is within the area of acceptance of 5%.

In Figure 8.14 the surface elevation in ComFLOW, from probe 1, is first plotted against

the incident waves from Wadam, and then against the superimposed waves consisting of the incident and diffracted waves. The results are for a fixed FPSO with an incident wave amplitude of 1 m and a period of 10 s. The results from Wadam were shifted according to Equation (8.3).

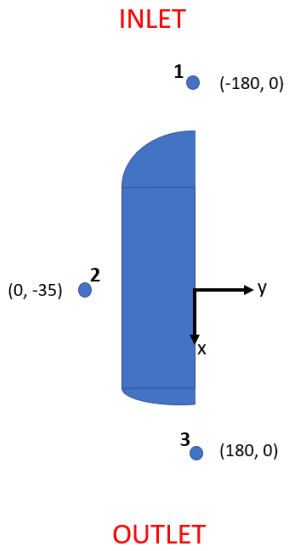

Figure 8.13: The locations of the wave probes.

The location of probe 1 is given in Figure 8.13. Probe 1 is relevant to study because it is placed close to the bow of the vessel. Hence, the waves at this location are expected to be diffracted back into the incoming waves. If the resulting waves become larger than the 10 m, which is the height of the freeboard of the model, water on deck can occur. That is not desirable because the model does not have any super structure, causing the calculated forces to include an extra error. The phenomenon of green water loading is not the target of this thesis but is a relevant topic when studying steep waves and extreme weather conditions.

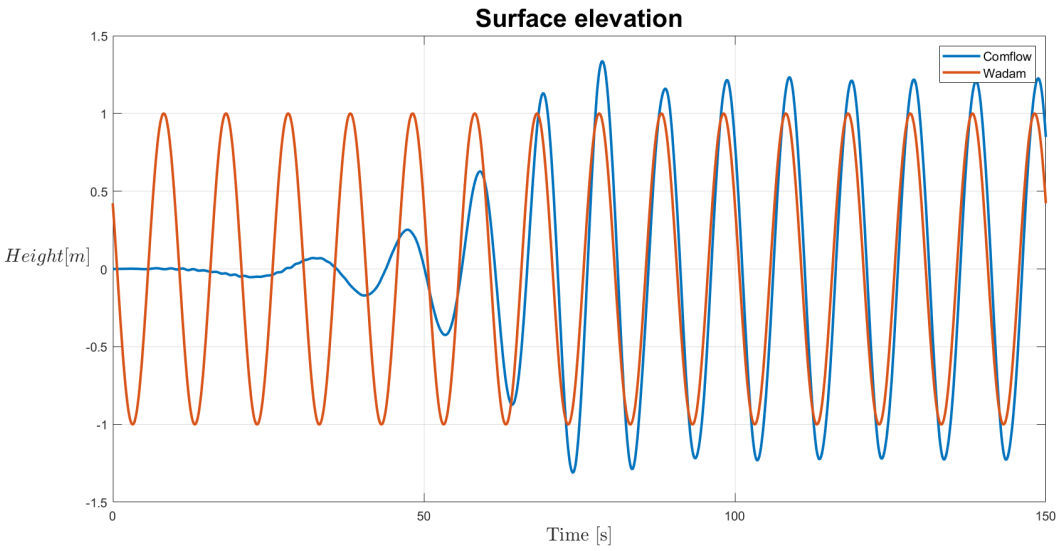

(a) Surface elevation from ComFLOW and the incident wave from Wadam.

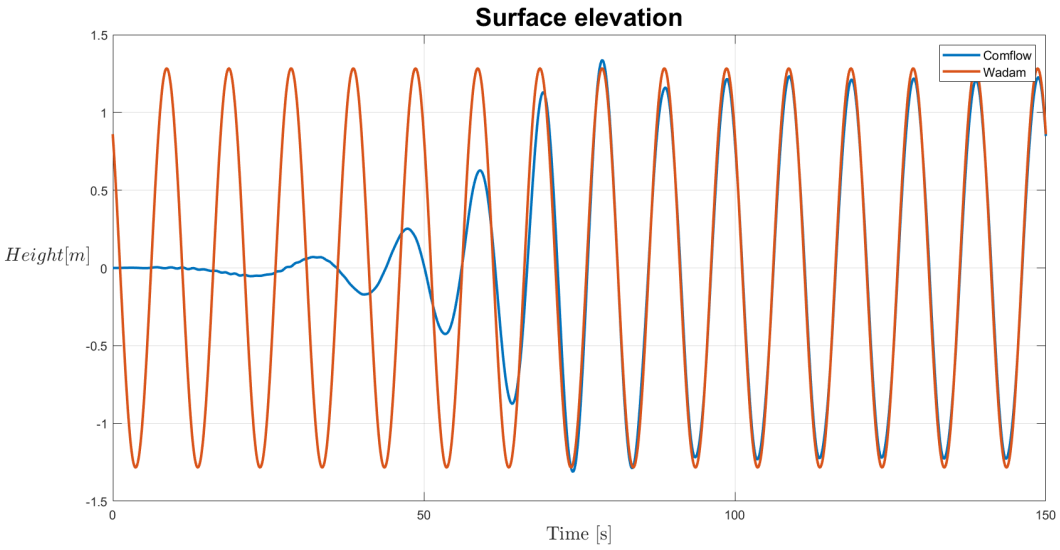

(b) Surface elevation from ComFLOW and the resulting wave consisting of the incident and diffracted wave from Wadam.

Figure 8.14: Surface elevation measured at wave probe 1.

From Figure 8.14a it is clear that the amplitudes from the wave probe in ComFLOW are larger than for the incident waves. The phase is also slightly shifted between the two results. When the diffracted waves are included in the result from Wadam, see Figure 8.14b, both the amplitudes and phase are almost identical for the results from ComFLOW and Wadam.

The superimposed wave from Wadam can be used to estimate the danger of water on

deck for a fixed FPSO, by estimating the total wave height in front of the bow of the ship. It is only the wave amplitude of 12.15 m that gives a total wave height higher than the freeboard of 10 m. The steepness of 90% of the maximum steepness is therefore not analyzed for the fixed FPSO. Nevertheless, the probe is 20 m ahead of the ship bow, the resulting wave can, therefore, be expected to be even larger closer to the ship. The wave amplitude of 9.45 m gives a total amplitude of 9.64 m at the wave probe 20 m in front of the bow, this amplitude should also be paid attention to regarding water on deck.

For a floating FPSO the relative vertical motion between the FPSO and the incident waves can be calculated to estimation if there is any danger of water on deck with Equation (8.5). The coordinate system in Wadam is located at the stern of the ship, and the pitch motion is relative to the center of buoyancy which is located close to the midship.

$$(S_3 - \zeta_0) = \eta_3 - \frac{L}{2}\eta_5 - \zeta_a cos(\omega t + kL) \tag{8.5}$$

S_3 is the vertical motion, η_3 is the heave motion, η_5 is the pitch motion, and L is the length of the ship. Investigating the amplitudes given in Table 8.1, the relative vertical motion is given in Table 8.10. The freeboard is 10 m, which means that according to the results from Wadam it is only the period of 11 s with an amplitude corresponding to a steepness of 90% that have a danger of water on deck according to Equation (8.5).

Table 8.10: Relative vertical motion between the incident waves an the FPSO for different wave periods and steepnesses.

	Relative vertical motion [m]			
Steepness [%] / Period [s]	10	50	70	90
4	0.17	0.86	1.19	1.53
8	0.69	3.40	4.76	6.12
11	1.31	6.54	9.15	11.77

8.3 Fixed FPSO

Based on the convergence study, the very large domain was used with a fine grid size and the geometry had a fine surface mesh. The periods analyzed are within the range of significant drift forces according to the results from Wadam. The analysis were done on Tyr for the periods given in Table 8.1 for the steepnesses up to 70% of maximum wave steepness. This is because the size of the freeboard was 10 m, hence to avoid water on deck, and the complexity it adds to the problem, a steepness of 70% of the maximum steepness was chosen.

Table 8.11 gives the mean drift force in the x-direction for the fixed FPSO for the three steepnesses 10%, 50% and 70% of the maximum steepness. In the following sections the plots of the force coefficients for the drift forces in x-direction for the given periods are presented and further discussed.

Table 8.11: Mean values for the force in x-direction for a fixed FPSO. The gray cells indicate not presentable values because the resolution of the results are too poor.

	Steepness [%]					
Period [s]	10		50		70	
4						
8	$3.98 \cdot 10^4 N$	0.73	$5.26 \cdot 10^5 N$	0.39	$9.64 \cdot 10^5 N$	0.36
11	$1.54 \cdot 10^5 N$	0.80	$3.43 \cdot 10^6 N$	0.71	$7.07 \cdot 10^6 N$	0.75

8.3.1 Results for 4 s wave period

Figure 8.15 shows the force in the x-direction for the three steepnesses 10%, 50% and 70%. As observed from the plot, the forces are irregular and pointy. One of the reason for this could be the grid refinement. A wave period of 4 s gives a wave length of about 23 m. As described in Section 3.7.1 the recommended minimum number of cells per wave length is 60 cells. As each of the finest cells have a length of 0.94 m, see Table 8.8, the total number of cells becomes just over 24 cells for the wave length. The height of the cells are 0.67 m. This gives only about two cells in the wave height. Concluding, the grid is too coarse. Since the convergence test was done for a wave with a period of 10 s it is not surprising that the grid could turn out too coarse.

Another reason for the messy results could be the way ComFLOW describes the surface and the interaction between the fluid and the geometry. As described in Section 3.8, the grid is staggered meaning that the geometry and surface cuts the cells. This handling of the surface and the geometry can lead to inaccuracies in the calculation of pressure if the grid is too coarse. The force in the x-direction highly depends on the surface of the bow. The geometry with the bulb, used in this analysis, is curvy and could be difficult for the grid to capture. Hence, no mean drift is extracted from this plot, and the cells are marked with gray in Table 8.11.

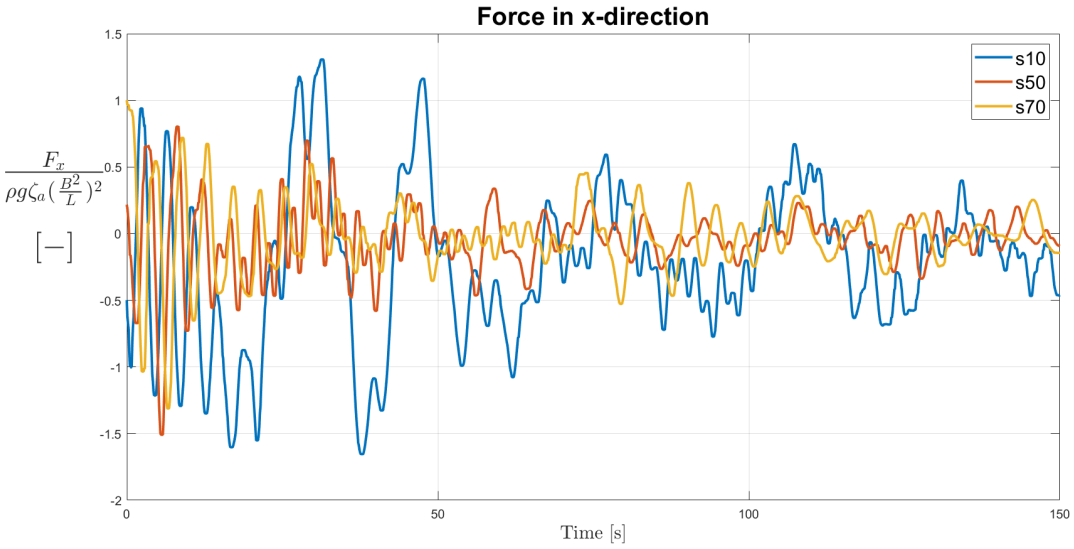

Figure 8.15: Force in x-direction for a fixed FPSO with bulb for a wave period of 4 s and amplitudes corresponding to 10%, 50% and 70% of the maximum steepness, $s_{max} = \frac{H}{\lambda} = \frac{1}{7}$.

8.3.2 Results for 8 s wave period

Figure 8.16 present the force in x-direction. The force for the steepness of 50% and 70% of the maximum steepness are higher than the 10% steepness for the first part, then they decrease and flattens out. In the first 50 s a transient phase is expected, nonetheless, notable that the lowest steepness has the relative largest force amplitudes.

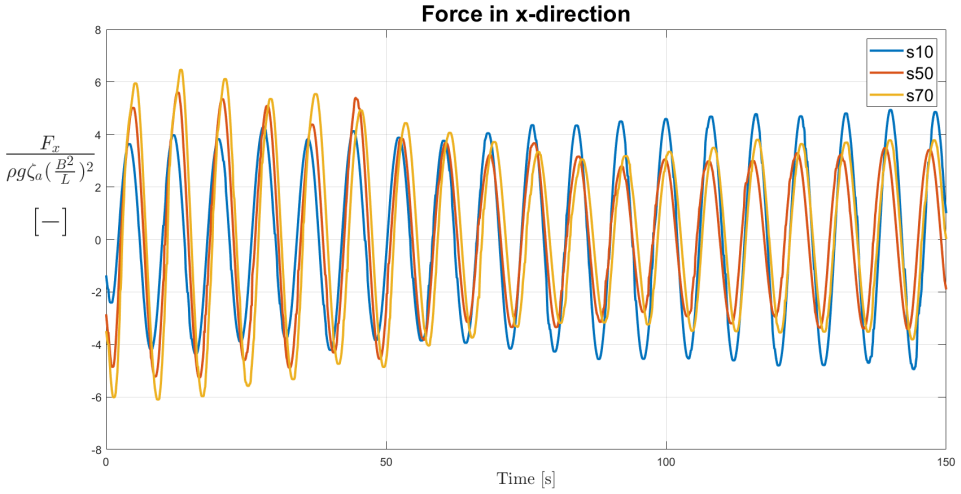

Figure 8.16: Force in x-direction for a fixed FPSO with bulb for a wave period of 8 s and amplitudes corresponding to 10%, 50% and 70% of the maximum steepness, $s_{max} = \frac{H}{\lambda} = \frac{1}{7}$.

In Table 8.12 the mean drift force in the x-direction for the results from Wadam and ComFLOW is presented both with and without units, and the deviation from Wadam for the ComFLOW results are given in percent. The sign is positive if the results from ComFLOW are higher, and negative if the results are lower. Studying the results from Table 8.12 shows that ComFLOW provides lower mean drift forces than Wadam, and that the discrepancy between the tools increases with increasing steepness.

Table 8.12: Mean drift force in surge for a fixed FPSO with bulb given in N and non-dimensional with respect to $\rho g \zeta_a^2 (\frac{B^2}{L})$ and the deviation from Wadam given in percent with T=8 s.

	Mean drift force in surge				
Steepness [%]	Wadam		ComFLOW		Deviation from Wadam
10	$5.00 \cdot 10^4 N$	0.91	$3.98 \cdot 10^4 N$	0.73	-20%
50	$1.23 \cdot 10^6 N$	0.91	$5.26 \cdot 10^5 N$	0.39	-57%
70	$2.41 \cdot 10^6 N$	0.91	$9.64 \cdot 10^5 N$	0.36	-60%

8.3.3 Results for 11 s wave period

The results with 11 s period and the steepnesses of 10%, 50% and 70% for the fixed geometry with bow is presented in Figure 8.17. This graph shows that the results are relatively similar independently of the steepness. The plots are more even than the results for the 4 s wave period. Assuming that the main issue was the refinement of the grid for the period of 4 s, a wave period of 11 s gives a wave length of 189 m, which means that there are 201 cells per wave length. This is over three times the recommended number. The steepness of 10% has only four cells in the wave height, but for the higher steepnesses the number of cells exceeds 20 cells. The high resolution in these results supports the assumption that a too coarse grid resulted in the unexpected results for the 4 s wave period.

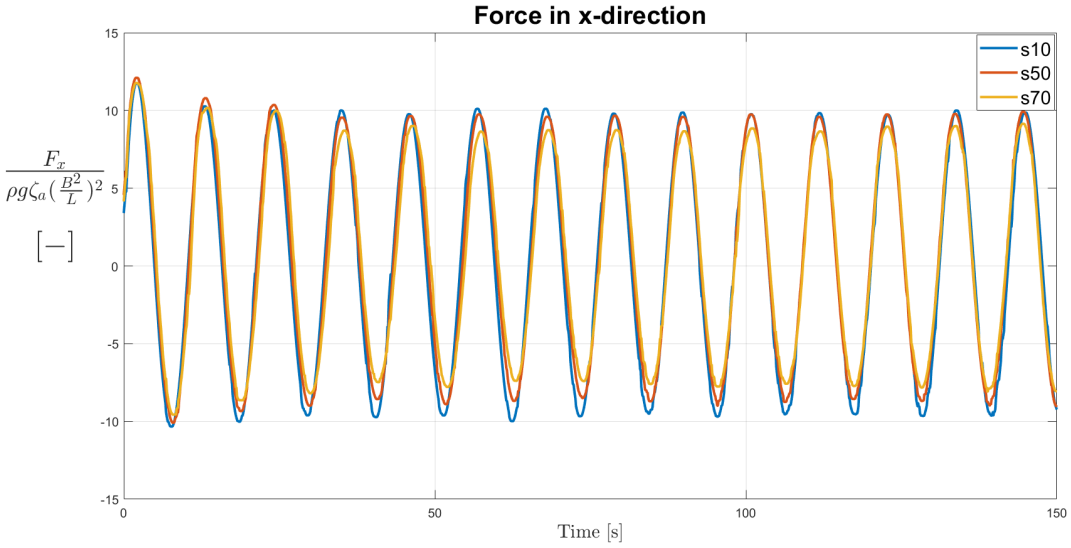

Figure 8.17: Force in x-direction for a fixed FPSO with bulb for a wave period of 11 s and amplitudes corresponding to 10%, 50% and 70% of the maximum steepness, $s_{max} = \frac{H}{\lambda} = \frac{1}{7}$.

From the results for the mean drift force in surge given in Table 8.13, the results are, as for the results in for the wave period of 8 s, lower for the mean drift forces from ComFLOW. The discrepancy is also increasing with the wave steepness for this wave period. Nonetheless, the deviations for the mean drift force in the x-direction for the different steepnesses are smaller for the wave period of 11 s than the wave period of 8 s.

Table 8.13: Mean drift force in surge for a fixed FPSO with bulb given in N and non-dimensional with respect to $\rho g \zeta_a^2 (\frac{B^2}{L})$ and the deviation from Wadam given in percent with T=11 s.

	Mean drift force in surge				
Steepness [%]	Wadam		ComFLOW		Deviation from Wadam
10	$1.61 \cdot 10^5 N$	0.83	$1.54 \cdot 10^5 N$	0.80	-4%
50	$4.00 \cdot 10^6 N$	0.83	$3.43 \cdot 10^6 N$	0.71	-15%
70	$7.84 \cdot 10^6 N$	0.83	$7.07 \cdot 10^6 N$	0.75	-10%

8.4 Floating FPSO

In the analysis of the floating FPSO, the extra large domain was used with the extra fine surface mesh on the geometry and the fine grid in the domain. The domain was made slightly higher to enable to run the highest waves without the FPSO exiting the domain. The analysis were done on Saga for the periods and wave steepnesses given in Table 8.1. The FPSO was fixed in all degrees of freedom except heave and pitch.

Table 8.14 gives an overview of the mean drift forces for the steepnesses of 10%, 50%, 70% and 90% of the maximum steepness. The following sections will further present and discuss the results.

Table 8.14: Mean values for the force in x-direction for a floating FPSO. The gray cells indicate not presentable values because the resolution of the results are too poor, or the analysis did not finish in time.

	Steepness [%]							
Periods $[s]$	10		50		70		90	
4								
8	$-1.69 \cdot 10^5 N$	-3.08	$3.30 \cdot 10^4 N$	0.02	$3.78 \cdot 10^5 N$	0.14	$8.67 \cdot 10^5 N$	0.20
11	$5.48 \cdot 10^5 N$	2.85	$5.57 \cdot 10^6 N$	1.16				

8.4.1 Results for 4 s wave period

Figure 8.18 shows the forces in the x-direction and Figure 8.19 the motions in heave and pitch for the floating FPSO with a wave period of 4 s. The analysis with a steepness of 90% of maximum wave steepness was not able to run because the wave was too steep and short, so ComFLOW was not even able to start the analysis. To run this wave a finer grid is most likely needed. A 90% steepness is very close to the breaking wave criteria and can due to the diffracted waves from the FPSO the waves can break. Breaking waves are much more complicated numerically.

As can be observed from the Figure 8.18, the forces are not periodic and the graph is spiky. The wave with the steepness of 50% and 70% of the maximum steepness are more consistent than the 10% steepness, the cause could be that there are more cells in the wave height for the higher steepnesses than for the lowest one. The forces are relatively higher for the lowest wave steepness, which was also the trend for all the fixed FPSO's.

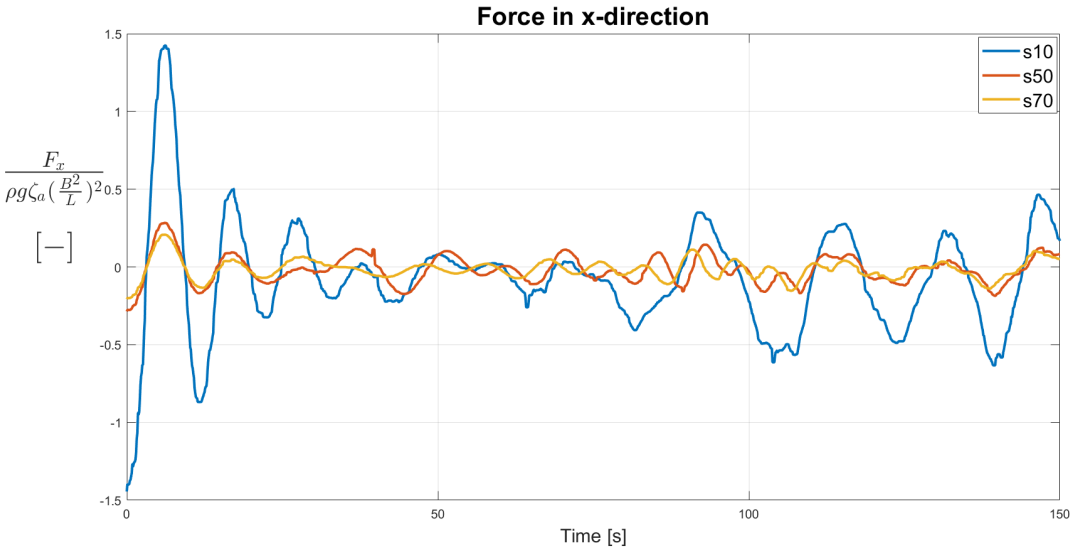

Figure 8.18: The force in x-direction for a floating FPSO with bulb for a wave period of 4 s and amplitudes corresponding to 10%, 50% and 70% of the maximum steepness, $s_{max} = \frac{H}{\lambda} = \frac{1}{7}$

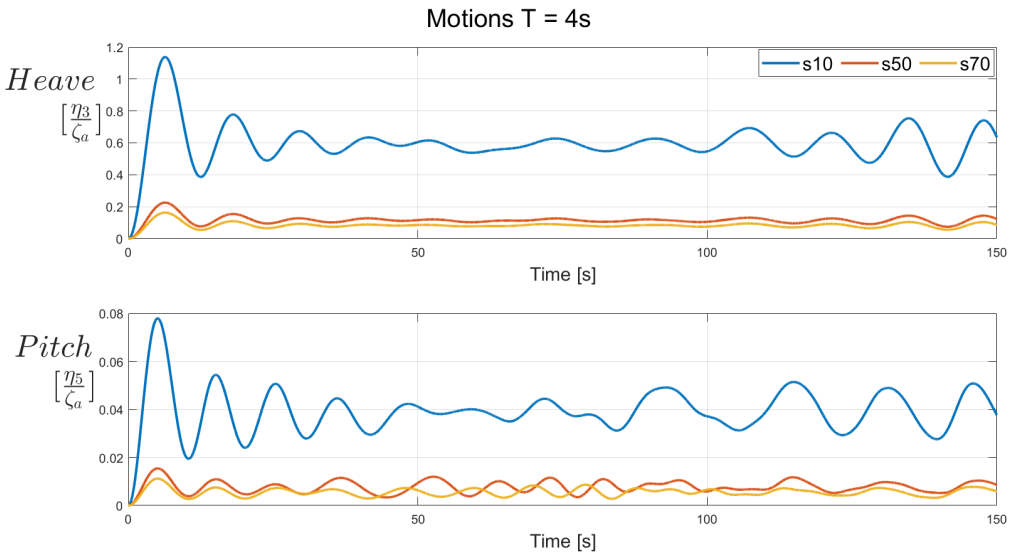

Figure 8.19: The motion for a floating FPSO with bulb for a wave period of 4 s and amplitudes corresponding to 10%, 50% and 70% of the maximum steepness, $s_{max} = \frac{H}{\lambda} = \frac{1}{7}$, in heave and pitch divided by the wave amplitude

Figure 8.19 demonstrates significantly higher amplitudes of the motions in heave and pitch for the lowest steepness. Studying the plots, the steepness of 10% is floating differently with a constant angle of pitch. A significant offset is observed at the beginning of the time series giving the FPSO a transient phase. This is most prominently for the wave steepness of 10% of the maximum steepness. From the convergence test in Section 8.1 the forces in z-direction had a higher mean value than the buoyancy from Wadam. This could indicate that the draft is slightly to large, causing the vessel to stabilize during the first time in the analysis.

If it is the offset of the draft that causes the discrepancy, the response multiplied with the incident wave amplitude should give the same values for all steepnesses. Multiplying the mean values for RAO's in heave with the different amplitudes corresponding to the steepnesses, all the motions shows an offset of about 0.11 m, see Table 8.15.

Table 8.15: Mean offset in heave.

Steepness [%]	η_3 $[m]$
10	$0.604 \cdot 0.18 = 0.109$
50	$0.117 \cdot 0.90 = 0.105$
70	$0.084 \cdot 1.25 = 0.105$

0.11 m reduction in the draft corresponds roughly to $2.05 \cdot 10^7 N$, estimated in Equation (8.6). In Figure 8.9b the mean value of the force in z-direction from ComFLOW is $3.325 \cdot 10^9$. Subtracting the estimation of the force caused by the offset of the draft, the new buoyancy becomes $3.325 \cdot 10^9 N - 2.05 \cdot 10^7 N = 3.305 \cdot 10^9 N$, which is the exact buoyancy given by Wadam. Despite that the geometries were given the same draft as the input in ComFLOW and Wadam, the draft did turn out the same. One reason could be the difference in the mesh size of the geometry, which in Wadam is 2 m and in ComFLOW is about 7 m. Considering that the force in z-direction were reduced with $9.5 \cdot 10^6 N$ in Figure 8.6b by refining the mesh from a target value of 20 m to 7 m, it is not unlikely that having the same mesh size would solve the difference in the buoyancy.

$$0.11m \cdot 320m \cdot 58m \cdot 1025\frac{kg}{m^3} \cdot 9.81\frac{m}{s^2} = 2.05 \cdot 10^7 N \tag{8.6}$$

The motions becomes larger again around 120 s. The reason for this could be that the transient phase has died out and the vessel starts to move with the waves.

8.4.2 Results for 8 s wave period

Figure 8.20 shows the forces in the x-direction and Figure 8.21 the motions in heave and pitch for the floating FPSO with a wave period of 8 s for the steepnesses 10%, 50%, 70% and 90% of the maximum steepness.

The amplitude of the forces in Figure 8.20 are not stabilizing before about 110 s into the analysis. This also accounts for the synchronizing of the phase for the different steepnesses. After 110 s the forces stabilizes and the steepness of 10% of the maximum wave steepness stands out at the steepness that causes the relative highest forces in surge.

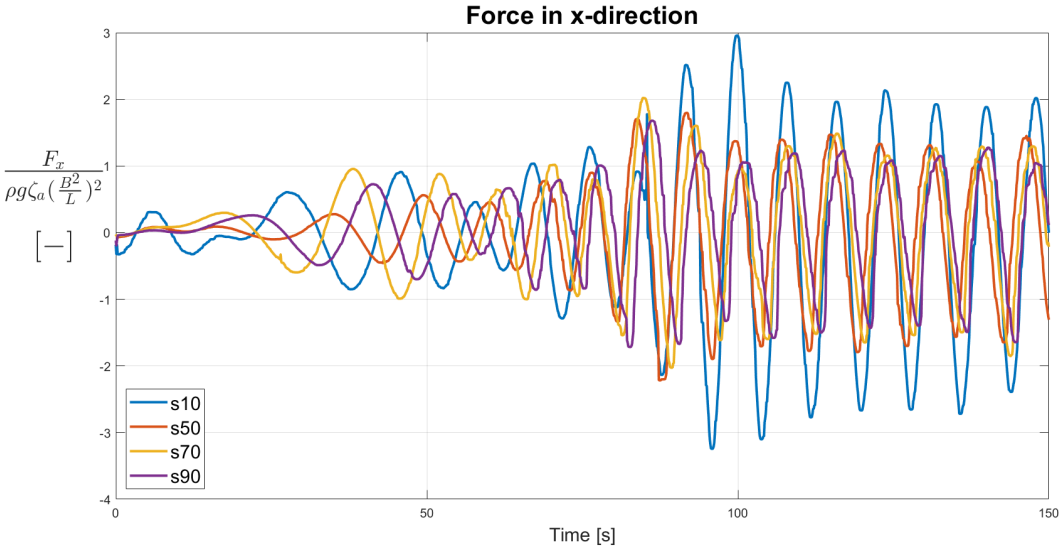

Figure 8.20: The force in the x-direction for a floating FPSO with bulb for a wave period of 8 s and amplitudes corresponding to 10%, 50%, 70% and 90% of the maximum steepness, $s_{max} = \frac{H}{\lambda} = \frac{1}{7}$.

Figure 8.21 gives the motions in heave and pitch for the four steepnesses together with the motions from Wadam. Studying both the heave and the pitch motions, the phases are not fully synchronized, but they are close to the result from Wadam. The offset in the heave motion is also visible for the period of 8 s and is assumed to have the same origin as in Section 8.4.1. Studying the plot for the pitch motions the steepness of 10% of the maximum steepness does not have the same constant pitch different than zero, as was the case in Figure 8.19. The reason for this inconsistency is not clear at this point.

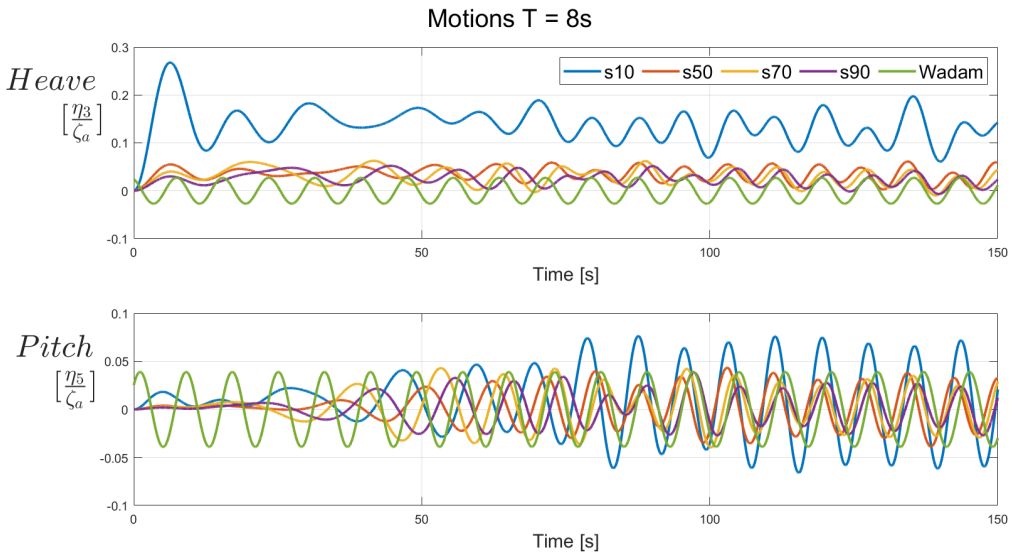

Figure 8.21: The motion for a floating FPSO with bulb for a wave period of 8 s and amplitudes corresponding to 10%, 50%, 70% and 90% of the maximum steepness, $s_{max} = \frac{H}{\lambda} = \frac{1}{7}$, in heave and pitch divided by the wave amplitude.

Higher relative motions between the vessel and the fluid should cause higher mean drift forces according to the theory. Considering the motions in Figure 8.21 the steepness of 10% of the maximum steepness has the largest relative motions, but given the results in Table 8.16 it does not result in the relative highest mean drift loads, rather the opposite. ComFLOW underpredicts the mean drift forces compared to Wadam, and the deviations from Wadam are very large but decreasing with increasing wave steepness. This evolution is the opposite as observed for the fixed FPSO with a period of 8 s.

Table 8.16: Mean drift force in surge for a floating FPSO with bulb given in N and non-dimensional with respect to $\rho g \zeta_a^2 (\frac{B^2}{L})$ and the deviation from Wadam given in percent with T=8 s.

	Mean drift force in surge				
Steepness [%]	Wadam		ComFLOW		Deviation from Wadam
10	$6.14 \cdot 10^4 N$	1.12	$-1.69 \cdot 10^5 N$	-3.08	-375%
50	$1.51 \cdot 10^6 N$	1.12	$3.30 \cdot 10^4 N$	0.02	-98%
70	$2.97 \cdot 10^6 N$	1.12	$3.78 \cdot 10^5 N$	0.14	-88%
90	$4.90 \cdot 10^6 N$	1.12	$8.67 \cdot 10^5 N$	0.20	-82%

8.4.3 Results for 11 s wave period

Figure 8.22 presents the forces in the x-direction and Figure 8.23 the motions in heave and pitch for the floating FPSO with a wave period of 11 s for the steepnesses 10%, 50%, 70% and 90% of the maximum steepness. Due to limited time the analysis for the steepness of 70% and 90% of the maximum steepness did not finish in time, but are plotted as far as they came.

Observing Figure 8.22 the forces develops very synchronized and gradual. Within the 150 s of analysis it is difficult to decide if the periods are stationary or still evolving. A larger time frame would have been beneficial.

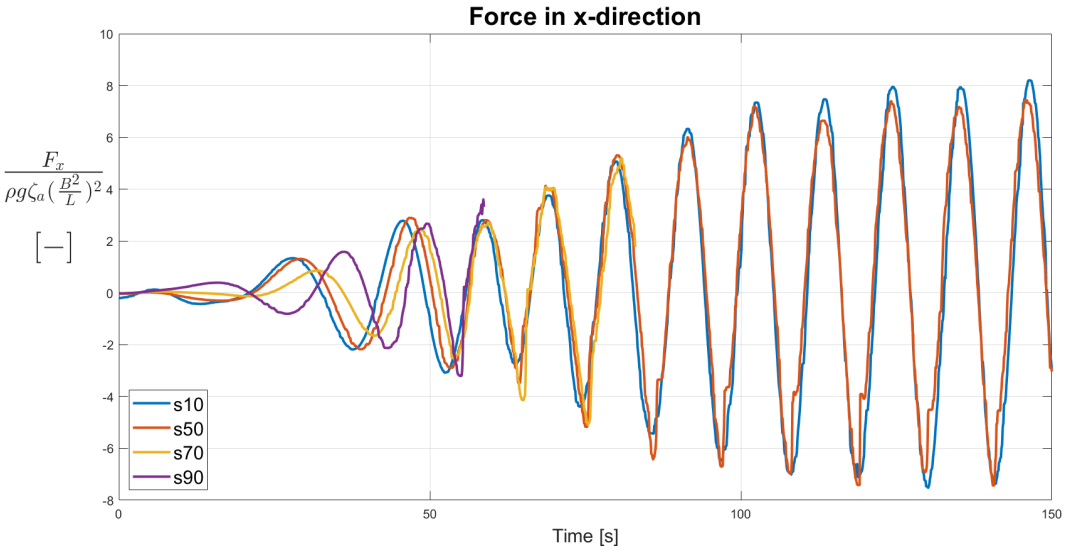

Figure 8.22: The force in the x-direction for a floating FPSO with bulb for a wave period of 11 s and amplitudes corresponding to 10%, 50%, 70% and 90% of the maximum steepness, $s_{max} = \frac{H}{\lambda} = \frac{1}{7}$.

Compared to the motions for the periods of 4 s, in Figure 8.19, and 8 s, in Figure 8.21, the motions for the period of 11 s, in Figure 8.23, are very close to the solution from Wadam both in phase and amplitude. The steady offset of the heave motion and the large initial motions clearly observed for the period of 4 s is still present in Figure 8.23. As the relative motions are larger for the wave period of 11 s because of the higher amplitudes corresponding to the steepnesses, the offset and large initial motion are relatively smaller than in the case for the period of 4 s.

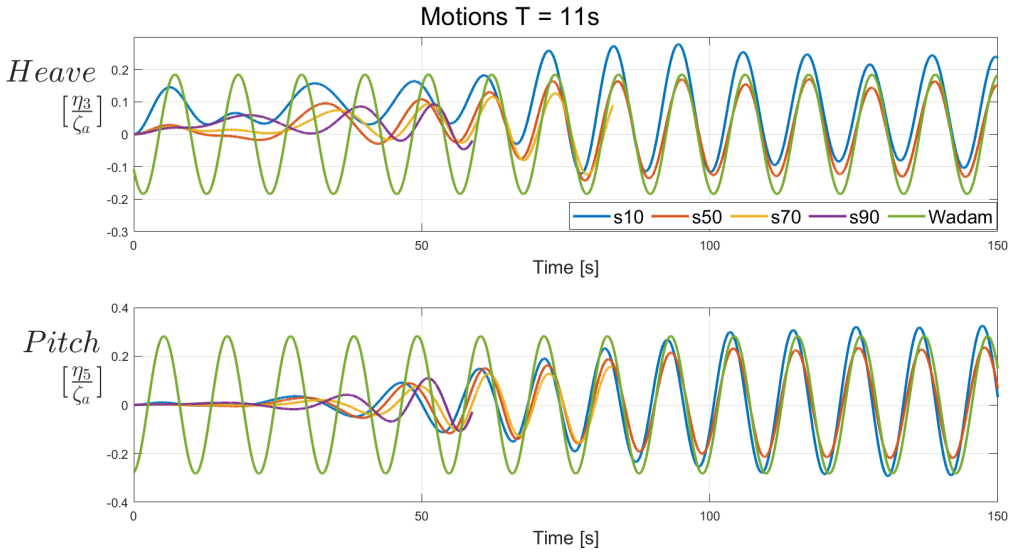

Figure 8.23: The motion for a floating FPSO with bulb for a wave period of 11 s and amplitudes corresponding to 10%, 50%, 70% and 90% of the maximum steepness, $s_{max} = \frac{H}{\lambda} = \frac{1}{7}$, in heave and pitch divided by the wave amplitude.

Table 8.17 presents the mean drift force in surge for the wave steepness of 10% and 50% of the maximum steepness. The steepness of 10% of the maximum wave steepness gives much larger mean drift forces than the result from Wadam.

Table 8.17: Mean drift force in surge for a floating FPSO with bulb given in N and non-dimensional with respect to $\rho g \zeta_a^2 (\frac{B^2}{L})$ and the deviation from Wadam given in percent with T=11 s. The gray cells indicate analysis that did not finish in time.

	Mean drift force in surge				
Steepness [%]	Wadam		ComFLOW		Deviation from Wadam
10	$2.49 \cdot 10^5 N$	1.29	$5.48 \cdot 10^5 N$	2.85	121%
50	$6.21 \cdot 10^6 N$	1.29	$5.57 \cdot 10^6 N$	1.16	-10%
70	$1.22 \cdot 10^7 N$	1.29			
90	$2.01 \cdot 10^7 N$	1.29			

8.5 CPU time

The wall time and the CPU time is given in days for the different percentages of the maximum wave steepness in Figure 8.24. Since the analysis for the 50% and 70% of maximum wave steepness for the period of 11 s did not finish in time they were not included in the plots. The color orange indicates the floating analysis, while the blue are the fixed ones. The different steepnesses are presented with different lines. 16 CPU's were used for all the calculations on Saga and Tyr.

The fixed analysis used from half a week to one week to finish. The floating FPSO's used from one to three weeks to complete 150 s of analysis, and this is when the two longest analysis are not accounted included. From Figure 8.24b there is a trend that longer waves, larger amplitudes and steeper waves gives longer computational time.

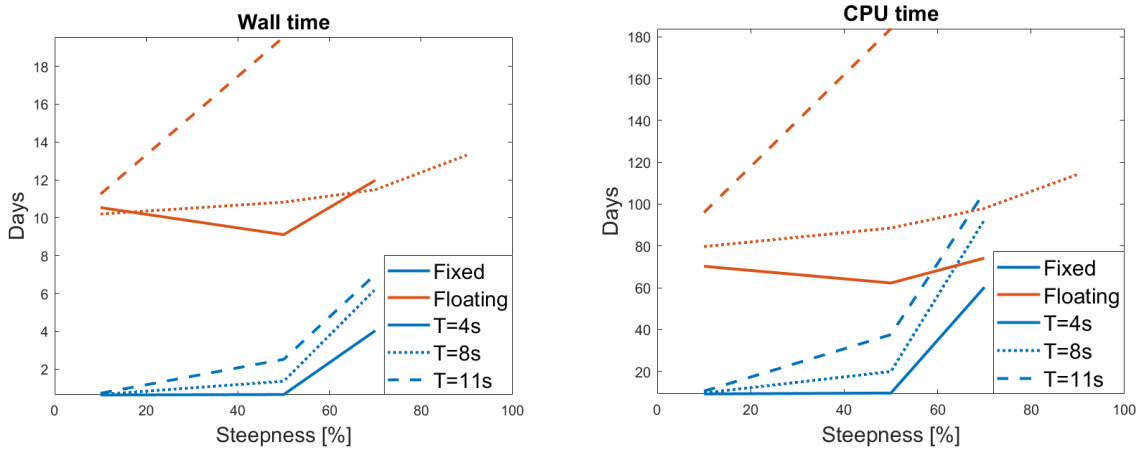

(a) Wall time. **(b)** CPU time.

Figure 8.24: Wall time and CPU time given in days for the percentage of the maximum steepness, $s_{max} = \frac{H}{\lambda} = \frac{1}{7}$.

The motions were fixed in all directions except for heave and pitch for the floating analysis. If a mooring system with realistic surge motions were to be investigated, even longer analysis were to be expected because an additional degree of freedom will have to be calculated.

8.6 Different bows

The three different bows presented in Figure 5.2 are analysed with ComFLOW subjected to waves with a period of 11 s and amplitude corresponding to a steepness of 10% of maximum steepness.

8.6.1 Fixed FPSO

The forces in the x-direction for the geometry with and without bulb and the wall sided geometry are plotted in Figure 8.25. The wall sided has less draft as described in Section 7.3. As expected from the Wadam results, the wall sided geometry has larger forces in surge than the geometries with and without bulb.

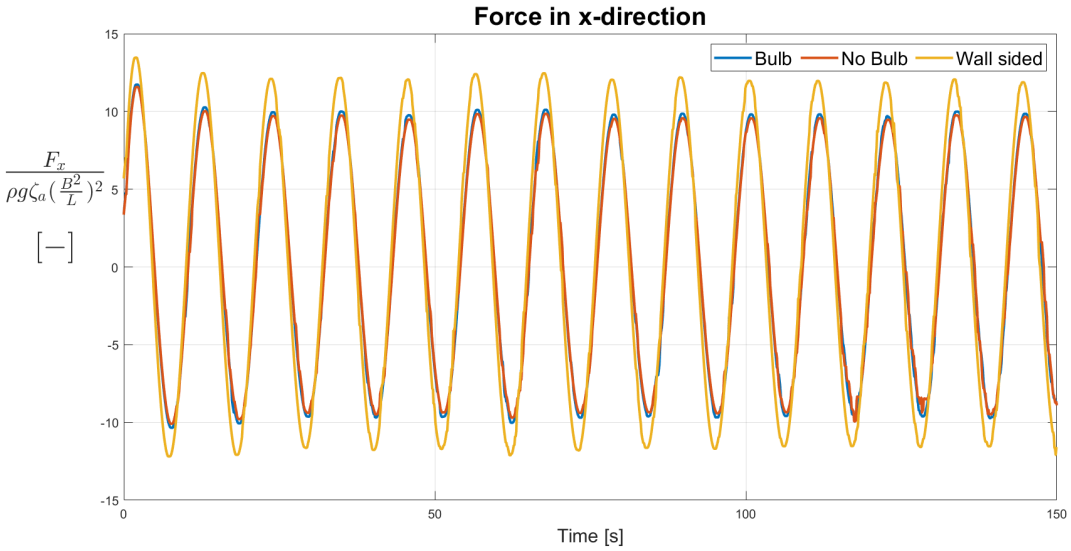

Figure 8.25: Force in x-direction for the three bow geometries for a fixed FPSO for a wave period of 11 s and ζ_a=1.35m

Seen from Table 8.18, the mean values for the drift forces in surge corresponds well with the results from Wadam. The detected drift forces in ComFLOW are all larger than the Wadam results.

Table 8.18: Mean drift force in surge for the three fixed geometries with T=11s and ζ_a=1.35m given in N and non-dimensional with respect to $\rho g \zeta_a^2(\frac{B^2}{L})$ and the deviation from Wadam given in percent.

	Mean drift force in surge				
Geometries	Wadam		ComFLOW		Deviation from Wadam
Bulb	$1.6 \cdot 10^5 N$	0.83	$1.68 \cdot 10^5 N$	0.87	5%
No bulb	$1.56 \cdot 10^5 N$	0.80	$1.60 \cdot 10^5 N$	0.83	4%
Wall sided	$1.86 \cdot 10^5 N$	0.96	$2.15 \cdot 10^5 N$	1.12	17%

8.6.2 Floating FPSO

The forces in x-direction for the floating FPSO with the three different bow shapes are given in Figure 8.26, and the heave and pitch motions are given in Figure 8.27. The forces are observed to be almost identical for all the geometries. A clear transient phase is observed at the two first periods for the wall sided geometry, while the following periods looks constant.

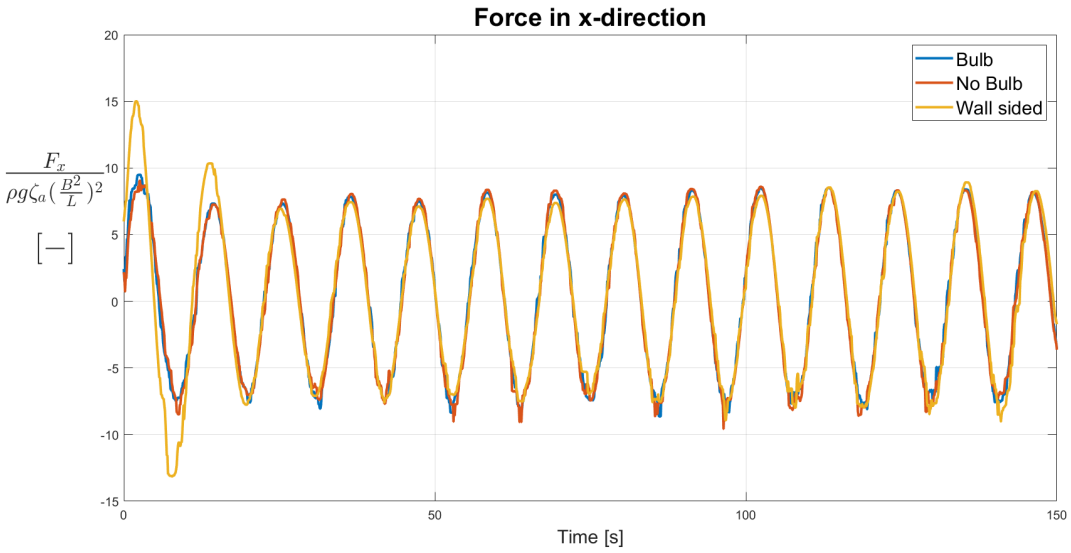

Figure 8.26: Force in x-direction for the three different bow geometries for a wave period of 11 s and ζ_a=1.35m.

Figure 8.27 presents the motion of the three vessels in heave and pitch. The geometry with and without bow moves similar, while the wall sided FPSO floats with a constant trim because of the volume at the bow. The COG should have been moved to keep the vessel at even keel.

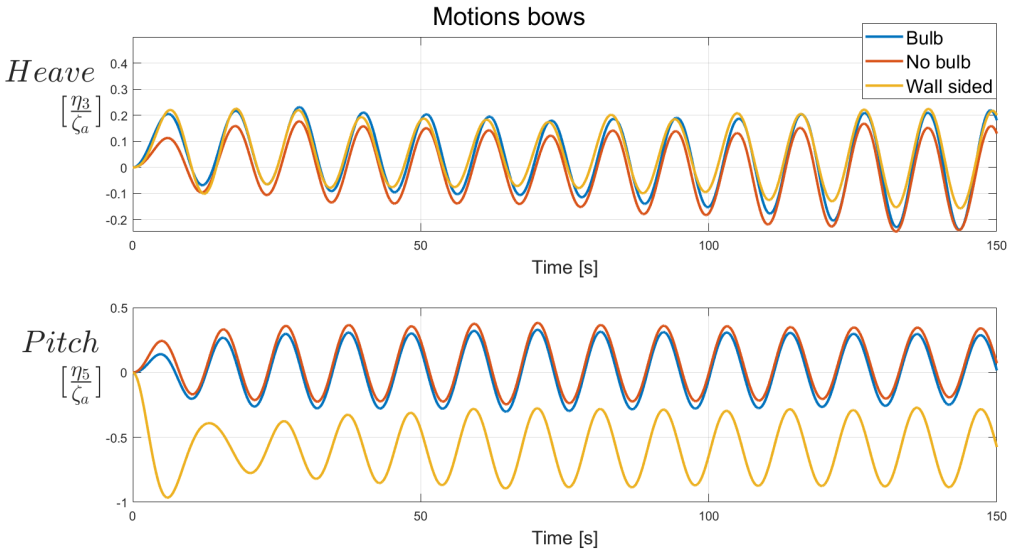

Figure 8.27: Heave and pitch motion for the three different bow geometries for a wave period of 11 s and ζ_a=1.35m.

The motion in heave has an amplitude of around 0.2 m. From Figure 7.6b from Wadam the expected motion in heave for a period of 11 s is around 0.18 m/ζ_a for all the bows. The amplitude is 1.35 m, giving an expected heave motion of 0.24 m. The amplitude in ComFLOW is 0.18 m for the wall sided geometry, 0.19 for the vessel without bulb, and 0.2 m for the geometry with bulb, which is not so far off. Table 8.19 gives the amplitude of the pitch motion from Wadam and ComFLOW and the deviation from Wadam in percent. As can be observed from Figure 8.27, the motions for the geometry with and without bulb are almost identical, just as expected from the Wadam results. The motions are in general smaller for the results from ComFLOW than the Wadam results.

Table 8.19: Amplitude of the pitch motion in degrees for the three different bow geometries at T = 11s and ζ_a=1.35m and the deviation from ComFLOW given in percent.

Geometries	Wadam	ComFLOW	Deviation from Wadam
Bulb	0.38°	0.32°	-16%
No bulb	0.39°	0.33°	-16%
Wall sided	0.28°	0.25°	-11%

Despite the fact that the geometry with and without bulb appears almost identical both considering the force in the x-direction and the motions, the mean drift load in surge is

so sensitive that the drift load is more than 50% larger for the geometry with bulb. The mean drift forces from ComFLOW are in general larger than the mean drift forces from Wadam.

Table 8.20: Mean drift force in surge for the three floating geometries with T=11s and ζ_a=1.35m given in N and non-dimensional with respect to $\rho g \zeta_a^2 (\frac{B^2}{L})$ and the deviation from Wadam given in percent.

	Mean drift force in surge				
Geometries	Wadam		ComFLOW		Deviation from Wadam
Bulb	$2.49 \cdot 10^5 N$	1.29	$5.24 \cdot 10^5 N$	2.72	111%
No bulb	$2.33 \cdot 10^5 N$	1.21	$3.42 \cdot 10^5 N$	1.78	47%
Wall sided	$2.65 \cdot 10^5 N$	1.38	$4.25 \cdot 10^5 N$	2.21	60%

Chapter 9

Conclusion and recommendations

9.1 Conclusion

The over all objective of the master thesis was to investigate the importance of nonlinear wave-body interaction effects on the FPSO drift loads, focusing on the mean drift load in surge. Nonlinear results from ComFLOW were compared to the outcome of the linear potential solver Wadam.

The linear results from Wadam showed that the wall sided geometry diffracts more waves for the lower wave periods, causing a higher mean drift force in surge than the geometry with and without bulb. The conservation of fluid momentum was proved to be a more robust theory than the direct pressure integration, which was more sensitive to geometrical inconsistencies.

The results from ComFLOW indicated that the grid was to coarse for the lowest selected wave period of 4 s to get any useful results. The deviations from Wadam were not consistent, ComFLOW detected smaller mean drift forces than Wadam for both the fixed and floating cases, but for the analyses related to the three bow geometries ComFLOW gave higher mean drift forces both for the floating and the fixed FPSO. The mean value of the force in surge was in general ten to hundred times smaller than the force amplitude, causing the value to be highly sensitive to the resolution of the result and the chosen stationary time interval.

It took up to three weeks to calculate the floating FPSO using 16 CPU's on the supercomputer Saga. Considering the findings in this master thesis and the calculation time spent, ComFLOW needs further validation on the topic of mean drift loads.

9.2 Recommendation for further work

The topic of calculating nonlinear forces is highly relevant. To further develop the model there are several actions that can be made both to improve the model and the post processing of the analysis. Following is a list of suggestions to be further investigated.

- A mooring line system with realistic natural periods in surge should be modeled to study its effect on the drift forces. This was a part of step four in the list of tasks, but the time was simply a insufficient resource.
- It would be beneficial to study the flow around the vessel to complement the knowledge to better explain the output from the analysis.
- The grid should be refined either by increasing the number of cells in each direction or by adding sub grids, or better, a combination, to capture also the short and steep waves. A convergence study should also be done for the shortest wave periods to assure sufficient grid refinement.
- A beach or some other boundary condition should be implemented at the lateral boundary to reduce the reflection and, hence, the domain size. This will reduce the computational time.
- The superstructure should be modeled to enable the study of green water loading.
- Since current significantly effects the drift loads, it had better be implemented.
- It would be beneficial to study the problem in irregular sea for more realistic wave conditions.
- Conduct the research with another CFD tool like Open FOAM or Star CCM+ which handles the grid set up differently to validate if it is a general challenge for the CFD to calculate the mean drift forces or if ComFLOW should be further developed.

Bibliography

Avila, L., Osterdahl, K., McKenzie, S., & Jordan, S. (2020). The ParaView Guide - Community Edition. Kitware Inc.

Bashforth, F., & Adams, J. (1883). *An attempt to test the theories of capillary action: By comparing the theoretical and measured forms of drops of fluid.* Cambridge University Press.

Bøckmann, A. (2016). Exwave JIP - report.

Buchner, B. (1996). The Influence of the Bow Shape of FPSOS on Drift Forces and Green Water. Offshore technology conference.

Buffoni, B., & Toland, J. (2003). *Analytic Theory of Global Bifurcation : An Introduction.* Princeton University Press.

Butcher, J. (1999). Numerical methods for ordinary differential equations in the 20th century. doi:10.1016/S0377-0427(00)00455-6

BW Offshore. (2018). BW ADOLO. Retrieved March 11, 2019, from bwoffshore.com/business/fleet-map/azurite/

Colicchio, G., Greco, M., & Faltinsen, O. M. (2007). A BEM-level set domain-decomposition strategy for non-linear and fragmented interfacial flows. INTERNATIONAL JOURNAL FOR NUMERICAL METHODS IN ENGINEERING.

DNV GL. (2015). DNVGL-OS-E301 - Position mooring.

DNV GL. (2017). SESAM USER MANUAL - Hydro-D.

DNV GL. (2018). GeniE - User documentation.

DNV GL. (2019a). DNVGL-RP-C205 - Environmental conditions and environmental loads.

DNV GL. (2019b). SESAM USER MANUAL - POSTRESP.

DNV GL. (2019c). SESAM USER MANUAL - WADAM.

Düz, B., Borsboom, M., Veldman, A., Wellens, P., & Huijsmans, R. (2017). An absorbing boundary condition for free surface water waves | Elsevier Enhanced Reader. *Elsevier*. doi:10.1016/j.compfluid.2017.05.018

Equinor. (2008). Norne-oppstart etter vellykket revisjonsstans. Retrieved March 11, 2019, from www.equinor.com/no/news/archive/2008/08/29/Norne29August.html

Faltinsen, O. M. (1999). *Sea loads on ships and offshore structures*. Ocean technology serie. Cambridge University Press.

Fenton, J. D. (1985). A Fifth-Order Stokes Theory for Steady Waves. *Journal of Waterway, Port, Coastal, and Ocean Engineerin*, 19.

Fonseca, N. (2016). *EXWAVE FPSO Model Tests - Main Report* (tech. rep. No. MT2016F-055). SINTEF OCEAN AS.

Fonseca, N., Hellan, Ø., Stansberg, C. T., Nestegård, A., & Birknes-Berg, J. (2019). EXWAVE 2 JIP - Wave forces on floating units in extreme seas. Internal document SINTEF OCEAN AS.

Fonseca, N., Ommani, B., Stansberg, C. T., Bøckmann, A., Nestegård, A., Birknes-Berg, J., & Baarholm, R. (2019). *Wave Forces and Low Frequency Drift Motions in Extreme Seas: Benchmark Studies*.

Fournarakis, N., Papanikolaou, A., & Liu, S. (2017). Estimation of the drift forces and added resistance in waves of the KVLCC2 tanker. *Journal of Ocean Engineering and Marine Energy*, *3*(2), 139–149. doi:10.1007/s40722-017-0077-7

Gerrits, J. (2001). *Dynamics of liquid-filled spacecraf*.

Greco, M. (2018). Lecture Notes - TMR4215. Department of Marine Technology, NTNU.

H.T. Ok, S. L., & Choi, J. (2016). Numerical simulation of motion of single and sideby-side vessels in regular waves using OpenFOAM. *Ships and Offshore Structures*. doi:10.1080/17445302.2016.1265697

Hanssen, F.-C. W., Bruschi, R., & Pettersen, E. (2013). Aspects of the Mean Surge Drift Force for Single-Point Moored Vessel, 8.

ITTC. (2017). Uncertainty analysis in CFD—verification and validation methodology and procedures. International Towing Tank Conference (ITTC). Retrieved May 4, 2020, from https://www.ittc.info/media/8153/75-03-01-01.pdf

Kleefsman, K. M. T. (2005). *Water impact loading on offshore structures. - A numerical study* (Doctoral dissertation, University of Groningen).

Leffler, W. L., Pattarozzi, R., & Sterling, G. (2003). *Deepwater - Petroleum exploration & production*. PennWell corporation.

Myrhaug, D. (2000). *TMR4230 OCENOGRAPHY-Wind Waves*.

Nestegård, A., & Fonseca, N. (2017). *Handbook on low-frequency wave forces and response-guidelines and recommendations* (tech. rep. No. 2017-0251, Rev. 2). SINTEF OCEAN AS.

Oracle Corporation. (2020). Oracle VM VirtualBox - User Manual. Retrieved April 29, 2020, from http://download.virtualbox.org/virtualbox/UserManual.pdf

Pinkster, J. A. (1980). *Low frequency second order wave exciting forces on floating structures*. Technische Wetenschappen aan de Technische Hogeshcool te Delft.

Schulz, K. (2007). Hacking Vim : A Cookbook to Get the Most Out of the Latest Vim Editor.

Sea2Cradle. (2015). FPSO Brasil. Retrieved October 12, 2019, from https://www.sea2cradle.com/trackrecord/fpso-brasil/

Sigma2. (2020). Documentation | Sigma2. Retrieved May 5, 2020, from https://documentation.sigma2.no/

Själander, M., Jahre, M., Tufte, G., & Reissmann, N. (2019). EPIC: An Energy-Efficient, High-Performance GPGPU Computing Research Infrastructure.

Skjelbreia, L., & Hendrickson, J. (1960). FIFTH ORDER GRAVITY WAVE THEORY. *Coastal Engineering Proceedings*, (7), 10–10. Number: 7. doi:10.9753/icce.v7.10

Stansberg, C. T., Kaasen, K. E., Abrahamsen, B. C., Nestegård, A., Shao, Y., & Larsen, K. (2015). Challenges in Wave Force Modelling for Mooring Design in High Seas. doi:10.4043/25944-MS

The Petroleum Safety Authority Norway - PSA. (2019). Risikonivå i petroleumsvirksomheten Hovedrapport, utviklingstrekk 2018, norsk sokkel.

Van Der Plas, P. (2018). Program documentation — ComFLOW 4.2.0-alpha documentation. Retrieved March 5, 2020, from http://poseidon.housing.rug.nl/sphinx/index_documentation.html

Van Dokkum, K. (2016). *Ship knowledge - Ship design, construction and operation*. DOKMAR Maritime Publisher BV.

Veldman, A. E. P., Gerrits, J., Luppes, R., Helder, J. A., & Vreeburg, J. P. B. (2007). The numerical simulation of liquid sloshing on board spacecraft. *Journal of Computational Physics*, *224*(1), 82–99. doi:https://doi.org/10.1016/j.jcp.2006.12.020

Wellens, P. R. (2012). *Wave Simulation in Truncated Domains for Offshore Applications* (PHD, Delft).

Zeltkevic, M. (1998). Adams Methods. Retrieved May 26, 2020, from http://web.mit.edu/10.001/Web/Course_Notes/Differential_Equations_Notes/node6.html

Appendix A

Geometries from GeniE in HydroD

A.1 Geometry with bulb

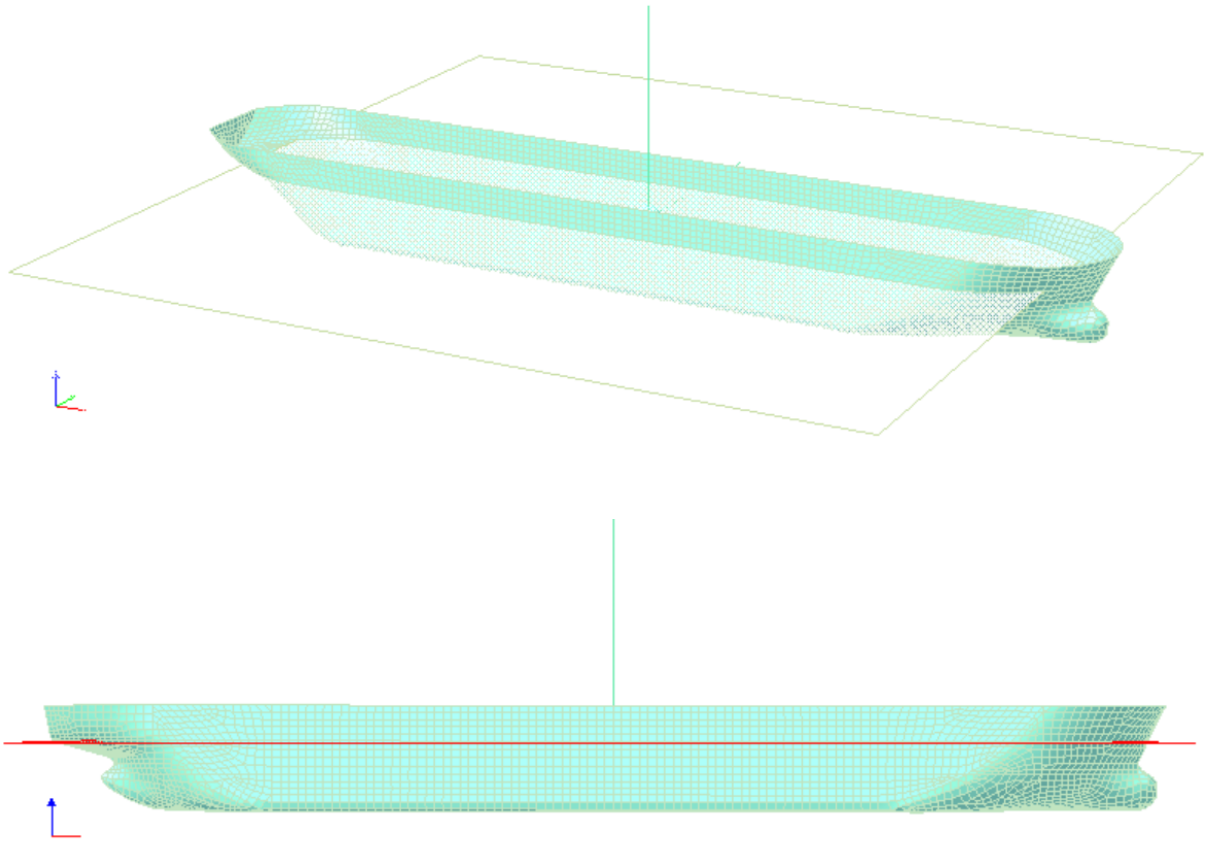

A.2 Geometry without bulb

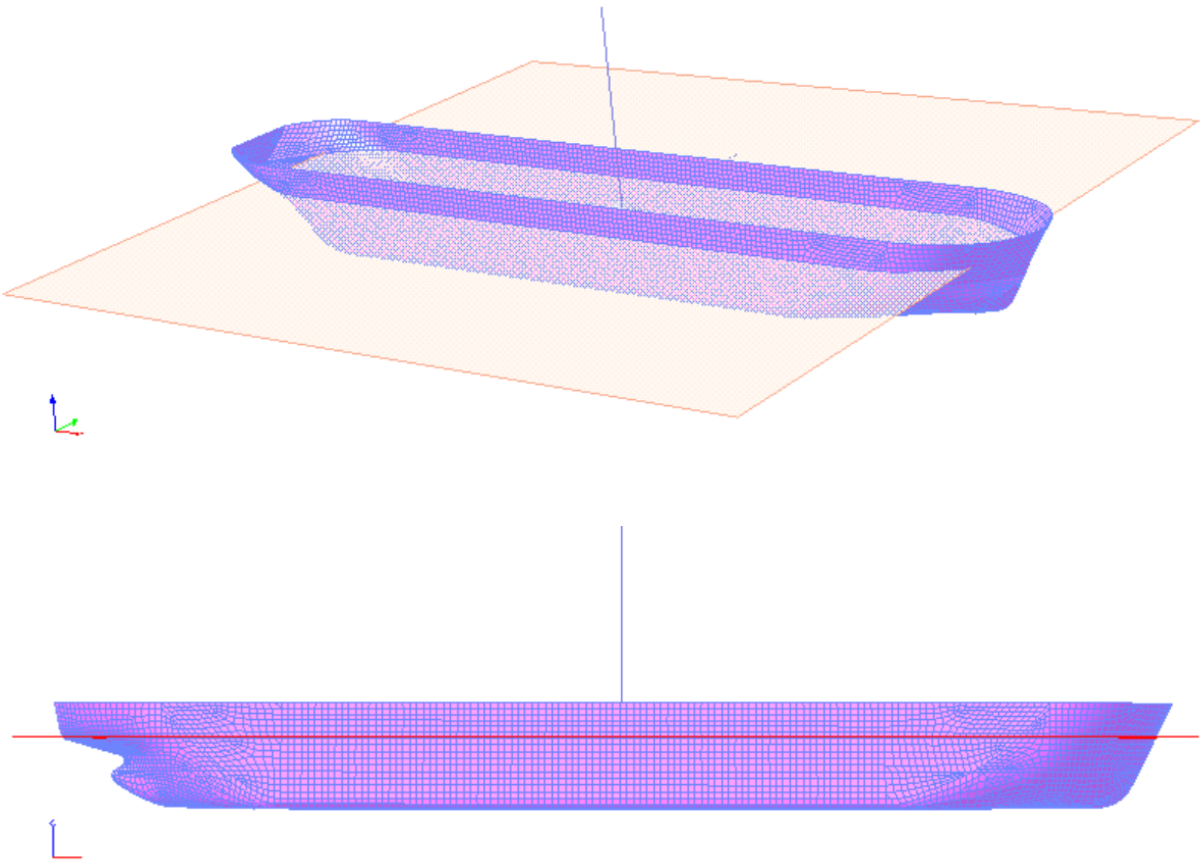

A.3 Wall sided geometry

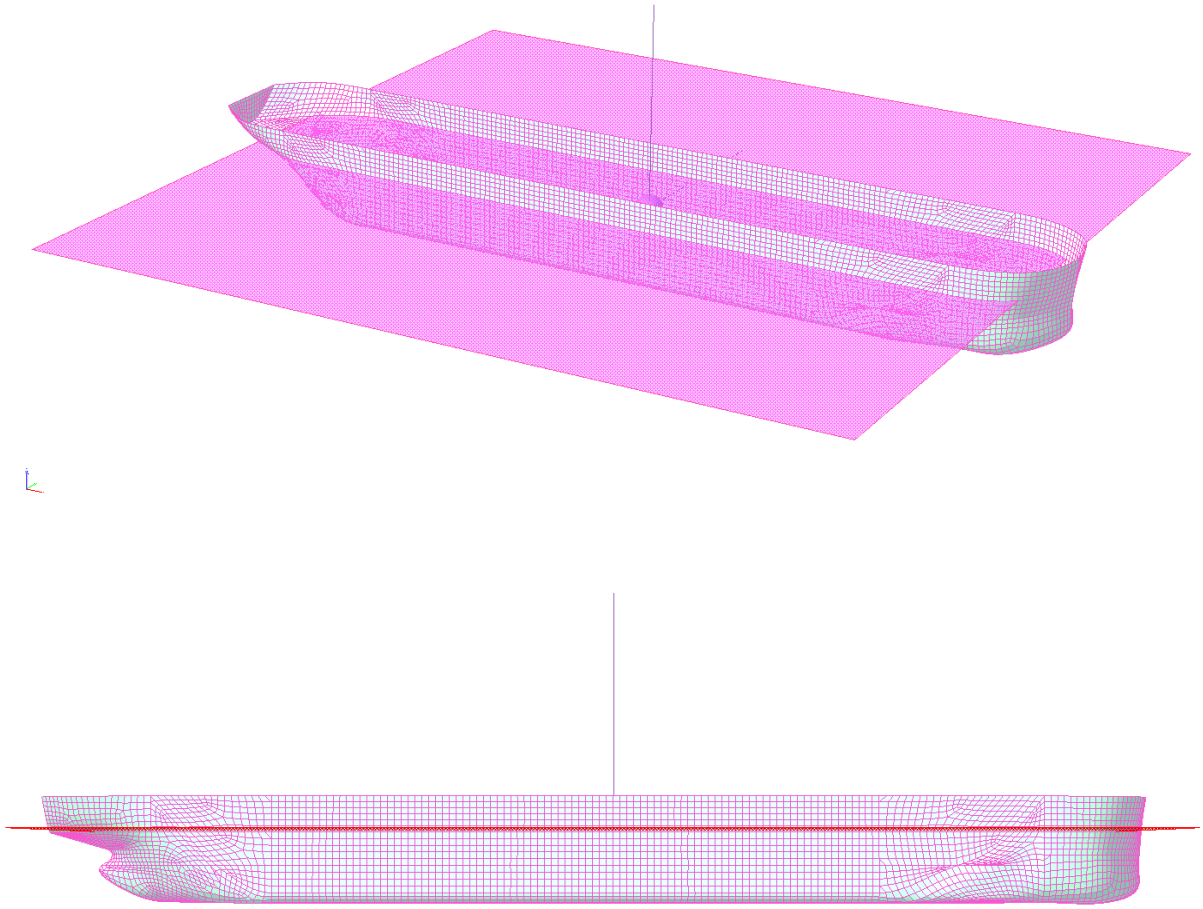

Appendix B

Verification of calculations from Wadam

B.1 RAO

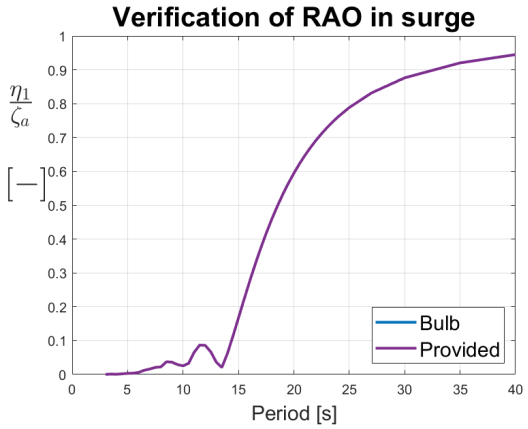

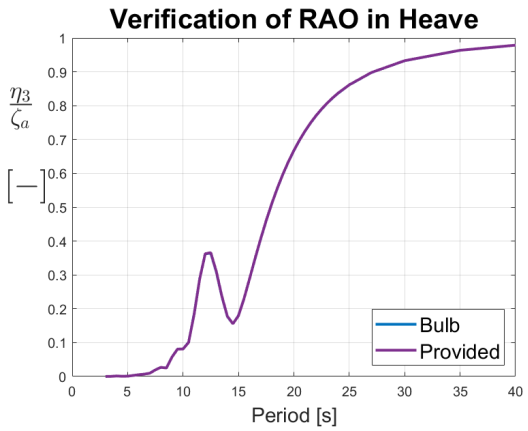

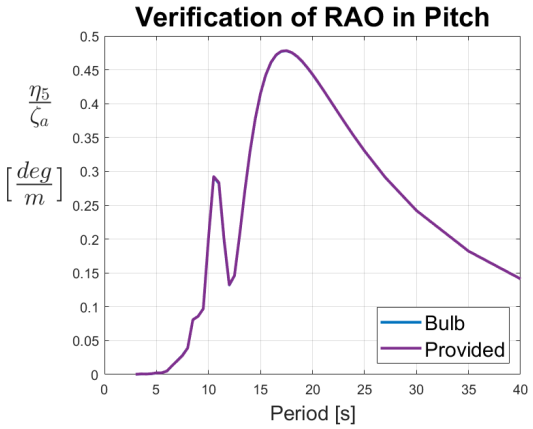

B.2 *Hdrift*

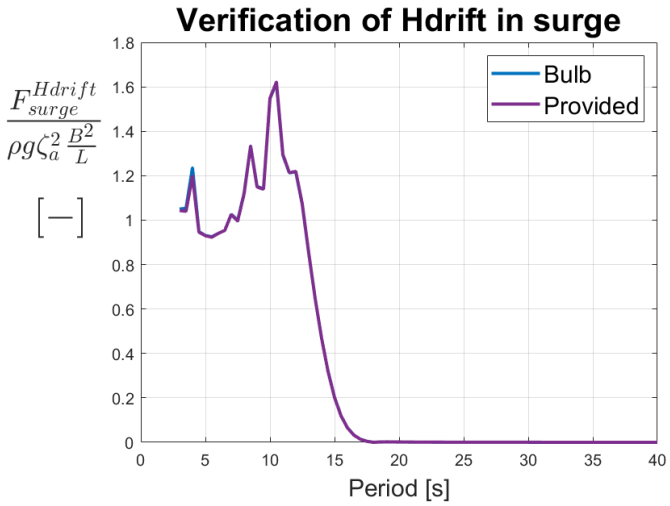
Verification of Hdrift in surge
$\frac{F_{surge}^{Hdrift}}{\rho g \zeta_a^2 \frac{B^2}{L}}$
[—]
Bulb
Provided
Period [s]

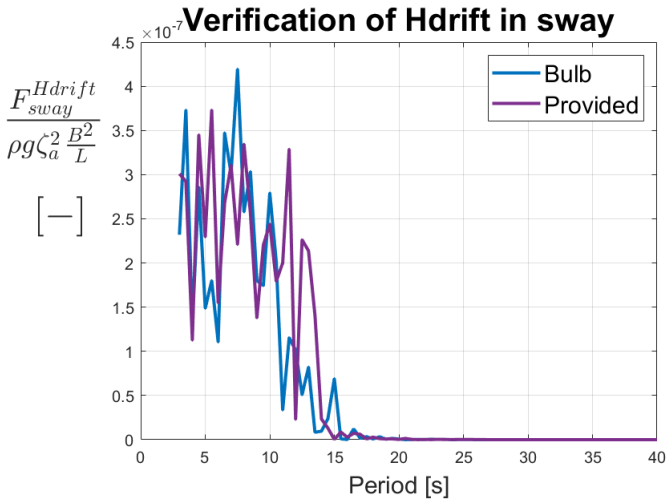
Verification of Hdrift in sway
$\times 10^{-7}$
$\frac{F_{sway}^{Hdrift}}{\rho g \zeta_a^2 \frac{B^2}{L}}$
[—]
Bulb
Provided
Period [s]

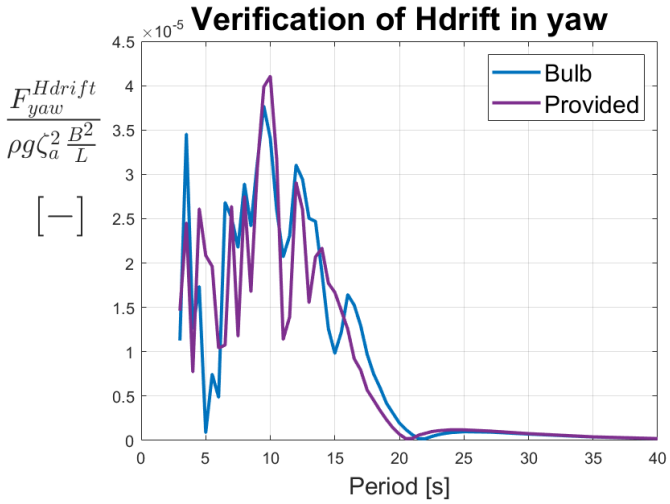
Verification of Hdrift in yaw
$\times 10^{-5}$
$\frac{F_{yaw}^{Hdrift}}{\rho g \zeta_a^2 \frac{B^2}{L}}$
[—]
Bulb
Provided
Period [s]

Appendix C

Coupled damping

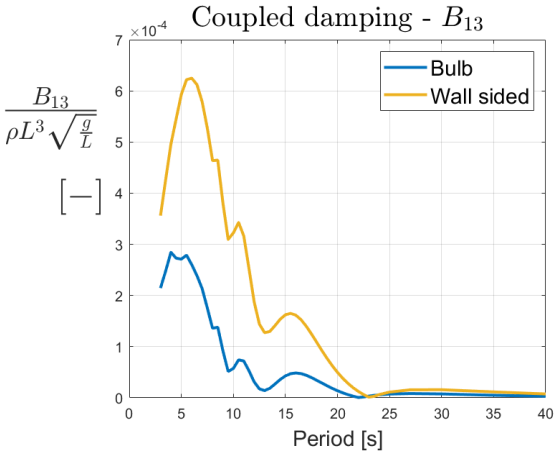

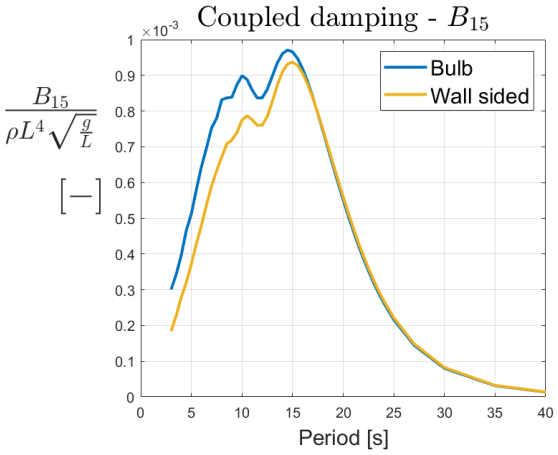

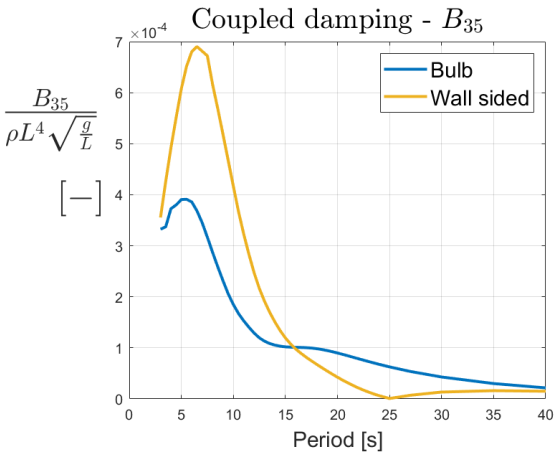

Appendix D

Mean drift forces in surge, sway and yaw

D.1 *Drift*

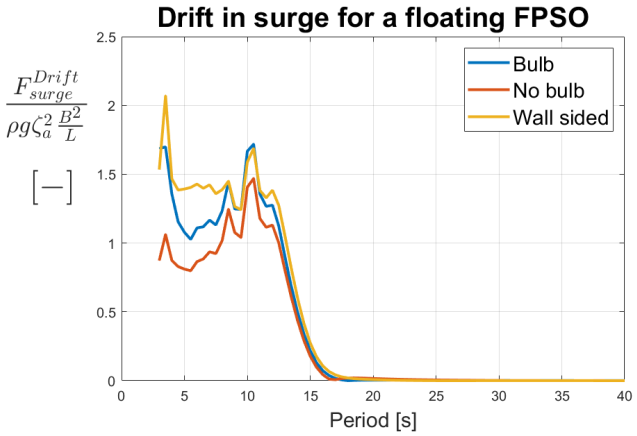

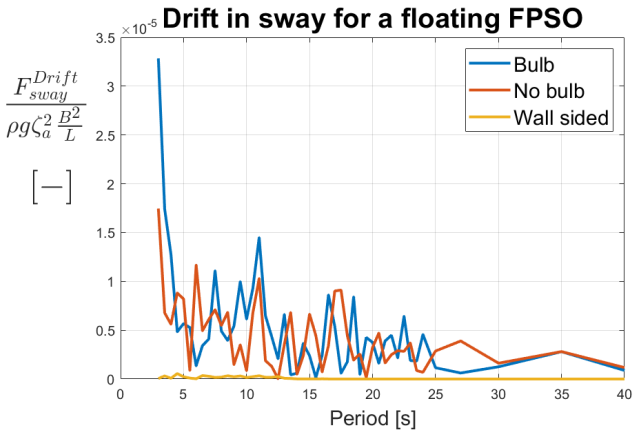

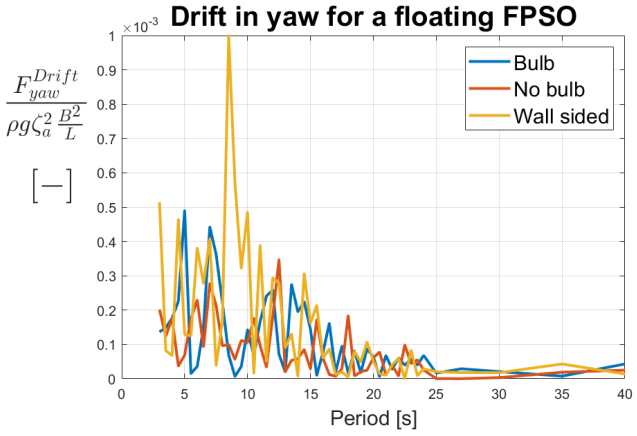

D.2 *Hdrift*

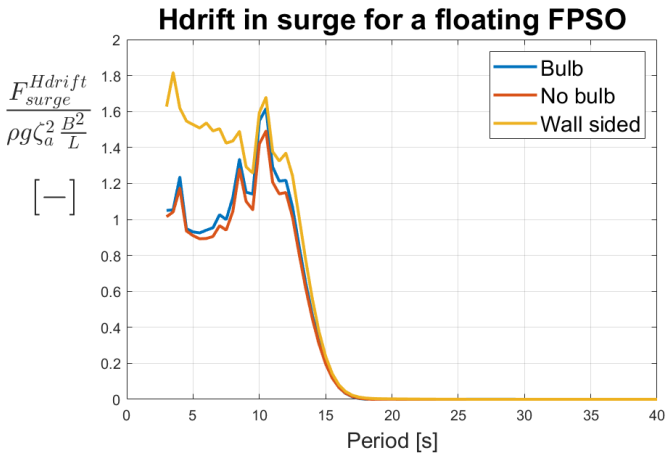
Hdrift in surge for a floating FPSO
$\frac{F_{surge}^{Hdrift}}{\rho g \zeta_a^2 \frac{B^2}{L}}$
[—]
Bulb
No bulb
Wall sided
Period [s]

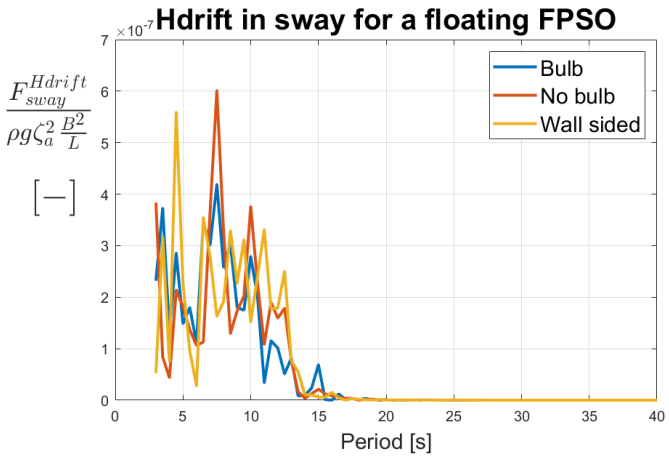
Hdrift in sway for a floating FPSO
$\times 10^{-7}$
$\frac{F_{sway}^{Hdrift}}{\rho g \zeta_a^2 \frac{B^2}{L}}$
[—]
Bulb
No bulb
Wall sided
Period [s]

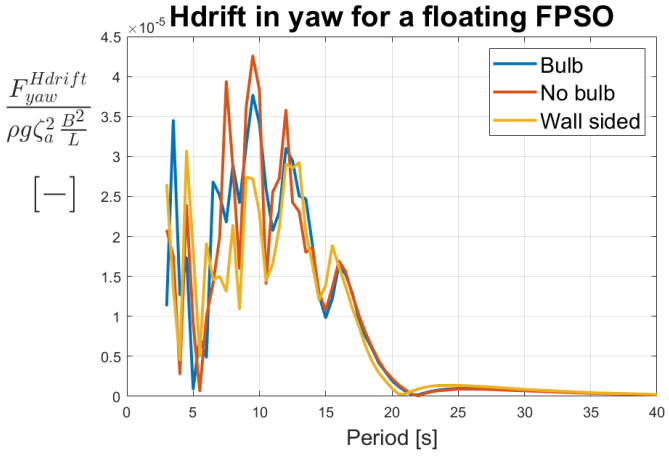
Hdrift in yaw for a floating FPSO
$\times 10^{-5}$
$\frac{F_{yaw}^{Hdrift}}{\rho g \zeta_a^2 \frac{B^2}{L}}$
[—]
Bulb
No bulb
Wall sided
Period [s]

Appendix E

Stationary areas ComFLOW

E.1 Domain

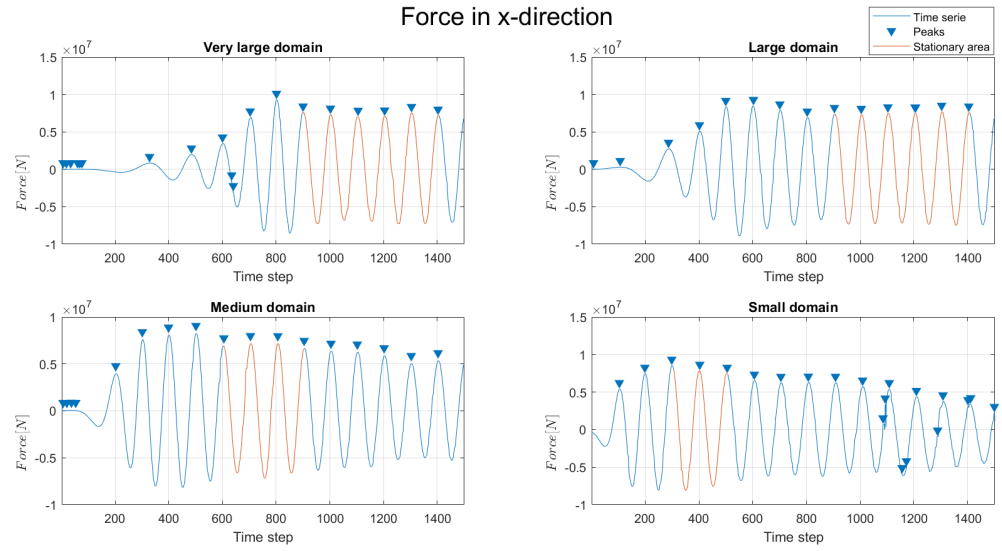

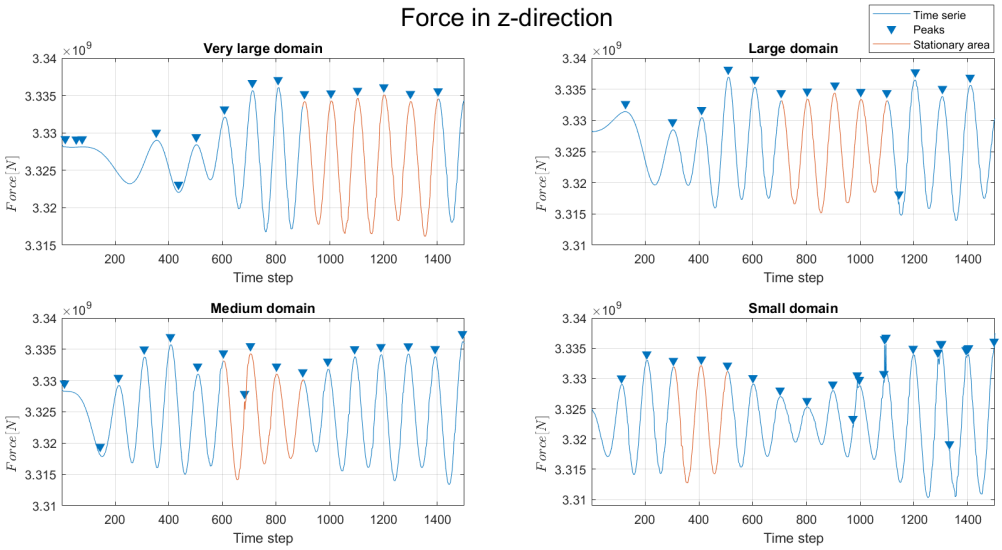

Appendix F

Coarse grid refinement

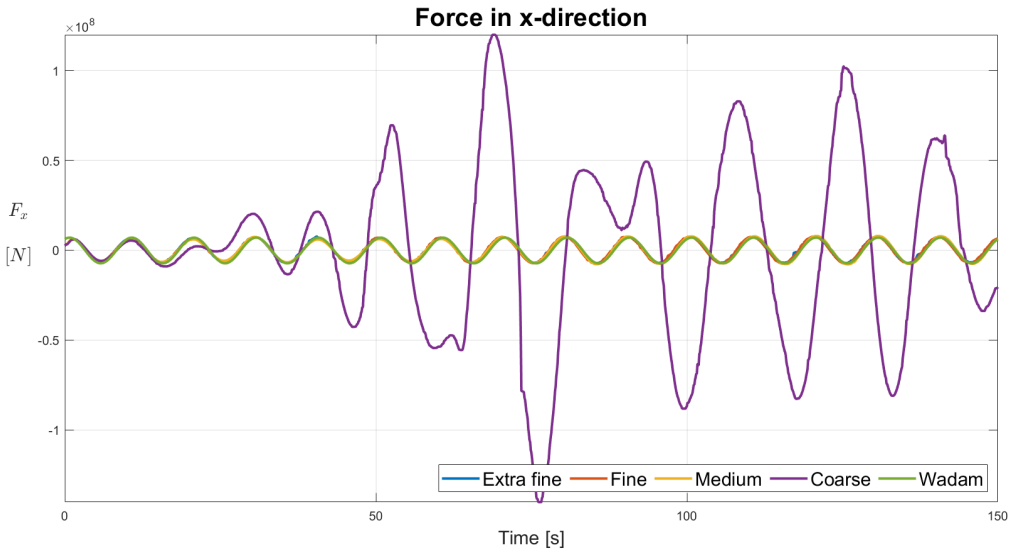

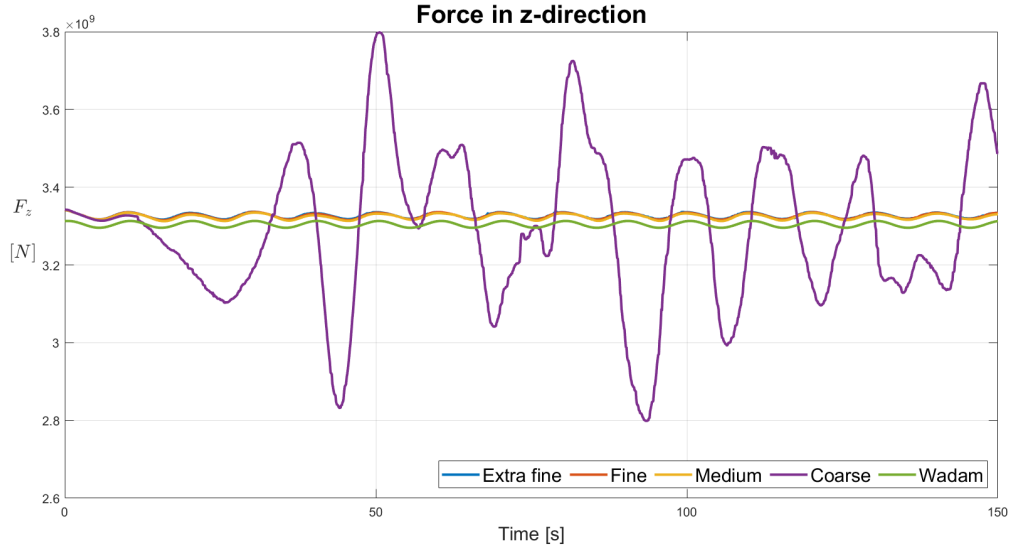

Appendix G

Verification of results from ComFLOW

G.1 Force in y-direction

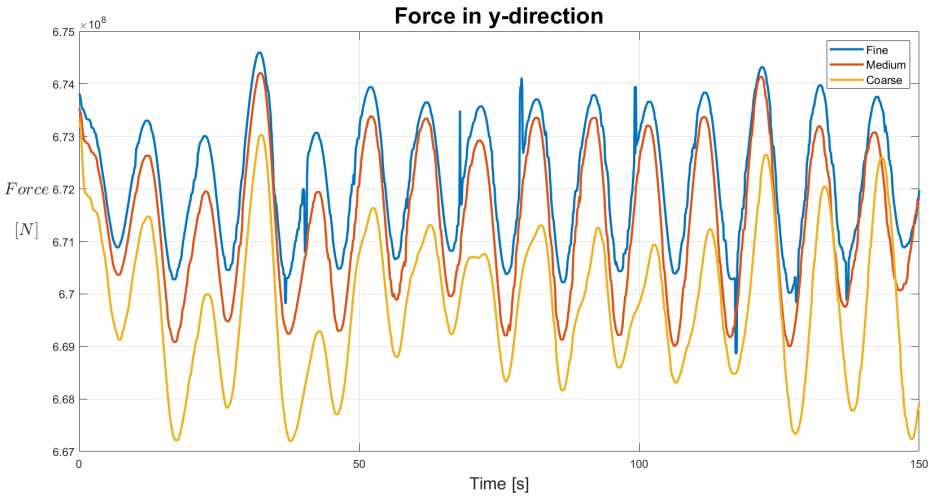

Figure G.1: Force in y-direction for the fine, medium and coarse grid refinement of the domain

G.2 Surface elevation

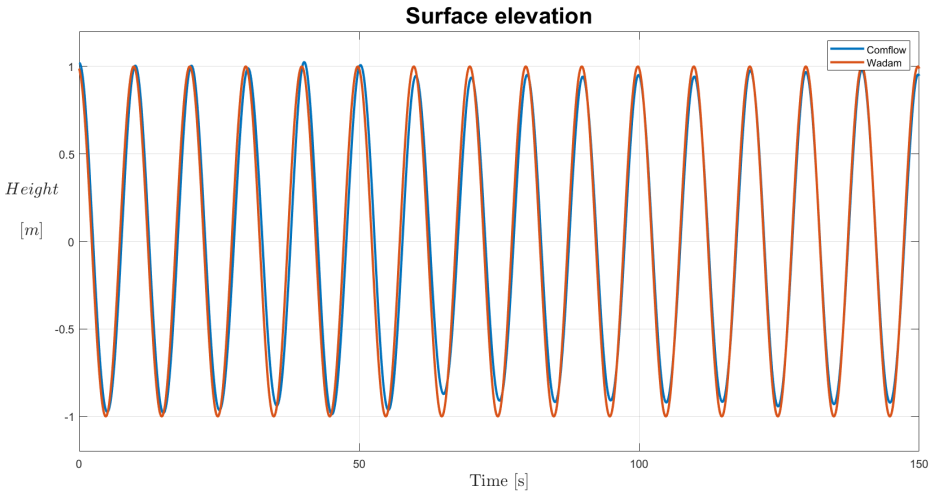

Figure G.2: Surface elevation at probe 2

Appendix H

Simulations from ParaView

The QR-codes can be scanned with a cellphone or pad to see simulations of the results in ParaView. When scanning the QR-code, you are directed to google drive.

H.1 Very large domain with fixed FPSO

The period is 10 s and the amplitude is 1 m.